NUMERICAL INVESTIGATION OF MECHANISMS TO AID IN ENHANCING SURFACE HEAT TRANSFER FROM AN IMPINGING 2D HOT-AIR JET

BY

MOHAMMED MUMTAZ AHMED KHAN

A Thesis Presented to the
DEANSHIP OF GRADUATE STUDIES

KING FAHD UNIVERSITY OF PETROLEUM & MINERALS

DHAHRAN, SAUDI ARABIA

In Partial Fulfillment of the
Requirements for the Degree of

MASTER OF SCIENCE

In

AEROSPACE ENGINEERING

JANUARY 2010

KING FAHD UNIVERSITY OF PETROLEUM AND MINERALS
DHAHRAN 31261, SAUDI ARABIA

DEANSHIP OF GRADUATE STUDIES

This thesis, written by **Mohammed Mumtaz Ahmed Khan** under the direction of his thesis advisor and approved by his thesis committee, has been presented to and accepted by the Dean of Graduate Studies, in partial fulfillment of the requirements for the degree of **MASTER OF SCIENCE IN AEROSPACE ENGINEERING**.

Thesis Committee

Farooq Saeed
Dr. Farooq Saeed (Advisor)

Dr. Ahmed Z. Al-Garni (Co-Advisor)

Hanafy Omar
Dr. Hanafy Omar (Member)

Ahmet
Dr. Ahmet Z. Şahin (Member)

Dr. Esmail M. A. Mokheimer (Member)

Dr. Ahmed Z. Al-Garni
Department Chairman

Dr. Salam A. Zummo
Dean of Graduate Studies

Date 15/5/10

بسم الله الرحمن الرحيم

To

My Beloved Parents
for their
Innumerable prayers, Encouragement and
Motivation.

ACKNOWLEDGMENT

In the name of Allah, The Most Gracious and The Most Merciful

Read! In the Name of your Lord, Who has created (all that exists). He has created man from a clot (a piece of thick coagulated blood). Read! And your Lord is the Most Generous, Who has taught (the writing) by the pen. He has taught man that which he knew not. Nay! Verily, man does transgress. Because he considers himself self-sufficient. Surely! Unto your Lord is the return. (Surah: Al-Alaq, 1-8)

All the praise belongs to Allah, the Most Beneficent and Magnificent, Who provided me the courage and persistence to conclude this work successfully, Who was with me in the most difficult times and always. Peace and blessings be upon Prophet Muhammad, his family and companions. I thank the All-Mighty for blessing me an opportunity to get admittance in King Fahd University of Petroleum & Minerals. My gratitude is also due to the esteemed university and to its learned faculty members for imparting valuable knowledge through their invaluable support and guidance that helped me in completing my thesis work.

My profound appreciation and heartfelt gratitude goes to my thesis advisor, Dr. Farooq Saeed, for his constant endeavor, guidance and the numerous moments of attention he devoted throughout the course of this research work. His valuable suggestions made this work interesting and knowledgeable for me. Special thanks to his ingenious discussion over FLUENT and GAMBIT. I also thank my thesis co-advisor Dr. Ahmed Al-Garni for his extended cooperation and fullest support during my entire course and research work.

I would also like to acknowledge all AE faculty members, who were involved with my M.Sc. course work or otherwise. Their knowledge and experience led me to secure this degree in a very professional manner. I also owe thanks and recognition to my fellow research assistants, course mates, colleagues and friends for their help, motivation and support. Special thanks to Mr. AbdurRahman, Mr. Imran Abdul Qayyum, Mr. Massihullah, Murtuza, Mr. Saad bin Mansoor, Mr. Bilal Siddique, Mr. Yousuf Elarian and Mr. Shaik Razwan for their moral and technical support.

Last but not the least, I would like to acknowledge the understanding, sacrifice, encouragement and moral support from my family at home. I am obliged to them lifetime, especially to my parents and siblings for their prayers, support and trust that made me achieve this important goal of my life.

TABLE OF CONTENTS

CHAPTER 1

CHAPTER 2

CHAPTER 3

CHAPTER 4

CHAPTER 5

CHAPTER 6

LIST OF TABLES

LIST OF FIGURES

THESIS ABSTRACT (English)

NAME: MOHAMMED MUMTAZ AHMED KHAN

TITLE: NUMERICAL INVESTIGATION OF MECHANISMS TO AID IN ENHANCING SURFACE HEAT TRANSFER FROM AND IMPINGING 2D HOT-AIR JET

MAJOR: AEROSPACE ENGINEERING

DATE: MARCH 2010

Aircraft icing is a serious concern for the aviation community since it adversely affects flight performance. There has always been a continuous effort to improve aircraft anti-icing systems. One such system is the hot-air anti-icing systems, which uses hot-air from the engine compressor bleed to heat critical aircraft surfaces. In this system hot-air is impinged on the inner side of critical aircraft surfaces which are susceptible to ice formation on the outer side. The heat transfer due to jet impingement prevents formation of ice and its accumulation. Numerous experimental and numerical studies have been performed to increase the efficiency of the hot-air jet based anti-icing systems. Most of the investigations have focused on either orifice design or the impingement region of target surface geometry. Since this surface heat transfer drops off sharply past the impingement region, investigators have studied the use of multiple jets to enhance surface heat transfer over a larger area. However, use of multiple jets is a further strain on engine resources. One way to conserve engine resources is to use single jet in conjunction with various mechanisms to enhance heat transfer over a large area. Hence, the study focuses on the heat transfer over a larger area using single jet and various mechanisms which can enhance heat transfer outside the impinging region. Most of these mechanisms increase the turbulence in the flow resulting in enhanced heat transfer. In this regards, several types of obstacles such as multiple triangles, cylinder, wedge, channel, cavities and vortex generator were investigated. The commercial CFD code, FLUENT, was used for numerical simulation of the above models. Insight gained from this study will help understand ways or mechanisms to enhance surface heat transfer as applied in aircraft anti-icing system.

MASTER OF SCIENCE DEGREE
KING FAHD UNIVERSITY OF PETROLEUM and MINERALS
Dhahran, Saudi Arabia

THESIS ABSTRACT (ARABIC)

ملخص الرسالة

الاسم : محمد ممتاز احمد خان
العنوان : التحقيق العددي للآليات للمساعدة في تعزيز مساحة الانتقال الحراري من فوهة ملامسة ثنائية الأبعاد
التخصص : هندسة الطيران والفضاء
التاريخ : يناير 2010، صفر 1431 هـ

لطالما كانت مشكلة تغطية الجليد للطائرة أثناء الطيران مصدر قلق بالغ للملاحة الجوية، لما يؤثره سلباً على أداء الطائرة. لقد بذلت جهود متواصلة لتحسين النظم المضادة للجليد في الطائرات. من هذه الأنظمة نظام الهواء الساخن المضاد للجليد، والذي يستخدم الهواء الساخن المدفوع من ضاغط المحرك لتسخين أسطح الطائرة ذات الأهمية في عملية الطيران. في هذا النظام يلامس الهواء الساخن الجوانب الداخلية لأسطح الطائرة المهمة والحرجة في عملية الطيران التي تكون عرضة لتكون الجليد على الجوانب الخارجية منها. بسبب الانتقال الحراري من فوهات هذا النظام الملامسة للأسطح فإن ذلك يمنع تكون الجليد وتراكمه. وقد أجريت العديد من الدراسات التجريبية والعددية لزيادة كفاءة نظام الهواء الساخن المضاد للجليد. ولقد تركزت معظم الدراسات والتحقيقات على تصميم فتحة الفوهات أو على الشكل الهندسي للمنطقة الملامسة للهواء الساخن. وبما أن مساحة الانتقال الحراري تتقلص بحدة ما وراء المنطقة الملامسة للفوهة، فلقد عمدت الدراسات والتحقيقات إلى استخدام فوهات متعددة لتعزيز مساحة الانتقال الحراري على مساحة أكبر. ومع ذلك، فإن استخدام فوهات متعددة يزيد من الضغط والإجهاد على المحرك بطلب كميات أكبر من الهواء الساخن. هناك طريقة واحدة للحفاظ على ثبات كمية الهواء المطلوبة من المحرك دون زيادة باستخدام فوه واحدة مع آليات مختلفة مساندة جنباً إلى جنب لتعزيز عملية الانتقال الحراري على مساحة أكبر. وبالتالي فإن هذه الدراسة تركز على زيادة الانتقال الحراري على مساحة أكبر باستخدام فوه واحدة مع آليات مختلفة مساندة جنباً إلى جنب لتعزيز عملية الانتقال الحراري على مدى نطاق أوسع خارج المنطقة الملامسة للفوه. معظم هذه الآليات تزيد من اضطراب تدفق الهواء الساخن مما يتسبب في تحسين عملية الانتقال الحراري. في هذا الإطار، جرى استخدام ودراسة عدد من الأشكال، مثل المثلثات المتعددة، الاسطوانات، الأسافين، القنوات، التجاويف، مولد الدوامات. تم استخدام برنامج FLUENT للمحاكاة العددية للنماذج المذكورة أعلاه. على ضوء هذه الدراسة، سوف تساعد النتائج المحصلة على فهم الطرق والآليات التي تعزز مساحة الانتقال الحراري كما هو مطبق في النظم المضادة للجليد في الطائرات.

درجة ماجستير في العلوم
جامعة الملك فهد للبترول والمعادن
الظهران ، المملكة العربية السعودية

Nomenclature

A	surface area (m^2)
d	horizontal distance between each element in a model (m)
d_1	hole diameter on perforated plate (m)
E	total energy per unit volume (J/m^3)
e	internal energy (J)
F	frequency of flow field pulsation (s^{-1})
H	distance of jet from impinging plate (m)
H_w	distance of the wedge from impinging plate (m)
h	distance of the model from the target plate (m)
l	horizontal length of the model (m)
Nu	$\text{Nusselt number} = \frac{\text{convective heat tranfer coefficient}}{\text{conductive heat transfer coefficient}}$
Pr	$\text{Prandtl number} = \frac{\text{viscous diffusion rate}}{\text{thermal diffusion rate}}$
p	hole pitch on perforated plate (m)
q	energy flux (W/m^2)
R	radius of jet (m)
Re	$\text{Reynolds number} = \frac{\text{inertial forces}}{\text{viscous forces}}$
r	radius of the model (m)
S	slot area = 2 × jet diameter (m)
x	position on impinging plate
Δt	height of each equilateral triangle (m)

Symbols

δ	boundary layer thickness (m)
θ	top half angle of wedge (deg)
Φ	specific quantity per unit volume
φ	vortex generator angle (deg)

Subscripts

c	cavity
ch	channel
cyl	cylinder
d	orifice
E	equivalent for square heat sink base
HS	total exposed area
rs	ratio defined as $8R^2/D_e^2$
t	triangles
w	wedge
z	perforated plate
vg	vortex generator

CHAPTER 1

INTRODUCTION

1.1 An Overview

Ice formation and accumulation on the aircraft has been a subject of serious concern since the past 20 years. In 1989, a commuter aircraft impacted terrain during landing killing both crew members and the entire four passengers. In March 1992, a transport aircraft stalled on takeoff in New York, killing two crew members and 25 passengers. A commuter flight went out of control and dived into a soybean field en route to Chicago, Illinois, U.S., in October 1994 killing all 68 aboard. The cause of these accidents and many similar was found to be aircraft icing. More recently, a Bombardier Dash-8 Q-400 aircraft fell off from the sky killing all 49 aboard due to severe ice accumulation on the wings in a very short time. Icing related accidents have led the U.S Federal Aviation Administration (FAA) to take a renewed interest in aircraft icing related research and a revision of related regulations. FAA In-Flight Aircraft Icing Plan [1][2] outlined validation and reliability tasks for icing and anti-icing simulation methods being used in the aircraft certification. Thus, in 1997 a comprehensive overview was published by the FAA showing the scope of icing-accident preventive measures.

The plan clearly laid out the importance of ice accretion simulations as well as measures to remove and avoid icing on aircraft surfaces.

It is now a well established fact that ice formation on critical aircraft surfaces severely degrades the aerodynamic performance of the aircraft. Ice accretion on lifting surfaces reduces the lift, increase the drag and weight. This ice accretion results in an increase in the stall speed and a reduction in the stall angle of attack. Therefore, an aerodynamic stall can occur before the stall warning systems can detect it. In propellers, ice drastically affects the efficiency and causes an imbalance resulting in vibrations. The rotor blades degrade in their efficiency using more power for equivalent lift causing the aircraft to descend higher than the normal rate during the approach. Ice on the canopy reduces the cockpit vision heavily. Communication antennae may be rendered ineffective or even snap off. Extension of flap may result in rudder ineffectiveness or even increase in stall speed. In addition to these problems, the detached ice may also cause unexpected problems such as flame out or compressor stall when ingested into the jet engine.

1.1.1 Types of Anti-Icing Systems

In order to avoid the problems pertaining to icing on the aircraft, the aircraft manufacturers typically make use of anti-icing system. Aircraft anti-icing system help prevent ice accumulation on important aircraft surfaces. There are different types of anti-icing systems used today which are designed to prevent ice accumulation. These anti-icing systems include:

1.1.1.1 Electrical Type

Electric heaters are used to heat critical areas. Although it is effective in preventing ice accretion in the leading edges of wings and stabilizers, it requires a large electrical current to be effective over a large area.

1.1.1.2 Pneumatic Type

The system is equipped with black rubber boots on the leading edges of wings and stabilizers in most turboprop and piston aircrafts. The rubber boots inflate and deflate alternatively in cycles flexing the accumulated ice. On failing to deform, the accumulated ice cracks and detaches from the aircraft surface.

1.1.1.3 Hot-Air Jet Type

In many aircrafts, hot-air from the compressor bleed is supplied to the wing's/slat's leading edge through ducts (see Fig. 1a). When the hot-air is impinged along the length of the wing (Fig. 1b), it helps eliminate ice by heating the surface. Similarly, areas around the jet intake can be protected from ice formation at the expense of engine power.

1.1.2 Hot-air Anti-Icing System

The most common anti-icing system used today on the aircrafts is the hot-air anti-icing system (Fig. 1a). The hot-air anti-icing system uses the bleed air from the engine compressor to heat the wing leading edge through the piccolo tube. This tube has several nozzles along its length maintaining a particular distance. The hot-air is impinged upon the inner surface of the slat or wing's leading edge. As the surface is heated, ice on the outer side melts in the vicinity of the impingement region, thereby also preventing ice accumulation.

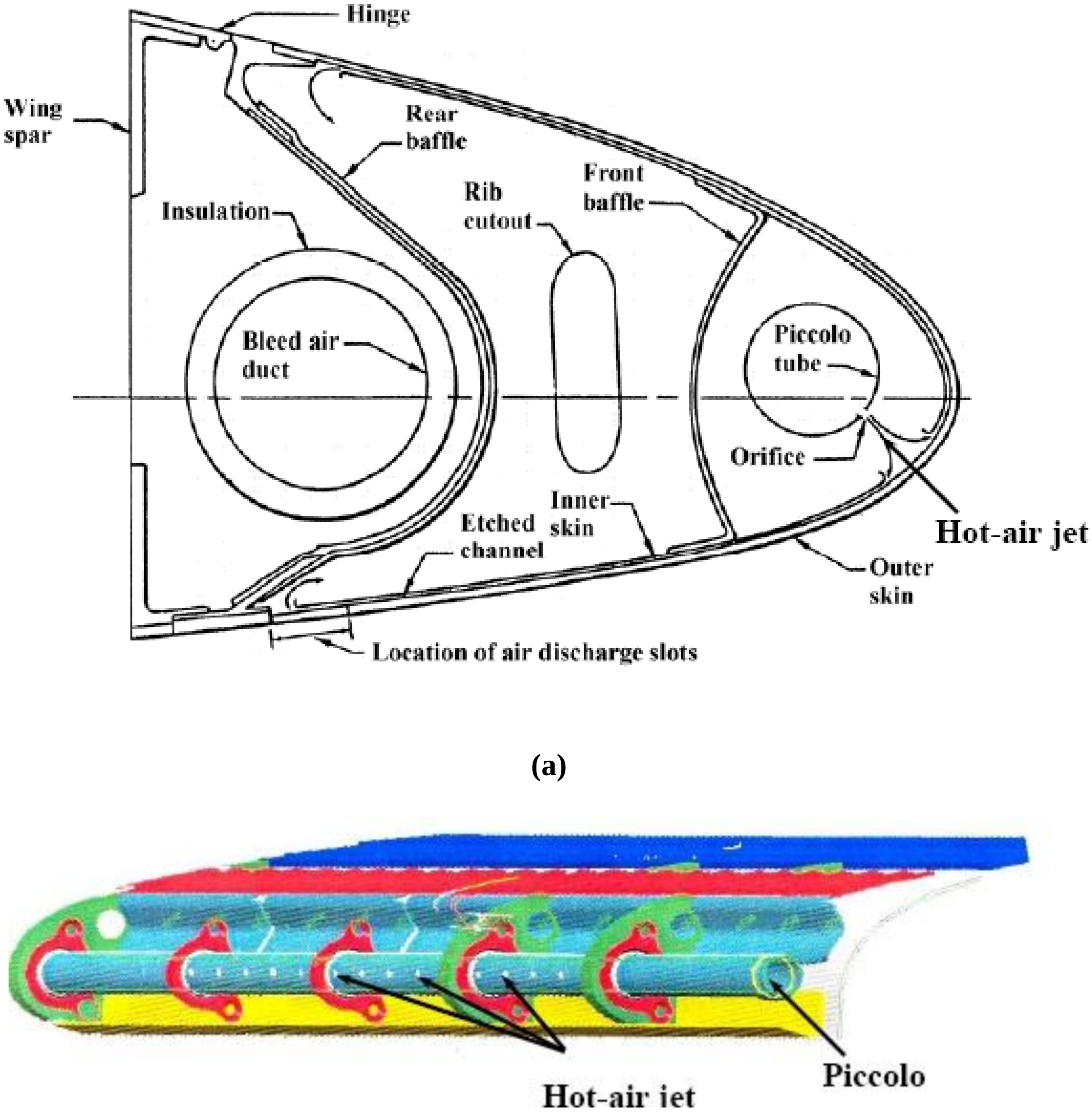

(a)

(b)

Figure 1.1 Internal layout of the piccolo tube: (a) Typical wing leading edge, (b) A typical slat

There are other systems which can be used for anti-icing in an aircraft but all of these have one common drawback that they eliminate ice at the cost of engine performance [3]. In order to minimize the use of engine resources , only a handful of investigators [4][5][6][7][8] have focused their attention on improving the anti-icing system. In addition, only a few studies focused on complex interactions of jet and curved surfaces [5][6][7] typical of wing leading edge.

On the other hand, jet impingement on a flat surface is commonly used in industries in different processes and therefore an extensive literature [7][10] on industrial applications is available today. Most of the literature focuses on key parameters such as jet nozzle-to-surface spacing, jet Reynolds number, jet diameter, jet nozzle-to-nozzle distribution, etc so as to improve the efficiency of the system. A brief overview of the related literature is given in the next section.

1.2 Motivation for the Current Study

It is essential to note that the hot air used for the anti-icing system is taken from the engine compressor bleed and is therefore, a strain on the engine resources. Utilizing this energy in the most efficient way is as necessary as efficient use of fuel for greater economy. A significant amount of heat energy taken from the compressor bleed air for anti-icing system is wasted as a result of inefficient use of the bleed air since the bleed air that exhausts into the atmosphere after being used by anti-icing is still warm. In order to utilize most of the heat energy in the bleed air, it becomes imperative to study the interaction between the hot–air jet and curved surfaces and investigate mechanisms that can aid in enhancing surface heat transfer.

Numerous experimental and numerical studies have been performed to increase the efficiency of the jet impingement based anti-icing system. Most of the investigations focus on either orifice design [11][12][13][14] or the impingement region of target surface geometry. It is an established fact that the surface heat transfer drops off sharply past this impingement region. Although, investigators have studied the use of multiple jets to enhance surface heat transfer over a larger area, use of multiple jets is a further strain on engine resources. The idea of enhancing heat transfer over a larger area using single jet is the focus of this study. Literature review suggests different mechanisms that can aid in enhancing heat transfer over a greater area such as increased turbulence [11][15] or jet intermittency [16].

1.3 Thesis Outline

Chapter one, the introductory chapter, gives an overview of this thesis which deals with improving performance of current aircraft icing systems. The chapter gives a brief introduction to aircraft anti-icing systems and presents an approach to improve the effectiveness of the hot-air jet based aircraft anti-icing system.

Chapter two contains a detail study of the literature available on jet impingement and different techniques used to enhance surface heat transfer. The research was done irrespective of the field of application. All the support for the investigations was taken from this chapter.

Chapter three illustrates the basic physics and presents the governing equations for the present study including turbulence models available and boundary conditions applied along with material properties.

Chapter four presents the numerical modeling and pre-validation study to select appropriate turbulence model for the numerical investigations in this research. All the turbulence models are explained in this chapter.

All the results are discussed in chapter five. A classification of results based on parametric variation and heat transfer distribution is presented. Important findings in each result and interesting facts are discussed. Chapter 6 outlines the conclusion drawn from this research with recommendations for future study.

CHAPTER 2

LITERATURE REVIEW

Heat transfer enhancement techniques started appearing before 1920, but it was only after 1955 when the number of publications increased tremendously. It was the result of the requirement mainly in chemical, aerospace, power and electronic industries. The second boost in the publications was in 1975 due to the oil embargo, after which about 10% papers in major journals dealt with enhancement. Eventually; by 1991, more than 250 manufacturers offering different products incorporating enhancement technology existed [17]. However, empirical correlations were main part of the experimental investigations. Visual observations gave much new information leading to analytical treatments and numerical studies.

Numerous studies have been carried out to investigate the effects of impinging jet heat transfer with respect to Reynolds number, nozzle-to-plate distance, nozzle geometry, jet temperature, target surface orientation, multiple jets, cross flow, and surface shape on the flow. Many experimented on their idea of different nozzle configuration. Gardon and Akfirat [18] studied the flow and heat transfer characteristics of two -dimensional and axisymmetric impinging jets with different nozzle configurations . Similarly , Obot et al . [19] investigated the effects of different nozzle geometries on the flow and heat transfer characteristics of round impinging jets.

Popiel and Boguslawski [20] showed how nozzle exit configuration affects the stagnation point heat transfer. Oyakawa et al. [21] measured the heat transfer using three square-edged orifice nozzles with different cross-sections; round, elliptic and cross-shaped.

In 1977, Martin Holgar [7] made an extensive study to derive an empirical correlation for different combinations of arrays of hot jet. He used results of different types of target surfaces heat transfer distribution in terms of Nu distribution. The following empirical correlation gives good agreement with the experiments on single slot jet impinging on a flat surface.

$$\begin{aligned} \left(\frac{\overline{Nu}}{\mathrm{Pr}^{0.42}}\right) &= \frac{1.53}{x/S + H/S + 1.39}\mathrm{Re}_S^m \\ m &= 0.695 - \left[x/S + (H/S)^{1.33} + 3.06\right]^{-1} \end{aligned} \tag{2.1}$$

Range of validity:

$$\begin{gathered} 3000 \le \mathrm{Re}_S \le 90{,}000 \\ 2 \le x/S \le 25 \\ 2 \le H/S \le 10 \end{gathered}$$

The empirical correlation given above is used for validation of numerical predictions in the present research.

Kurima et al. [22] in 1989 for the first time conducted experiments to study the effect of a perforated screen on the jet-flow distribution. Their set up used a perforated plate in front of a target plate for a range of hole-diameter to exit-diameter ratios, pitch-to-diameter ratios and a Re ~ 18,000. They found that the heat transfer augmentation is the highest inside the potential core region of the jet. Conditions like pitch-to-diameter ratio (*p*/*d*) of the perforated plate, and distance form target plate to perforated plate increased the heat transfer coefficient by about 2.3 times to that without a perforated plate. They also suggested that it is desirable to have a larger hole diameter and the hole pitch should be such that $p/d \sim 2$.

In 1993, Zumbrunnen and Aziz [23] used water jet to study the effect of intermittency on convective heat transfer on a constant heat flux surface for both steady and intermittent impinging jets at distances up to seven jet-widths from the stagnation line. Their experiments yielded enhancement in heat transfer coefficient of nearly a factor of two, where as theoretical considerations suggested more than this value. They concluded that if the frequency of the intermittency is sufficiently high, the convective heat transfer enhancement increases monotonically.

Huber and Viskanta [24] investigated the influence of spent air exits located between a confined 3×3 square array of axisymmetric air jets with a radial distribution Reynolds number ranging from 3,500 to 20,400. They also found secondary maxima (small separation distance $H/R \leq 1.0$) occurred in the local convective coefficient similar to a single jet enhancing the average convective heat transfer coefficient. They also discovered that without spent air exits located between the jet orifices in the jet orifice plate, the heat transfer enhancement is lost due to the radially outward flow of the spent.

Haneda et al. [16] introduced a cross-stream oscillatory motion of a cylinder perpendicular to its axis and augmented the maximum Nusselt number around the stagnation point by about 20% compared to the normal impinging jet without the insertion of a cylinder. He vibrated the cylinder using two strings one on each end supporting the cylinder (Fig. 2.1). He found that the heat transfer enhancement by the insertion of rigidly suspended cylinder was about 40% and more than 20% for H/2*R* = 3 and 5 respectively, where as the insertion of spring suspended cylinder had the highest value of enhancement ratio a little lower than in case with a rigidly suspended cylinder. He concluded that the effectiveness of the heat transfer enhancement was higher when the target plate was located at a distance of 6 times the jet radius (6*R*) from the jet exit.

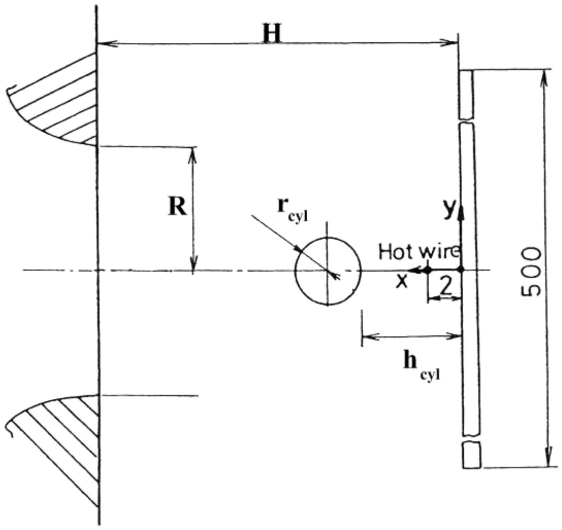

Figure 2.1 Coordinate system of Haneda et al [16]

In the same year, David et al. [25] used a pulsed air jet on a heated surface for the purpose of enhancing heat transfer relative to the corresponding steady air jet. Variables such as jet-to-plate spacing *H*, Reynolds number Re, and pulse frequency *f* were investigated. They involved a new term "duty-cycle" (ratio of flow on time to total cycle time for one period of the flow pulsation) in determining the level of heat transfer enhancement. They observed the work of Zumbrunnen and Aziz in 1993 [7] on flow pulsations resulting in increase in local Nusselts number by up to 100% for Re in the range of 3,100 to 21,000. The enhancement was believed to be largely the result of the effect of secondary flow structures (vortex rings) impingement. In David's test, a jet-to-plate spacing of $H/2R = 4$ and a pulsation frequency range from 25-35 Hz was used. Maximum heat transfer occurred for the highest flow speed. The pulsed flow heat transfer increased by 65% above that for a steady jet. At $H/2R = 6$, the steady jet heat transfer was slightly higher but the heat transfer enhancement went down and so on for the next experiment. At the end they found that the duty cycle cases consistently produced better heat transfer results and stated that higher frequencies should produce more enhancement. Hence, duty cycle parameter is crucial for the purpose of optimizing heat transfer enhancement associated with pulsed impingement. They also suggested that the mechanical valves developed for this study are quite promising for industrial use.

In 1999, Behnia et al . [26] used circular confined and unconfined impinging jet configurations to simulate the flow and heat transfer. They used an elliptic relaxation turbulence model, also called as $v2 - f$ model [54] in their numerical simulation. Their parameters for the test were jet Reynolds number and jet-to-target distance. They determined that the effect of confinement on the local heat transfer leads to a decrease in the average heat transfer rate, but doesn’t change the local stagnation heat transfer coefficient. He claimed that the heat transfer enhancement is effective only at very low nozzle-to-plate distances ($H/D < 0.25$). They stated that the velocity profile and the turbulent intensity in the nozzle have a strong influence on the qualitative and quantitative surface Nusselt number distribution.

In 2000, Saeed et al. [27] used 2D Navier Stokes CFD code to simulate the jet impingement on a flat plate and modified RAE 2822 airfoil. They used k-ϵ model in CFD code - NSC2KE to validate the numerical predictions. They observed that the flat-plate empirical correlations are not reliable enough to use in anti-icing simulations where the impingement surface is curved. They developed a new CFD code which can be used for more diversified problems accurately calculating the heat flux, therefore preventing unnecessary loss of energy and resources. Their work developed correlations for both 2D and 3D models [28][29]. Recently, other investigators [30] have also come up with similar correlations.

In 2000, Lee and Lee [31] reviewed the work of different investigators that used different jet nozzle configurations. They found that the nozzle exit configuration has an effect on heat transfer. They carried out experiments using three different types of orifice nozzles (see Fig. 2.2), which included sharp-edged orifice nozzle, standard-edged orifice nozzle, and a square-edged orifice nozzle with same diameter D. They used a nozzle-to-plate spacing of H/D = 2, 4, 6 and 10 and jet Reynolds numbers ranging from 5,000 to 30,000. They concluded that among the three nozzles tested in the study, the sharp-edged orifice nozzle gave the highest local and average heat transfer rates in the stagnation region. Nusselt numbers were approximately 50-75% higher than those of contoured nozzle jet. Finally they stated that the nozzle exit configuration can be used as an effective passive control technique for heat transfer enhancement as the variation in nozzle exit configuration alters the initial flow structure at the nozzle exit, and hence influences the local heat transfer characteristics.

El-Sheikh and Garimella [32] in 2000 experimentally investigated the enhancement of heat transfer from a discrete heat source in confined air jet impingement (see Fig. 2.3). In conjunction with confined impinging air jet and extent of heat transfer enhancement, a variety of pin-fin heat sinks were evaluated and quantified. Jet Reynolds number ranging from 8,000 to 45,000 and orifice diameter from 12.7 to 38.1 mm were used in the study.

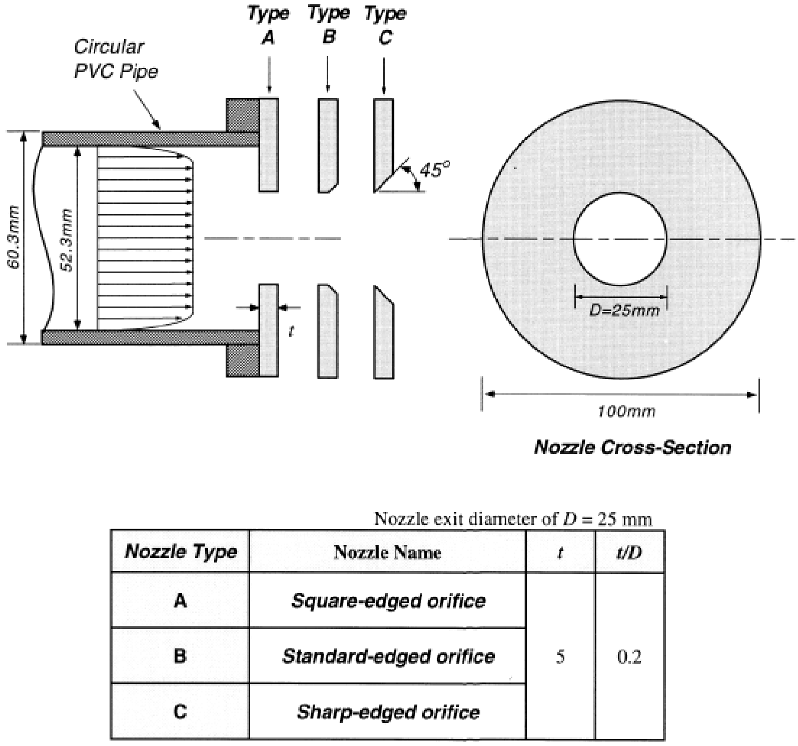

Nozzle exit diameter of D = 25 mm

Nozzle Type	Nozzle Name	t	t/D
A	*Square-edged orifice*	5	0.2
B	*Standard-edged orifice*		
C	*Sharp-edged orifice*		

Figure 2.2 Configuration of orifice nozzles tested by Lee and Lee [31]

El-Sheikh and Garimella [32] found that the enhancement in heat transfer was a strong function of nozzle diameter and heat sink footprint area (area under the pin fins in contact with the target plate); and that at a given flow rate, the effectiveness of the pin-finned heat sinks decreases with decreasing nozzle diameter. The effectiveness of the pin-finned heat sinks, defined relative to the unpinned ones, was in the range of 2.4 to 9.2, with the upper end being achieved for the tall pins with the largest nozzle diameter. A decrease in the nozzle diameter improved the heat transfer enhancement at a fixed flow rate. Smaller pin diameters showed higher heat transfer coefficients, by 8 to 25% depending on the nozzle diameter. Nozzle diameter and heat sink footprint were primarily affecting the enhanced heat transfer. A correlation was also proposed between $\mathrm{Nu}_{\mathrm{HS}}$ (Nusselt number with total exposed surface area of heat sink)and the pin fin parameters as

$$\mathrm{Nu}_{HS} = 2.759\mathrm{Re}^{0.620}\,\mathrm{Pr}^{0.4}\,(A_{HS}/A_d)^{-0.536}(D_e/d)^{0.217}\,A_{rs} + 2.083\mathrm{Re}^{0.817}\,\mathrm{Pr}^{0.4}\,(A_{HS}/A_d)^{-0.928} \times (D_e/d)^{-0.114}(1\text{-}A_{rs}) \qquad (2.2)$$

Where A_{HS} is Total exposed surface area of heat sink, A_d is areas of orifice, $D_e/2R$ is the ratio between Diameter of square heat sink base and orifice and A_{rs} is area ratio defined as $8R^2 / D_e^2$

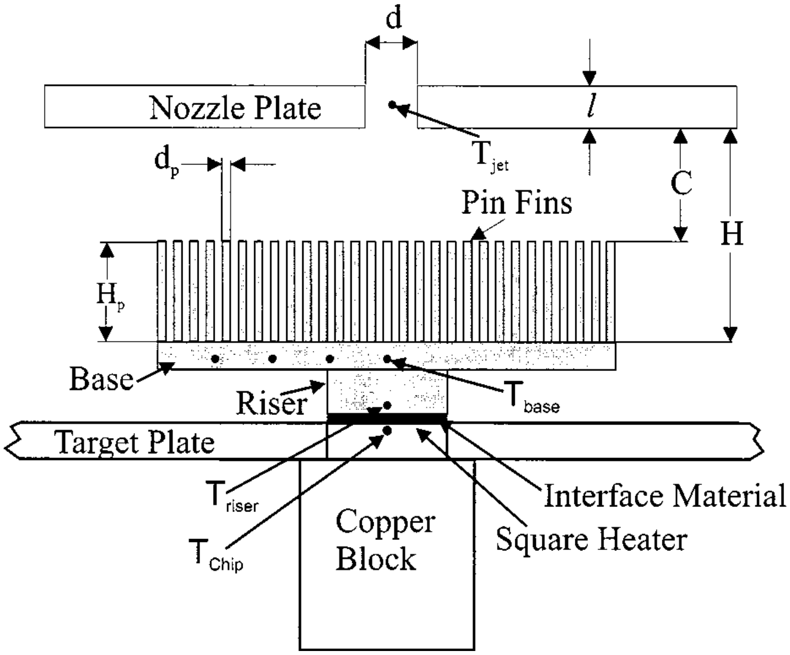

Figure 2.4 Pinned heat sink showing geometric parameters by El-Sheikh and Garimella [32]

In 2002, Lee et al. [15] observed the local Nusselt number increase by using perforated plate installed between impinging jet nozzle and target plate. Their work studied the effect of Reynolds number, pitch-to-hole diameter ratio p/d_1, hole diameter on perforated plate d_1, plate-to-target surface distance h_z/d_1, nozzle-to-target surface distance

H/d and the shape of the perforated hole. They found that as the perforated-to-impinging plate distance decreased, the more active interaction among the jets rapidly increases the rate of the heat transfer.

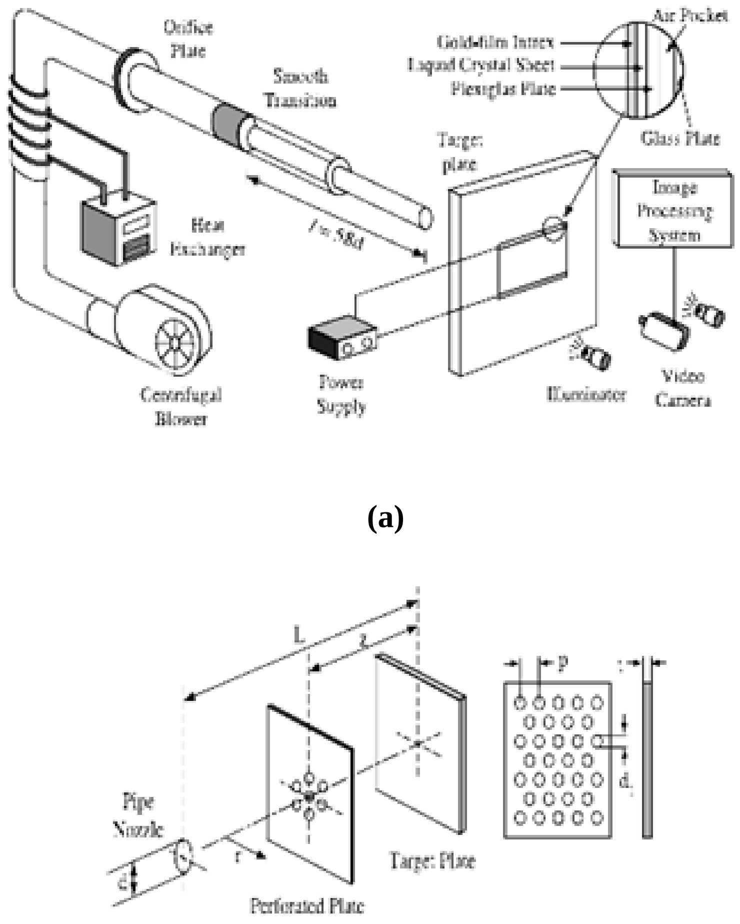

(a)

(b)

Figure 2.5 Schematic diagram of (a) experimental apparatus (b) set up of Lee et. al [15]

The study of Lee et al. [15] found that the rate of heat transfer increases as *H/d*, h_z/d_1, d_1 (see Fig. 2.5) decreases at the perforated plate-to-target surface distance of 2. The maximum Nusselt number occurs with the condition $H/d = 2$, $h_z/d_1 = 1$ and $d_1 = 4$. The

Nusselt number was higher for square hole than the round hole with increasing h_z/d_1. They concluded that the average Nusselt number is about two times higher with perforated plate than without the perforated plate at the stagnation region.

In 2002, Camci [33] proved that self-oscillating (at a frequency of 20 Hz to 100 Hz) impinging-jet configuration is extremely beneficial in enhancing the heat removal performance of a conventional (stationary) impinging jet. His work included Reynolds number at 7500, 10,000 and 14,000 at various nozzle to plate distances x/d = 24, 30, 40, 50, 60 (see Fig. 2.6). A heat transfer coefficient increase from 20 to 70% was found over the stationary jet values. He added two communication ports at the throat section to create a flapping mode for more effective thermal transport enhancement. By this he also increased the extent of stagnation region on the target plate. He suggested the technique can be used in future aircraft anti-icing system and other fields.

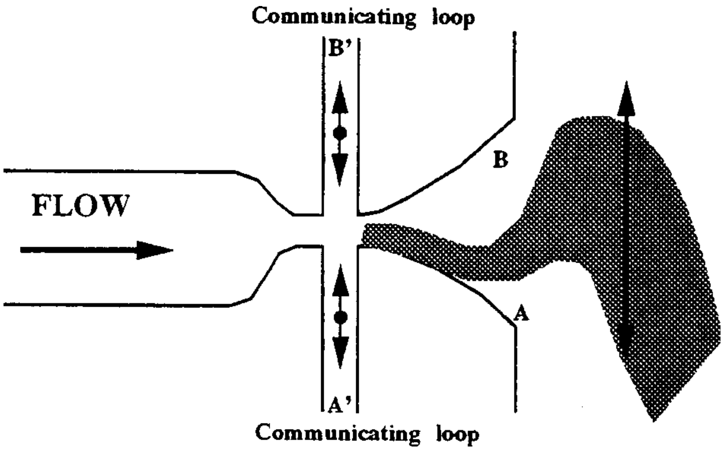

Figure 2.6 A planar jet with self sustained oscillations by Camci [33]

In 2002, Srinath et al. [34] investigated the effect of dimple location underneath the jets along with effect of dimple depth. Reynolds number varied from 4,800 to 14,800. They used 48 impinging holes of 0.635 cm diameter in an array of 12 columns and 4 rows as shown in the figure. The jet-plate to target-plate spacing *H*/*D* is 3×0.635 cm and jet-to-jet spacing *S*/*D* is 4×0.635 cm as shown in Fig. 2.7. Two dimple depths were used: 0.3175 and 0.15875 cm. Their results revealed that the dimpled surface, in-line (jet impinging directly onto the dimple) or staggered (jet impinging between the dimples) with respect to jet location, produce lower heat transfer coefficient than the non-dimpled target surface. They said that the bursting phenomena associated with flow over dimples produce disturbances of the impingement jet structure resulting in lower levels of heat transfer coefficient unlike in channel flow where bursting phenomenon produces local turbulence.

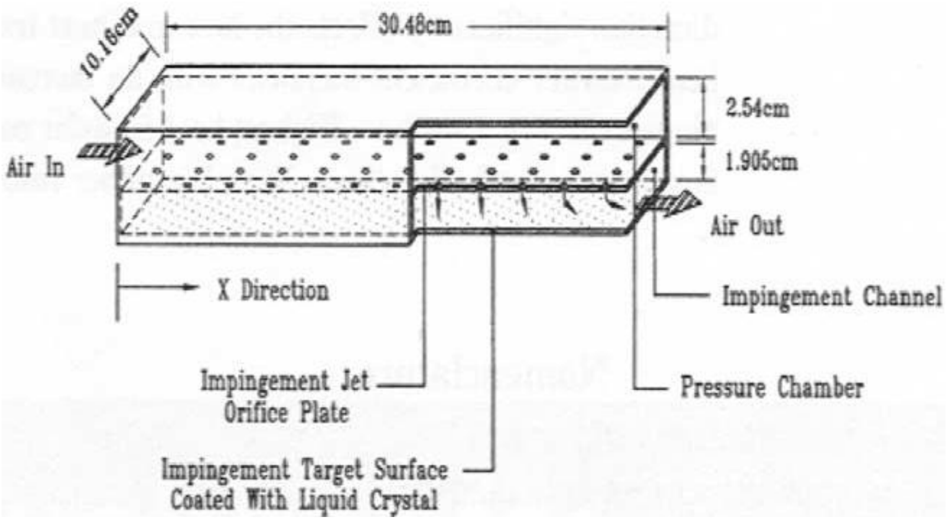

Figure 2.7 Experimental setup of Srinath [34]

In 2004, Herbert et al. [35] used Fluent version 5.5 to study the results of different turbulence model for jet impingement case. They used $y^+ = 0.5$ with the grid accommodating 150,000 to 200,000 cells. In that case, the temperature of the wall was a little more than the jet temperature and they used two-zonal turbulence model at the wall. They used the correlation given by Schlunder and Gnielinski [36] to analyze the results.

They concluded that the laminar region near the stagnation point cannot be calculated sufficiently well with the turbulence models and increasing the turbulence intensity at the nozzle exit does not improve the results. Hence, heat transfer cannot be calculated sufficiently well with any of the turbulence models in Fluent 5.5.

In 2004, Sarghini [37] did a transient numerical analysis of fluid flow and heat transfer from a planar jet impinging on a finite thickness substrate (see Fig. 2.8). Here a heated target substrate is subjected to a laminar cooling jet with a fully developed profile. He confirmed that the conjugate effect (heat transfer reversal) cannot be neglected during the initial exposition when an opposing cooling jet configuration is realized, for the largest investigated Reynolds number. He concluded that the transient heat transfer distribution showed the presence of heat transfer reversal which has to be considered in processes, as Chemical Vapor Disposition, where it is certainly appreciable and product-sensitive. A similar analysis was done by Shadlesky [38] in 1982.

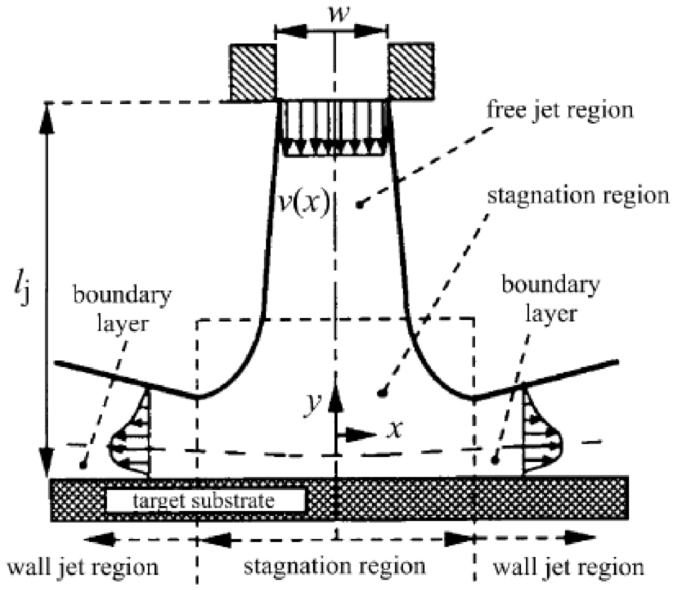

Figure 2.8 Jet Impingement flow region by Sarghini [37]

In 2004, Kanokjaruvijit et al. [39] used dimpled surface to promote the turbulence. They used 8×8 jet array surface facing the dimpled surface with jet-to-plate spacing *H/D* = 2, 4 and 8. Two geometries were tested, hemispherical cavity and cusped elliptical shapes as shown in the Fig. 2.9.

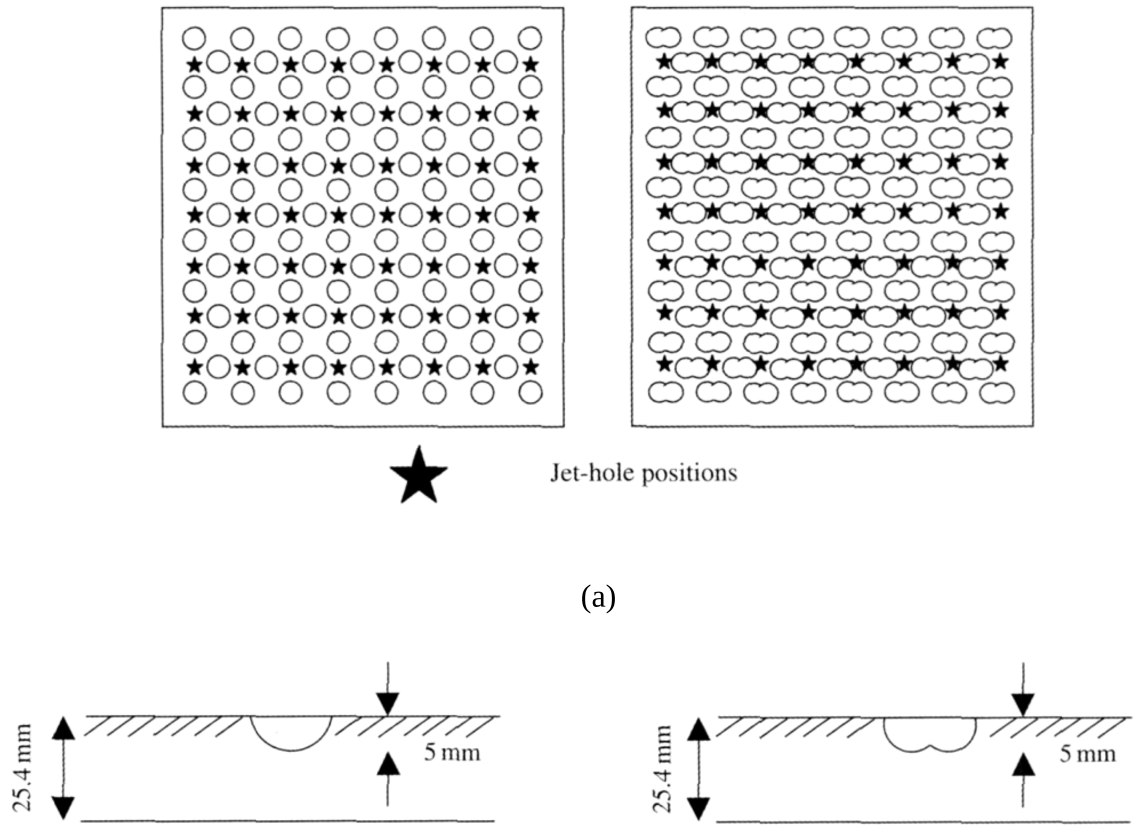

(b)

Figure 2.9 (a) Impingement on flat plate between dimples (shown as stars) (b) Hemispherical and cusp elliptical shaped dimple geometries

In their study, Kanokjaruvijit et al. [39] used ratio of jet to dimple imprint diameter was 0.59. The hemispherical dimple diameter was 17.32 mm and that for cusp shaped was 14.5 mm with center-to-center distance of 8.4 mm. The pitch and depth of dimples was 40 mm and 5 mm, respectively. They found that the heat transfer was best when *H*/*D* = 8 and that the two geometries had almost same heat transfer enhancement making hemispherical dimples more handy for manufacturers. Hemispherical dimples gave 8 to 68 % increase in heat transfer where as cusp elliptical shaped dimples gave 4 to 56 % increment. They suggested a research with more parameters like ratio of jet diameter to dimple diameter, dimple depth and pitch.

In 2005, Fregeau et al. [40] numerically investigated an array of hot-air jets impinging on three dimensional concave surface. They used a range of jet mach numbers, height-to-diameter ratio and jet spacing-to-diameter ratio. They derived the following correlation for maximum Nusselt number using Kriging Interpolation.

$$\begin{aligned} Nu_{\max} &= 0.282M \times 0.49\left(H/d\right) - 1.69\left(W/d\right) \\ &\quad - 0.85\exp\left[9.14\left(H/d\right)0.034\left(W/d\right)0.074\right] - 3 \end{aligned} \tag{2.3}$$

They observed Dual-Kriging method is a clever interpolation method for this case as it preserves the non-linear nature of the heat transfer distribution.

In 2005, Zhou et al. [11] compared the variations of flow structure and heat transfer characteristics of impinging air jets with respect to mesh solidity using different mesh screen locations and a little nozzle-to-plate spacing (see Fig. 2.10). They found that the heat transfer enhancement largely depends on nozzle-to-plate spacing *H/2R*, mesh solidity, and jet Reynolds number. The average Nusselt numbers was enhanced 1.38% for *H/2R* = 2.0. They suggested that the mesh screen effectively enhances heat transfer only when the nozzle-to-plate spacing is smaller than the potential core. For *H/2R* ≥ 4, on the contrary, the installation of a mesh screen leads to a decrease in the heat transfer rate.

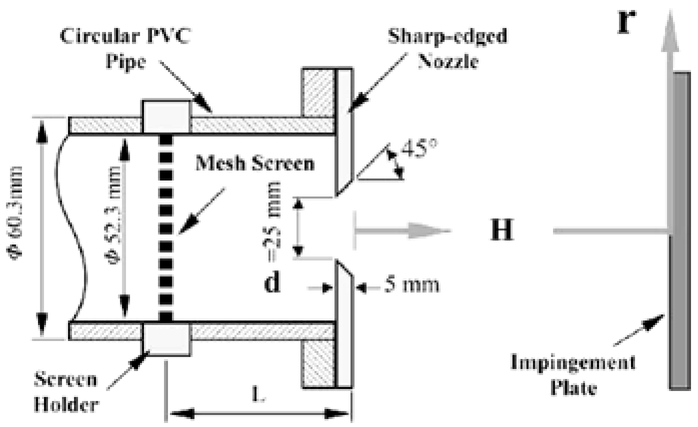

Figure 2.10 Nozzle exit configuration and coordinate system

Later in 2007, Zhuo et al. [14] studied the effect of jet Reynolds number and nozzle-to-plate spacing on local and average Nusselt number with a rectangular air jet. They correlated local Nusselt number and free stream turbulence intensity from the average heat transfer data along the axial direction as

$$\frac{Nu}{\mathrm{Re}^{0.5}} = 0.014 Tu\,\mathrm{Re}^{0.5} + 0.517 \tag{2.4}$$

and corresponding average values of Nusselt number and turbulence intensity along lateral direction as

$$\frac{Nu}{\mathrm{Re}^{0.5}} = 0.014 Tu\,\mathrm{Re}^{0.5} + 0.472 \tag{2.5}$$

Where *Tu* is turbulence intensity.

In 2006, Michael Papadakis [12] conducted an experimental and computational study on NACA 23012 airfoil. His investigation was concentrated upon the effect of piccolo design, diffuser geometry and hot-air temperature and mass flow rate on the system performance. He showed that after the chocking conditions at the jet exits were established, further increase in the hot-air mass flow will result in small skin temperature gain compared to gains obtained by the increasing air temperature.

In 2007, Saeed and Al-Garni [13] studied the effect of single array of jets, two staggered arrays of jets at different stagger angle (10 and 20 degs) and a case with etched/channel surface. They found that the single array and the array with a 20-degs stagger yield better surface heat transfer than the 10-deg stagger. A 2–3 times better surface heat transfer was found in case of etched/channel surface.

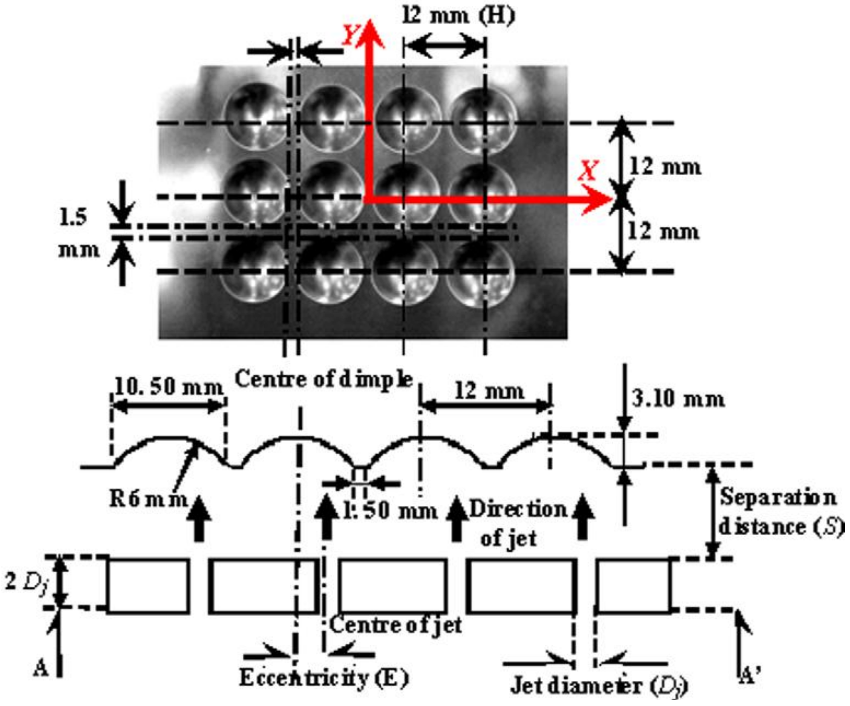

Figure 2.11 Dimple geometry and set up of Chang et al. [41]

In 2007, Chang et al. [41] examined the jet impingement heat transfer on dimpled surface (see Fig. 2.11) with Reynolds number varying from 5,000 to 15,000 and ratio of jet spacing to diameter ($S/2R$) varying from 0.5 to 10. They acquired data from three eccentricities *E* between jet-center and dimple-center of 0, 1/4 and 1/2 dimple-pitch *H*. They concluded that the dimples considerably modify the inter-jet mechanism and induce bursting phenomena in association with the vertical flow structure. Average Nusselt number of center jet region over the dimpled surface systematically increased with the increase of *E/H* ratio. They confirmed a general data trend which indicates that the increase in *S/D* ratio exceeding the effective Re range results in the ratio of average Nusselt number for dimpled surface to average Nusselt number for smooth wall above unity.

In 2008, Park et al. [42] conducted experimental and numerical investigation on spherical and oval dimpled surface. A laminar air flow of Re = 500 to 1650 was passed over a plate dimpled on both sides as shown in the Fig. 2.12. Heat transfer enhancement of about 6% compared to a flat plate at the given Reynolds number was observed.

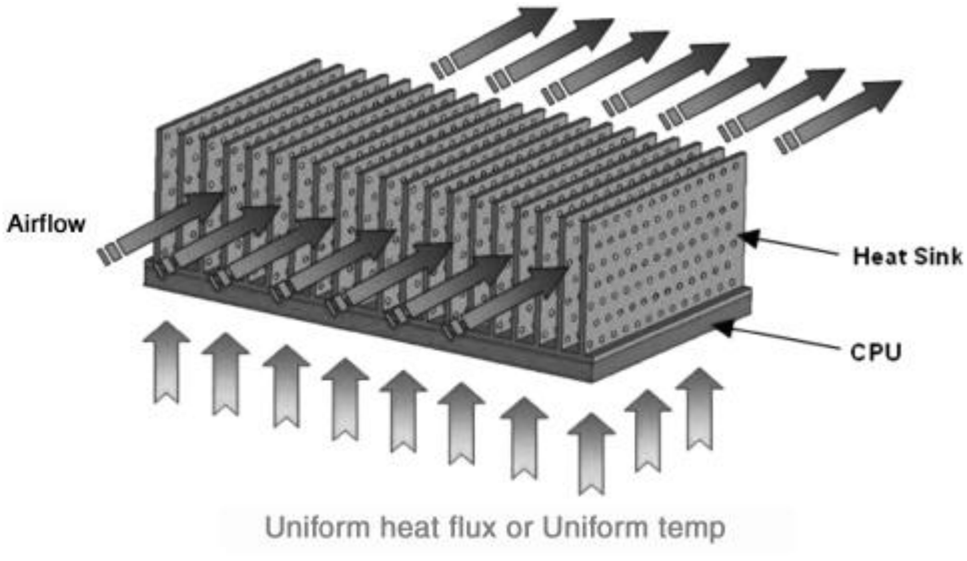

Figure 2.12 Heat sink with circular dimples of Park et al. [42]

The findings of their study were: (a) Heat transfer coefficient increases with increasing mass flow rate, (b) absolute heat transfer coefficient of numerical solutions gave lower values than experimental values, (c) thermal performance of both oval and circular dimples increased with increase in Reynolds number with circular dimples being more efficient, (d) vortex pairs in the recirculation region enhanced the heat transfer better in oval dimples than in circular dimples, and (e) the trailing edge region of the dimple has higher heat transfer as a result of reattachment of central and secondary vortex flow.

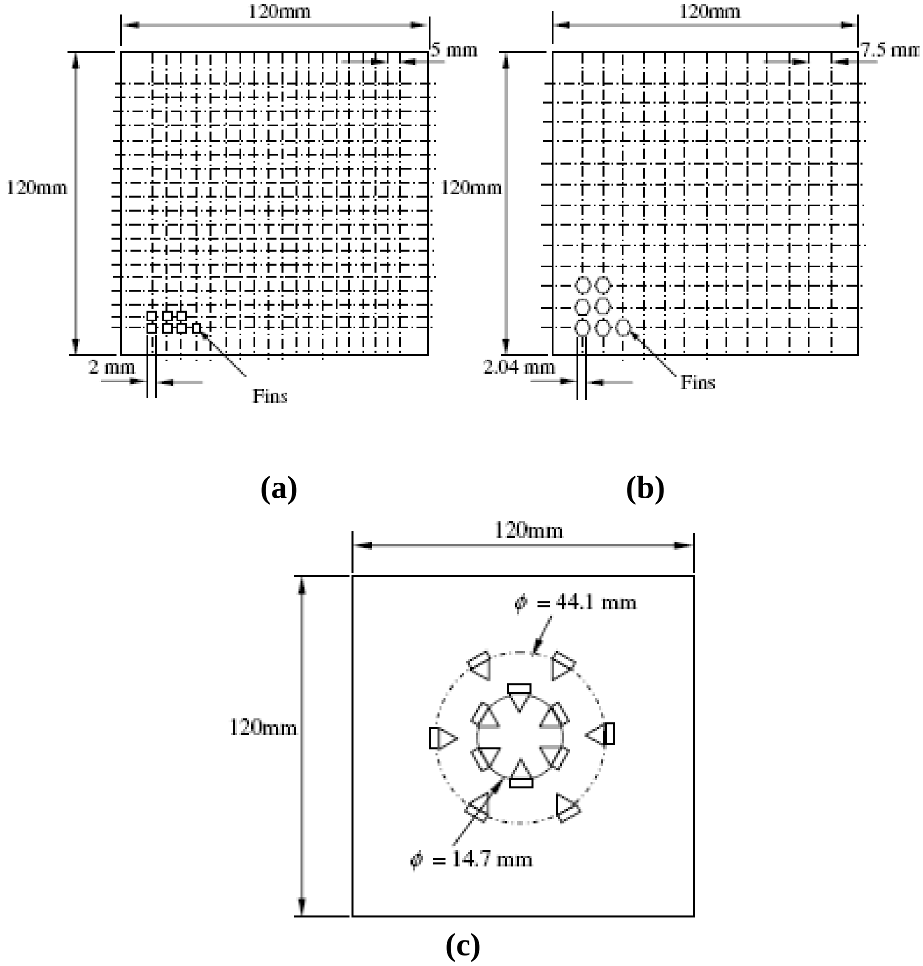

(a) **(b)**

(c)

Figure 2.13 (a) Details of cubical finned surface (b) Details of hexagonal finned surface, and (c) Details of vortex generators of Nakod [43]

In 2008, Nakod et al. [43] experimentally studied the effect of finned surfaces and surfaces with vortex generators on local heat transfer coefficient between impinging circular jet and flat plate. They varied Reynolds number and jet-to-plate spacing from 7,000 to 30,000 and 0.5 to 6, respectively. Fins of cube and hexagonal prism shape were used while vortex generators of equilateral triangle shaped with 4 mm sides each were circularly placed at a radial distance of φ as shown in the Fig. 2.13. They found an increase in the heat transfer coefficient up to 77% for hexagonal fined surface, nozzle-plate spacing of 0.184 and Reynolds number of 7000. For vortex generator the heat transfer coefficient was as high as 110% for a single row of six vortex generators at a radius of 1 nozzle diameter and Reynolds number of 25,000. They further found that at nozzle-to-plate distance of 0.5 and 6 Nusselt number at stagnation region was at peak, stagnation point heat transfer is stronger function of Reynolds number than wall jet heat transfer. A 24 to 77% increase in heat transfer for finned surface was observed when compared to a smooth wall surface.

In 2009, Korichi et al. [44] periodically mounted obstacles in a channel with oblique plates as vortex generators as shown in the Fig. 2.14. They modified the direction of the flow towards the obstacle faces to be cooled and activated the self-oscillations using oblique plates placed periodically. Their study focused on analysis of flow evolution and heat transfer enhancement in the intermediate and low Reynolds number range (250-1000) without recourse to turbulent flow. The hydraulic diameter and velocity were varied from 200 to 2,000 and 0.3 to 5 m/s, respectively. They found that the presence of vortex generators at the upper surface is a powerful mean to enhance the heat transfer compared to basic grooved channel. A 200% increase in heat transfer was obtained for Re = 600.

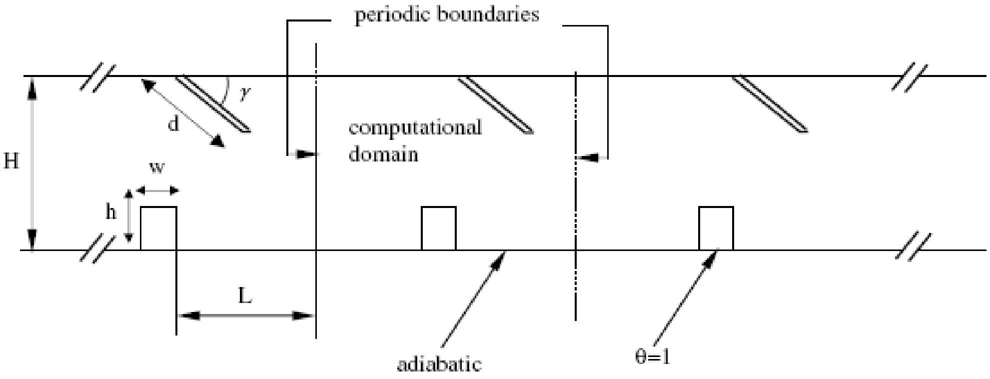

Figure 2.14 Channel with oblique plates and obstacles investigated by Korichi et al. [44]

Heat transfer enhancement techniques generally incorporate turbulence in the flow. Turbulence has been a helping phenomenon in aviation design. Apart from delay in flow-separation on a wing, turbulence helps increase in heat transfer by reducing the boundary layer near the wall. Some of the common techniques to create turbulence are as follows:

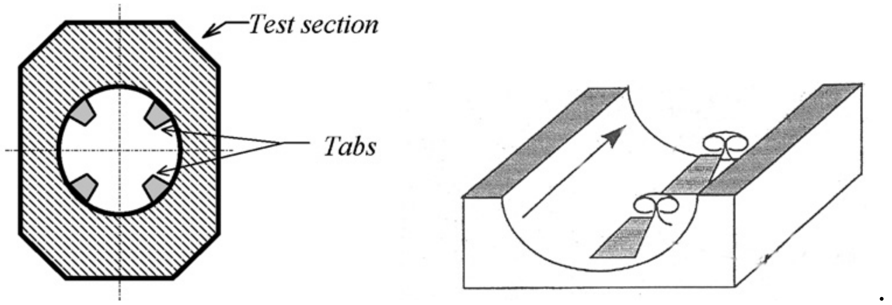

Figure 2.15 Vortex generators investigated by Mokrani et al. [45]

In 2009, Mokrani et al. [45] experimentally studied the effect of cascade of longitudinal vortices on the turbulence structure of flow inside a tube equipped with seven rows of vortex generators. The tabs (vortex generators) are trapezoidal in shape fixed at 30^o angle to the wall as shown in the Fig. 2.15. Reynolds number was varied from 1500 to 15000. Effect of Reynolds number on mean velocity distribution was analyzed and it was revealed that two mechanisms of transverse momentum transport are in competition. They stated that the momentum transport associated with longitudinal vortices tends to increase the deformation, while turbulent diffusion tends to homogenize the momentum distribution. The turbulence intensity in the flow substantially increased from 5% to 17%.

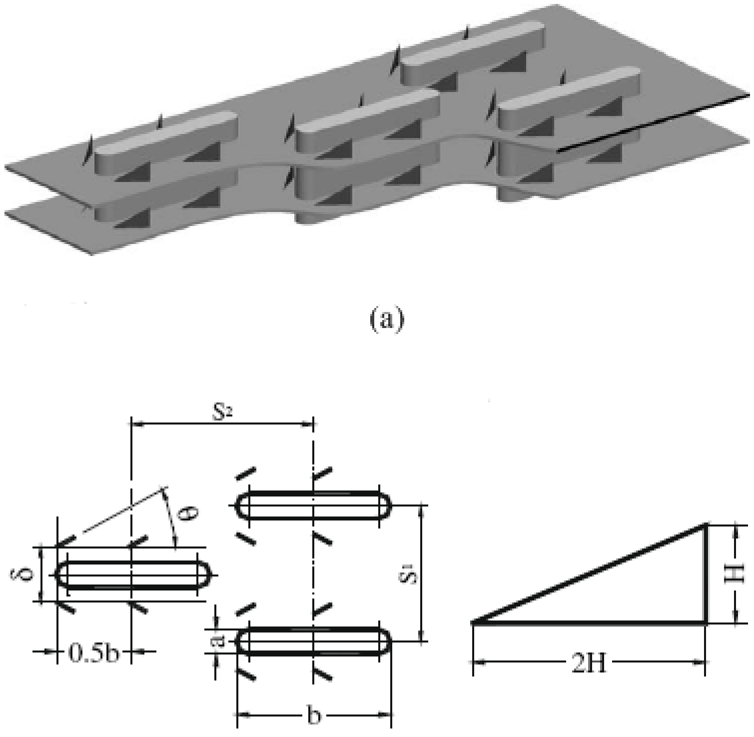

(a)

(a) **(c)**

Figure 2.16 (a) Isometric view of tube bank, (b) dimensions of tube bank and (c) dimensions of vortex generator

In 2009, Chang et al. [46] used cross averaged absolute vorticity flux in the main flow direction to specify the intensity of the secondary flow produced by vortex generators. Their set up included a flat tube bank with three-row tubes with vortex generators as shown in Fig. 2.16 (a). A tube along its length (b = 46.3 mm, a = 6.3mm,) has two vortex generators of shape as in Fig. 2.16 (c) at an angle θ = 35°. The transversal and longitudinal pitch between flat tubes are S_1 = 40 mm and S_2 = 55 mm. The span distance δ between the vortex generators of height H=4mm, is 12.6mm. The Reynolds number was about 1,300. They concluded that the span average Nusselt number has nearly the same tendency with cross-averaged absolute vorticity flux normal to the cross section except at the beginning region of the boundary layer. They also found that a similar trend was followed by Nusselt number and average absolute vorticity flux normal to the cross-section. In most of the cases, they observed that, secondary flow cannot greatly change the boundary layer characteristics and the average absolute vorticity flux cannot quantify the effects of developing boundary layer on convective heat transfer.

Numerous experiment investigations have been carried out to enhance the flow field on jet impingement. Investigators used obstructions like vibrating cylinders to modification of jet orifice itself. Many used mesh in front of jet in order to enhance the heat transfer on the target plate. When jet application is more widely used, changes in surface were made. Using dimpled surface was one of the major areas of research. In internal flows, vortex generators were applied wherever the need of turbulence was found. Although, obstructions were used, they are only a few models where innovators have designed and succeeded. Mesh and cylinder were only few design models to be used in jet intermittency. Having studied the heat transfer enhancements techniques found in literature for use in conjunction with aircraft anti-icing system. Dimpled surface were used but only for an array of jets. Hence, cavity effect on jet impingement was never been studied. Vortex generators were widely simulated in 3-D domain. Flows through/around pipes were mainly studied for the effect of VGs. Although, vortex generators strictly needed a three-dimensional domain to design, model and visualize the concept, enhancing heat transfer on the wall-jet region was never been attempted. With these ideas in mind, we propose the following objectives of this study.

2.1 Objectives

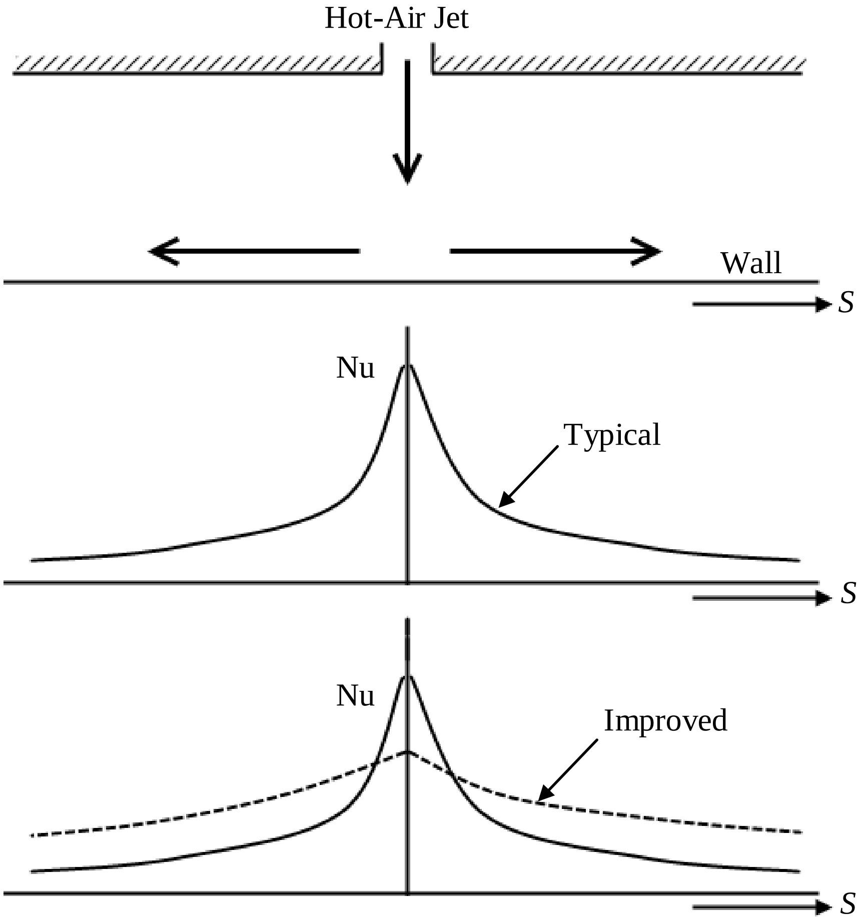

Figure 2.17 Typical and improved surface heat transfer characteristics

Fig. 2.17 shows a typical heat transfer distribution from the stagnation point through the wall-jet region along the impinging wall. On x-axis, the distance on the impinging wall is measured in a dimensionless quantity *S*. The heat transfer is measured in terms of Nusselt number along the y-axis. On observing closely, a maximum heat transfer is observed at the stagnation region with a sharp drop-off past the stagnation region. A lower heat transfer is observed therein along the wall-jet region. It was observed that heat transfer at the stagnation region exceeds the necessary value needed to melt the ice accumulated on the outer side of the impinging wall. Contrary to this, the heat on the wall-jet region was not high enough. Thus, improved heat transfer characteristics were desired where a uniform heat transfer distribution is obtained.

In this study we propose to study few mechanisms to enhance heat transfer outside the stagnation region (wall-jet region) as shown in Fig. 2.17. These mechanisms are classified as follows

a) Jet flow obstructions to enhance turbulence or cause the jet to spread.

b) Surface liners or restricted channels

c) Wall flow or surface obstructions such as vortex generators or cavities

2.2 Approach to the Problem

The steps that were taken to carry out the numerical investigation of the models are as follows

1. Numerical model of single jet impingement using the commercial CFD software FLUENT.

2. Study and validate the various turbulent models
3. Model the following
    - i. Jet-flow obstructions
        - (a) Triangles
        - (b) Cylinder
        - (c) Wedge
    - ii. Surface liners
        - (a) Channel
    - iii. Wall-flow obstructions
        - (a) Vortex generator
        - (b) Cavity
4. Document and compare the surface heat transfer distribution (average and local Nu) outside the impingement region.
5. Make recommendations for future study.

CFD was used to model and numerically simulate the various heat transfer enhancement mechanisms. In this, various turbulence models are investigated to validate the results with the empirical correlations. The commercial CFD software FLUENT 6.2 was used in this study. Sparlart-Allmaras, Standard, Realizable and RNG k-ε turbulence models are simulated for a steady state condition in FLUENT. The parameters that yield results closest to the empirical flat-plate heat transfer correlations was used for investigation of various heat transfer mechanisms studied in this work.

CHAPTER 3

MATHEMATICAL MODEL

Fluid behavior in the real world follows few basic governing equations. The science of fluid dynamics comprises of these fundamental governing equations - the mass, momentum and energy conservation equations. These equations follow the physics in nature. They are the mathematical forms of fundamental physical principles on which fluid dynamics is based.

3.1 Governing Equations

The governing equations are basically derived from three laws of conservation. They are

1. Conservation of mass (continuity)
2. Conservation of momentum (Newton's Second Law of Motion)
3. Conservation of energy (The First Law of Thermodynamics)

Velocity V, thermodynamic pressure p and absolute temperature T are the three unknowns to be found from the above given three equations where pressure and temperature are considered to be the two required independent thermodynamic variables. Four other thermodynamic variables are present in the final form of conservation equation.

They are density ρ, enthalpy h, and the two transport properties; viscosity μ and thermal conductivity k. Addition equations are then needed for density and turbulence transport properties to properly close the problem.

3.1.1 Conservation of Mass

The conservation of mass law in vector form when applied to a fluid passing through an infinitesimal, fixed control volume yields the following equation of continuity using the *Eulerian approach*

$$\frac{\partial(\rho)}{\partial t} + \nabla.(\rho V) = 0 \tag{3.1}$$

Rate of density increase + Rate of mass flux = zero

where ρ is the fluid density and V is the fluid velocity

3.1.2 Conservation of Momentum

Newton's Second Law of Motion applied to a fluid passing through an infinitesimal, fixed control volume yields the following momentum equation

$$\frac{\partial(\rho V)}{\partial t} + \nabla.\rho VV = \rho f + \nabla.\Pi_{i,j} \tag{3.2}$$

Rate of increase of momentum + Rate of momentum lost by convection = Sum of all forces

The stress consists of normal stresses and shearing stresses and are represented by the components of the stress tensor $\Pi_{i,j}$. f is the force per unit mass.

3.1.3 Conservation of Energy

The First Law of Thermodynamics when applied to a fluid passing through an infinitesimal, fixed control volume yields the following energy equation

$$\frac{\partial E_t}{\partial t} + \nabla . E_t V = \frac{\partial Q}{\partial t} - \nabla . q + \rho f . V + \nabla . \left(\Pi_{i,j} . V \right) \tag{3.3}$$

where E_t is the total energy per unit volume given by

$$E_t = \rho(e + \frac{v^2}{2} + \text{potential energy} + \ldots)$$

q is the energy flux given by

$$q = -\mathrm{k} \nabla T \tag{3.4}$$

e is the internal energy per unit mass

$\nabla . E_t V$ is the rate of total energy lost by convection through the control surface

$\frac{\partial Q}{\partial t}$ is the rate of heat produced per unit volume by external agencies

$\nabla . q$ is the heat lost by conduction through the control surface

3.1.4 Equation of State

In order to relate the thermodynamic properties (μ, k) to thermodynamic variables and to establish relation between the thermodynamic variables (p, ρ, T, e, h) so that the system is closed, the equation of state for ideal gas is utilized

$$p = \rho R T \tag{3.5}$$

where *R* is the gas constant

3.2 Turbulence Modeling

In a turbulent flow problem, the set of governing equations stated above are insufficient due to fluctuating products including Reynolds stresses and fluxes. Hence, the averaged conservation equations have more unknowns in such situations. This deficiency of governing equations is termed as closure problem. Consequently, there is a need for additional equations to solve the closure problem, turbulence modeling provides additional equations to solve the mean flow equations. These additional equations may be based on empirical observations or physical reasoning and therefore, an ideal turbulence model should introduce the minimum amount of complexity while capturing the essence of the relevant physics.

3.2.1 Turbulence Modeling Equations

Higher values of friction, drag and pressure drop are associated with turbulent flows. Hence, a higher capacity is seen in turbulent boundary layer to negotiate with unfavorable pressure gradients. *Direct numerical simulation* (DNS) method is generally used to solve turbulent flow problems, but it requires resolution of relevant length scales (within the problem domain) including time steps for a steady flow. *Large-eddy simulation* (LES) approach is used for isotropic model and needs large-scale structure of the turbulent flow to be computed directly. Although LES method take almost 1/10th of time than DNS, a time-averaged Navier-Stokes equation is better where stress gradients and heat flux quantities associated with the turbulent motion are dealt in detail. The LES equations are also known as Reynolds equations of motion or the *Reynolds averaged Navier-Stokes*

(RANS) equation. All the conservation equations can be written in the Reynolds average form. Many turbulence models exist in literature today. The choice of the turbulence model depends upon the physics associated with the flow, level of accuracy needed and available time and computational resources.

The turbulence model are classified as

1. Algebraic models
2. One-equation models
3. Two-equation models
4. Stress-transport models

Two-equation turbulent models not only account for turbulence velocity but also for length scale. They are the simplest models which succeed even for the flows in which length scale cannot be prescribed empirically. The most common and widely used two-equation turbulence models are the: (1) k-ε model, and (2) Realizable k-ε model.

3.3 k-ε and Realizable k-ε model

k-ε turbulence models usually differ in the method of calculating turbulent viscosity, turbulent Prandtl numbers governing the turbulent diffusion of k and ε, and the generation and destruction terms in ε equation. Realizable k-ε model satisfies certain mathematical constraints on normal stresses and is consistent with the physics of turbulent flows. Traditional k-ε models poorly solve the dissipation equation, especially in spreading rate for axisymmetric jets where as realizable k-ε model uses two new formulae in this aspect.

A new eddy-viscosity formula and a new model equation for dissipation ε based on dynamic equation of the mean square vorticity fluctuation. Realizable k-ε model have been excessively validated for a wide range of flows, including rotating homogenous shear flows, free flows including jet and mixing layers, channels and boundary layer flows and separated flows. This model has performed substantially better than that of Standard k-ε model. The most important and noteworthy advantage of realizable k-ε model in the current numerical investigation is that it can predict the spreading rate for axisymmetric jets and also planar jets.

3.4 Boundary Conditions

Boundary conditions play a vital role in defining the domain. They specify the flow and thermal variables on the boundaries of the physical model. The boundary conditions involved in the present domain are shown in Fig. 3.1. A vertical plane along the jet centerline was considered inside the slat as show in Fig. 3.1 (a). This plane can be stretched straight to form a simple axis symmetric rectangular domain (BB´CC´) as shown in Fig. 3.1 (b) where the OD or OD´ is the line/axis along which the domain is symmetric. The piccolo wall is stretched as AB and A´B´ with jet diameter as AA´. Similarly, the impinging surface is stretched CC´ with D or D´ at stagnation point. BC and B´C´ are the outlets for the hot air actually going behind the piccolo tube into the ambience, as seen in Fig. 3.1 (a). It should be noted that in Fig. 3.1 (b), the domain is symmetric along the jet centerline OD or OD´. Also results obtained in such a domain are axis symmetric. Hence, neglecting the shaded region (OA´B´C´D´) and considering the unshaded region (OABCD) saves much time, computer resources and data redundancy.

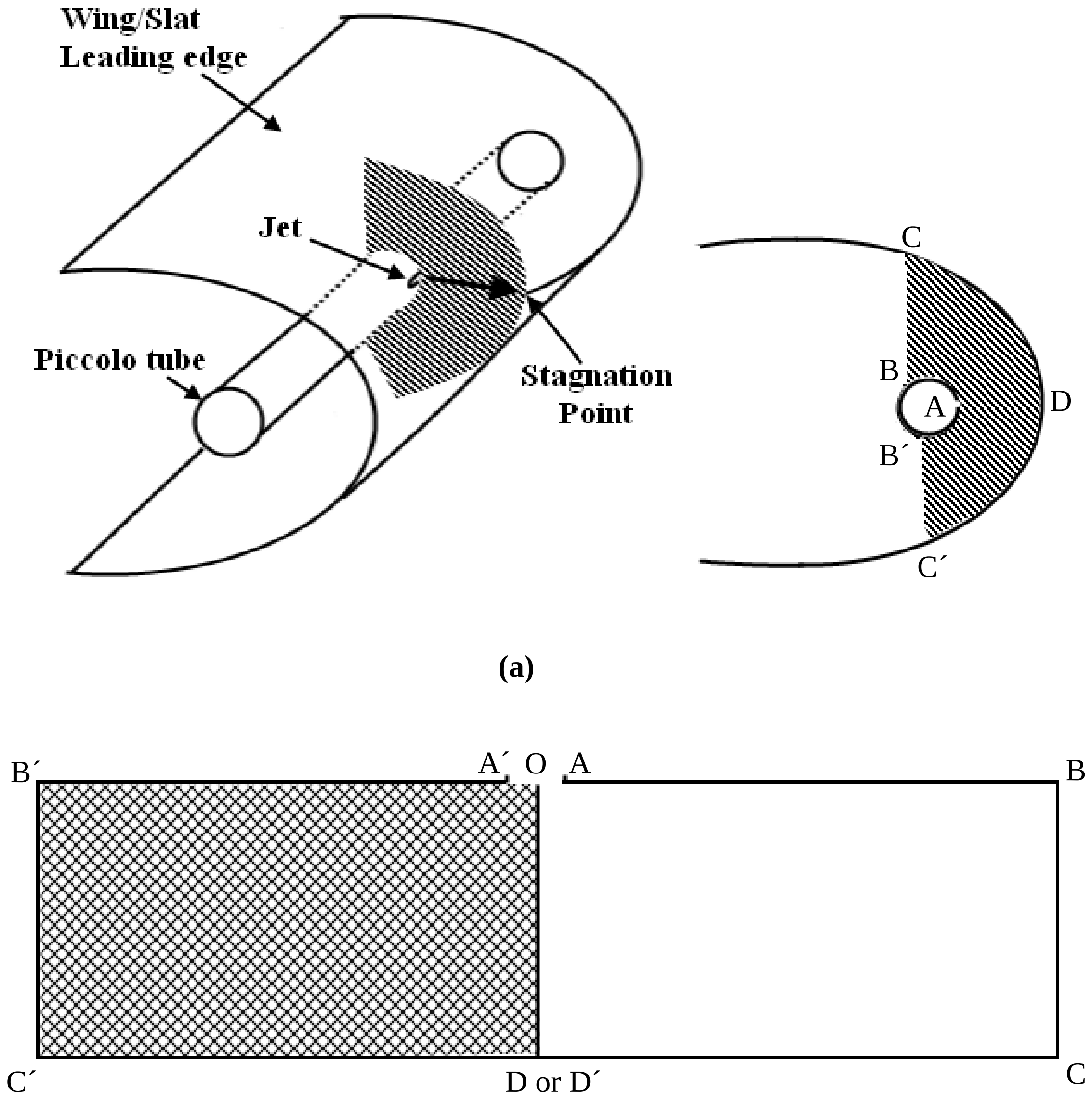

(a)

(b)

Figure 3.1 (a) Isometric and cross-sectional view of domain location,

(b) Domain boundaries

Table 3.1 Domain boundary specifications

Label	Boundary type
OA	Mass Flow Inlet
AB	Wall (Piccolo tube)
BC	Pressure Outlet (Ambient)
CD	Wall (Impinging surface)
OD or OD´	Symmetry (Jet centerline axis)

3.4.1 Mass Flow Inlet

The mass flow rate inlet boundary condition is used to model the flow inlet boundary. Air acting as ideal gas is considered to flow out from a jet with Reynolds number 68,353 (V = 34.959 m/s) and viscosity ($v = 2.254 \times 10^{-5}$ kg/m-s) at 400 K.

3.4.2 Pressure Outlet

Pressure outlet boundary condition is used to define the static pressure at flow outlets. An added advantage of this type of outlet boundary condition is that it defines scalar variables in case of back flow. The pressure outlet boundary condition requires the specification of static (gauge) pressure at the outlet boundary. Since the outlet conditions are ambient, zero gauge is defined as the pressure for pressure outlet boundary condition. Ambient pressure is defined as the operating pressure.

3.4.3 Walls and Symmetry

The boundary condition of the impinging wall is a stationary isothermal wall at 260 K temperature exposed to ambient temperature (much lower than the wall temperature) on the other side. The piccolo wall is kept at a constant heat flux with a thickness of 0.002 m.

3.4.4 Numerical Scheme.

FLUENT solves the governing integral equations for the conservation of mass, momentum and energy using *segregated* or *coupled* solver. A 2D segregated implicit solver is used as it solves the governing equations sequentially performing solution loop before convergence is reached. First, the fluid properties are obtained and momentum equation is solved. Then the pressure corrections are made by continuity equation considering the current pressure and mass flow rate values. All the other equations including energy, turbulence and scalar equations are solved and checked for the convergence criteria.

3.4.5 Properties

3.4.5.1 Air

Ideal gas law is considered for the fluid (air) at 400 K temperature with viscosity derived from Sutherland's formula given as

$$\mu = \mu_o \frac{T_o + C}{T + C}\left(\frac{T}{T_o}\right)^{3/2} \tag{3.6}$$

where μ and μ_o are dynamic viscosity and reference viscosity (μ_o = 18.27×10^{-6} Pa.s), T and T_o are input and reference temperature, and C is Sutherland's constant = 120 K for air.

Specific heat of air is specified in the polynomial form as (in J/kg-K)

$$c_p = 1.045356\times10^{3} - 3.161783\times10^{-1}T \\ + 7.083814\times10^{-4}T^{2} - 2.705209\times10^{-7}T^{3} \tag{3.7}$$

Thermal conductivity of air is specified in polynomial form and is given by (in W/m-K)

$$k = -4.937787\times10^{-4} + 1.018087\times10^{-4}T \\ - 4.627937\times10^{-8}T^{2} + 1.250603\times10^{-11}T^{3} \tag{3.8}$$

which are accurate for $200 \le k \le 600$ K

3.4.5.2 Wall

Properties of aluminum are unitized for the wall material. The isothermal wall is at 260 K temperature and has a thickness of 0.002 m.

CHAPTER 4

NUMERICAL MODEL DEVELOPMENT

Numerical modeling is initiated by first modeling the domain in modeling software. The final output of this modeling is a prototype of the stated problem which can be used for further processing. Generally, the model is designed and divided into tiny control volumes which constitute a grid.

4.1 Grid

Grid generation is often considered as most important and time consuming part of CFD simulation. It is a process of subdividing the region to be modeled into a set of small control volumes. The quality of grid plays a direct role on the quality of the analysis. The solver will be more robust and efficient when using a well constructed mesh.

Usually there are three techniques used for grid generation for any flow domain

1. Structured Grid
2. Unstructured Grid
3. Hybrid Grid

In the present study, both structured and hybrid grids were used in modeling. The details will be explained later in this chapter.

4.1.1 Dimensions

From the Fig. 3.1 (b), the domain boundaries were estimated and their dimensions were modeled as shown in Fig. 4.1.

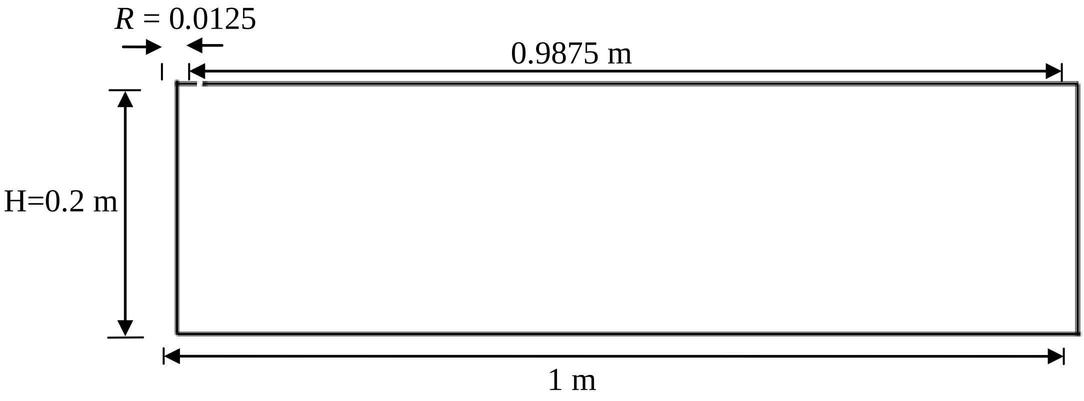

Figure 4.1 Dimensions of the computational domain

4.1.2 Structured Grid

Structured grid allows high degree of control as the user is free to place control points and edges to position the mesh. Structured mesh flow solver typically require low memory to execute the solution faster as they are optimized for structured layout of the grid. In the present study, modeling for the validation and study cases was conducted using a well structured grid within the rectangular domain as shown in the Fig. 4.2. The grid is compressed in one or more coordinate direction to properly resolve the various flow gradients near the walls.

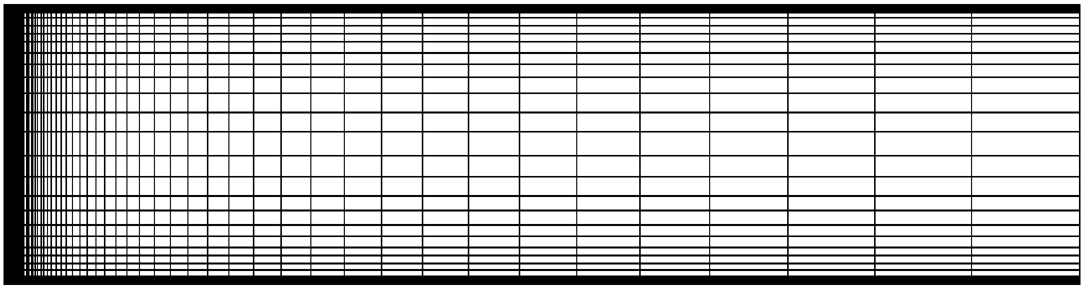

Figure 4.2 Structured grid domain

In the present case, the velocity profile near the walls has to be resolved; therefore, the grid is stretched towards or compressed near the walls. A higher velocity and pressure gradient can also be seen near the stagnation point and at the jet boundaries. The grid is thus concentrated towards the jet centerline. It can be easily assumed that the flow along the wall looses it energy as it moves away from the stagnation point. Keeping this in mind, the grid concentration at the right end of the domain is made coarse so as to save computational time and unnecessary calculations.

4.1.3 Hybrid Grid

A structured grid is more economical way of modeling and computationally solving a problem. However, there are many cases in which the geometry becomes complex and intricate where a structured grid becomes very difficult to construct. In such cases, the user is forced to use unstructured mesh to resolve all the regions of the domain. Unstructured grid uses an arbitrary collection of elements to fill the domain. Because the wedge arrangement is not a repeated pattern as in structured grid, the mesh is called unstructured. An advantage of such a grid is that it requires a very little input from the user and are numerically generated using different unstructured grid generation schemes.

Thus, the user has very little control over the elements and their arrangement. Hence, this type of grid generation is used when users encounter complex geometry which cannot be meshed using a structural pattern. A geometry may require unstructured grid generation but not in the entire domain. In such cases, a combination of structured and unstructured grid is used where only few faces in the modeling are subjected to the required type of grid. Such a combination of grid is called a hybrid grid. In the present study, there are few models which required hybrid grid generation. They are explained in the coming sections.

4.2 Selection of Turbulence Model

It is a fact that no turbulence model is a perfectly suitable model for all the classes of problems. The choice of turbulence model depends upon few considerations such as the physics in it, class of the problem, level of accuracy needed, time and computational resources available. Thus, in the present research different turbulence models are simulated with different grid resolutions.

4.2.1 Wall Treatment

The near-wall modeling significantly impacts the fidelity of numerical solutions. Accurate representation of the flow in the near-wall region determines successful predictions of wall-bounded turbulent flows. Traditionally, they are two approaches to modeling the near-wall region.

Wall function approach: In this approach, instead of resolving the viscosity-affected region, semi-empirical formulae called “wall function” are used between the wall and fully turbulent region. Furthermore, modifying the turbulence model to account the presence of wall is needed.

Near-wall model approach: In this approach, the viscosity-affected region is resolved with a mesh all the way to the wall. This is enabled by modifying the turbulence models.

Although, the wall function approach is economical, robust and reasonably accurate, it fails when there are severe pressure gradients or strong body forces involved in the flow.

In order to resolve the viscous sublayer, the height of the first control volume should stay within the boundary layer thickness. This height is measured by non-dimensional parameter defined as

$$y^{+} = \frac{\rho u_{\tau} y_{P}}{\mu} \tag{4.1}$$

where the friction velocity $\mu_{\tau} = \sqrt{\tau_{\omega} / \rho_{\omega}}$ and y_P is the distance from point P to the wall.

The value of y^+ depends upon the type of near wall treatment used. When using a wall-function, the log law is valid for $y^+ > 30$ to 60 and the linear (laminar) law at $y^+ < 11.225$. However, a y^+ value close to the lower bound ($y^+ \approx 30$) is most desirable. Similarly, when the enhanced wall treatment is employed to resolve the viscous sublayer, y^+ at the wall-adjacent cell should be of the order of unity. However, a higher range is acceptable as long as it is well inside the viscous sublayer. A similar guideline is observed for k-ε, k-ω and LES models; whereas for Spalart-Allmaras turbulence model, either a very fine near-wall mesh spacing (on the order of $y^+ = 1$) or a mesh spacing such that $y^+ \geq 30$ is required.

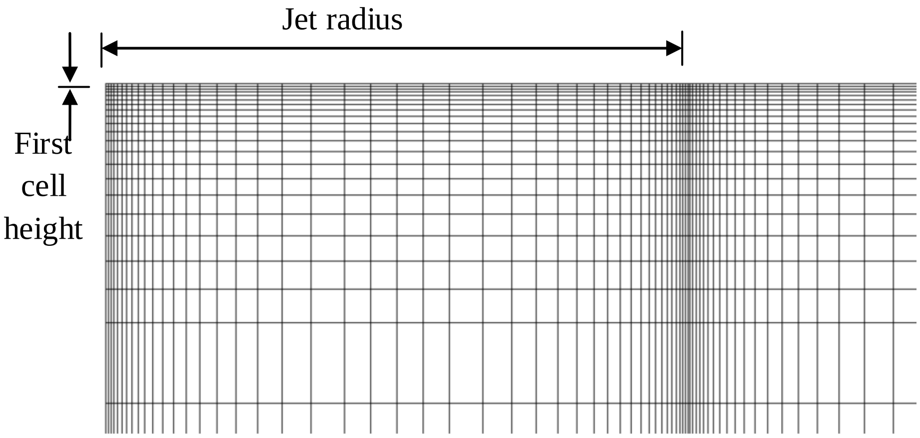

Figure 4.3 Mesh resolving viscous-effected region

An initial validation study was conducted to find the optimum value of y^+ required to satisfy the empirical correlation given by Martin [7] for a single slot nozzle.

In this study, a single slot jet impinging on a flat surface was investigated for y^+ values ranging from 1 to 5 for the following turbulence models.

1. The Spalart-Allmaras Model [47]
2. The Standard k-ε.Model [48]
3. The RNG k-ε Model [49]
4. The Realizable k-ε Model [50]
5. The Standard k-ω Model [51]
6. The Shear-Stress Transport (SST) k-ω Model [51]

The empirical correlation for surface heat transfer in terms of average Nusselt number given by Martin [9] is:

$$\left(\frac{\overline{Nu}}{\mathrm{Pr}^{0.42}}\right)=\frac{1.53}{x/S+H/S+1.39}\mathrm{Re}_S^m$$
$$m=0.695-\left[x/S+(H/S)^{1.33}+3.06\right]^{-1} \qquad (4.2)$$

Range of validity:

$$3000\le \mathrm{Re}_S \le 90,000$$
$$2\le x/S\le 25$$
$$2\le H/S\le 10$$

Thus for validation study, a slot width of S = 0.05 m, a slot height of H = 0.2 m was chosen. The average flow velocity was chosen to give a jet Re_S = 68,353, well within the range of Martin's correlation. The computational domain was modeled with same grid and mesh densities but different y^+ values along the wall. Each mesh file with different y^+ values was again run with different turbulence models to determine which turbulence model best satisfied the empirical correlation. The results of the validation study are presented next under the different turbulence models.

Since the results obtained from the numerical solution are in the form of local Nusselt number, they were integrated in order to compare and validate them with the above empirical data in terms of average Nusselt number. Trapezoidal rule which is an approximate technique for calculating the definite integral was used. If we consider the definite integral as shown in Fig. 4.4,

$$\int_a^b f(x)dx$$

Then we assume that *f*(x) is continuous on [*a*,*b*] and we devide [*a*,*b*] into *n* subintervals of equal length,

$$\Delta x = \frac{b-a}{n} \tag{4.3}$$

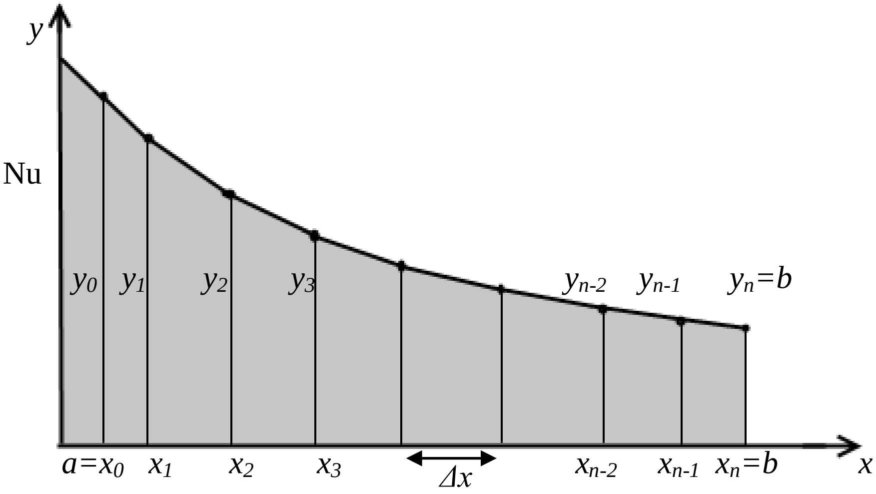

Figure 4.4 Approximating the graph of *y = f(x)* with line segments across successive intervals to obtain the Trapezoidal rule

Summing the definite integrals over each subinterval provides us with the approximation

$$\int_a^b f(x)dx \approx \frac{(y_o+y_1)\Delta x}{2} + \frac{(y_1+y_2)\Delta x}{2} + \ldots + \frac{(y_{n-1}+y_n)\Delta x}{2} \tag{4.4}$$

Which simplifies to the trapezoidal rule formula

$$\int_a^b f(x)dx \approx \frac{\Delta x}{2}(y_0 + 2y_1 + 2y_2 + ... + 2y_{n-1} + y_n) \tag{4.5}$$

Martin [9] used the following relation to determine the average Nusselt number from the local Nusselt number to given as

$$Nu_{ave}(x_n) = \frac{1}{x}\int_0^x Nu_{local}(x')dx' \tag{4.6}$$

or mathematically,

$$Nu_{ave}(x_n) = \frac{\Delta x}{2x}\left[Nu_{local}(x_0) + 2Nu_{local}(x_0 + \Delta x) + ... + 2Nu_{local}(x_n - \Delta x) + Nu_{local}(x_n)\right] \tag{4.7}$$

4.2.1.1 The Spalart-Allmaras Model

The Spalart-Allmaras model [47] solves a single transport equation for a quantity that is a modified form of the turbulent kinematic viscosity. Solving a single equation makes Spalart-Allmaras a simple, fast and reliable turbulence model. Spalart-Allmaras model has been used for aerospace applications involving wall-bounded flows with boundary subjected to adverse pressure gradient. A comparison of surface Nusselt number distribution between the empirical correlation and CFD predictions using computational grid with different y^+ along with the Spalart-Allmaras turbulence model is shown in Fig. 4.4. The ±15% empirical data lines are shown on all plots in the current study to indicate the spread in the experimental data.

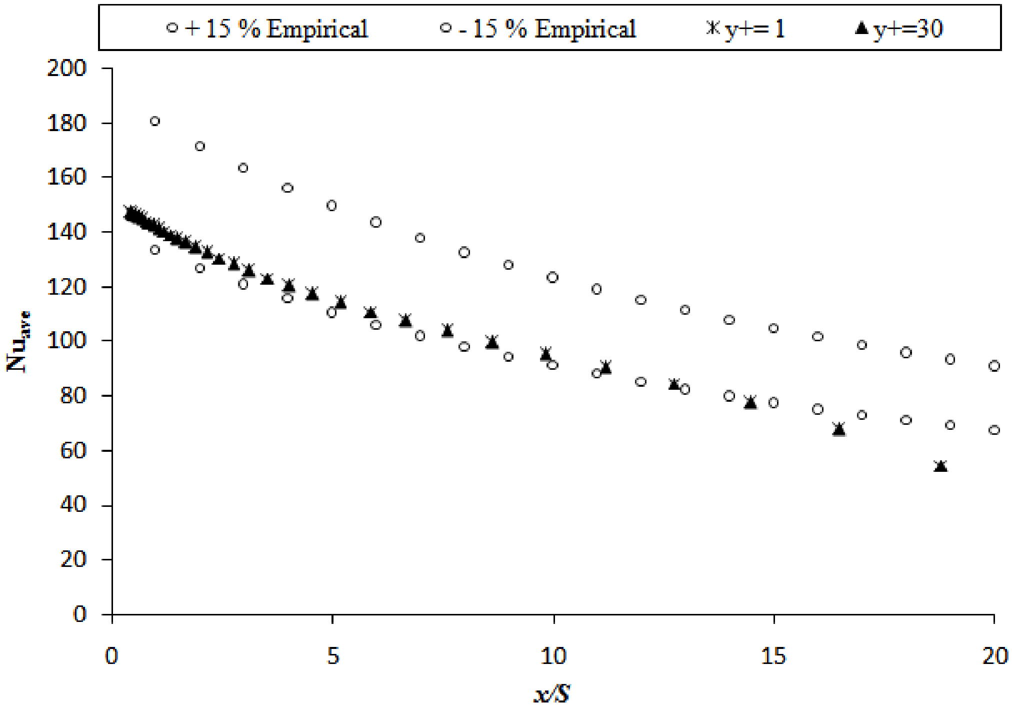

Figure 4.5 Comparison of empirical with numerical Nusselt number distribution at various y^+ using Sparlart-Allmaras tubulence model

From Fig. 4.4, it is evident that the Sparlart-Allmaras turbulence model satisfactorily calculates the heat transfer for about three-forth of the wall-jet region. The numerical results fall within the lower empirical data range near the stagnation region but fall below it past $x/S \approx 12$. A comparatively lower heat transfer is observed after $x/S = 15$.

4.2.1.2 The Standard *k*-*ε* Model

The standard $k-\varepsilon$ model [48] is a semi-empirical model and the derivation of the model equations relies on empiricism and phenomenological considerations. It determines turbulent velocity and length scales independently from two separate transport equations using two-equation model. The turbulence kinetic energy k and its rate of dissipation are calculated separately from two equations and the turbulent eddy viscosity is calculated by combining both *k* and *ε*. This makes the model robust, economic and reasonably accurate for a wide range of fully turbulent flows. Fig. 4.5 show the results obtained by solving standard *k*-*ε* model for various y^+ values.

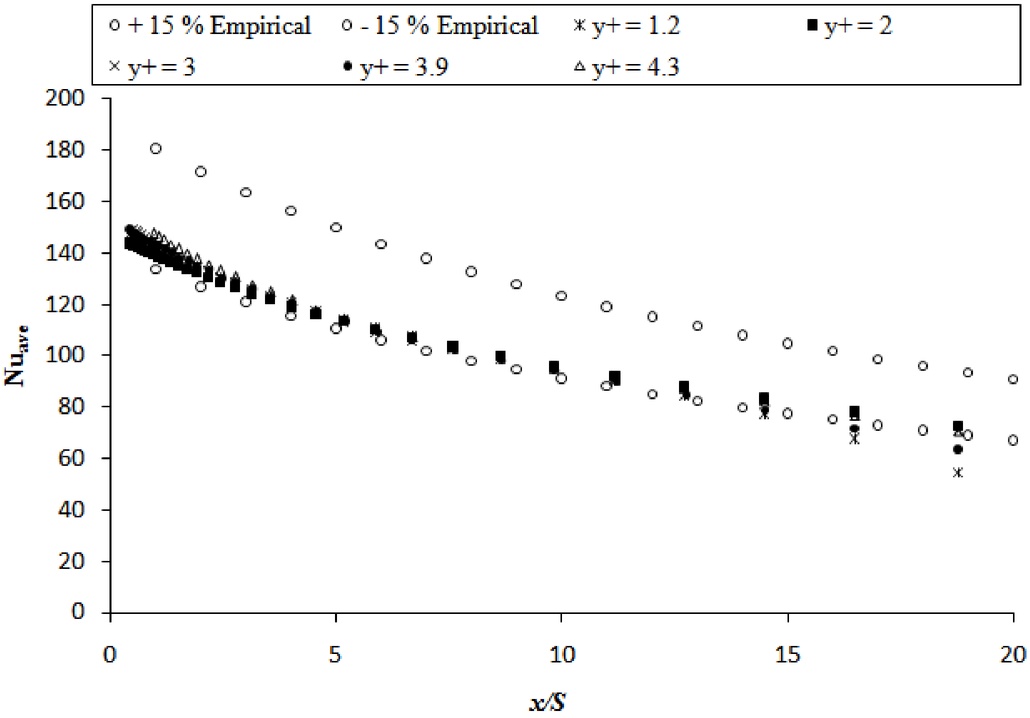

Figure 4.6 Comparison of empirical with numerical Nusselt number distribution at various y^+ using Standard *k*-*ε* tubulence model

Fig. 4.4 illustrates that the standard $k-\varepsilon$ model turbulence model satisfactorily calculates the heat transfer for $y^+ = 2$. The numerical results are well within the empirical range near the stagnation region and as well as wall-jet region for y^+=2. A higher value of y^+ results in unsatisfactory solution at far wall-jet region ($x/S \geq 15$) which makes $y^+ = 2$ a suitable value for wall treatment for this turbulence model.

4.2.1.3 The RNG *k-ε* Model

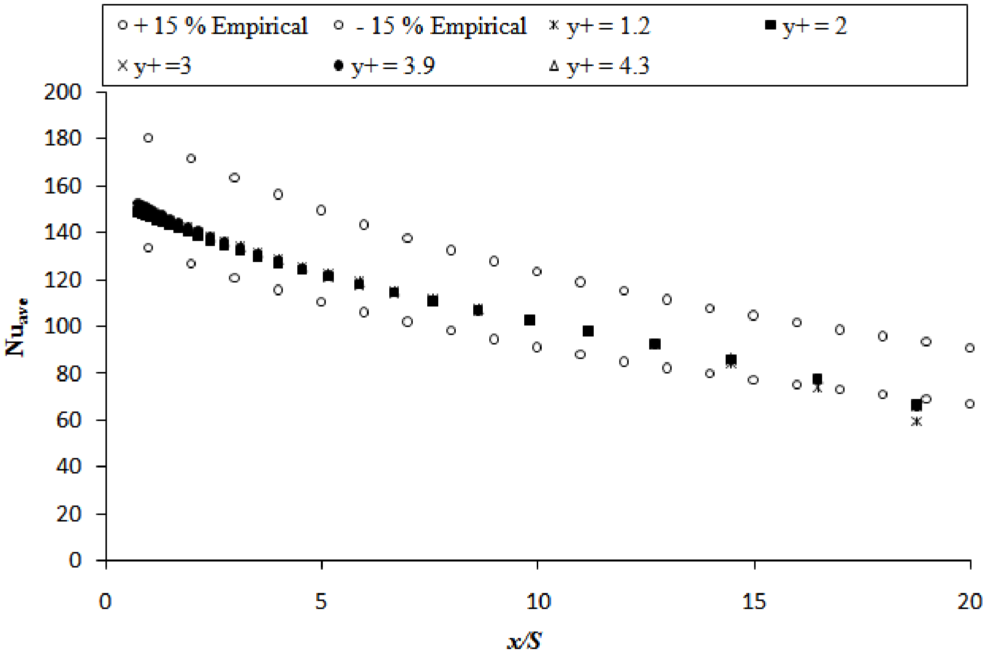

Figure 4.7 Comparison of empirical with numerical Nusselt number distribution at various y^+ using RNG *k-ε* tubulence model

Renormalization group (RNG) method [49] is a mathematical technique used to derive RNG-based $k-\varepsilon$ turbulence model from Navier-Stokes equation. The RNG $k-\varepsilon$ turbulence model employs additional terms and functions in the transport equations for k and ε when compared to standard $k-\varepsilon$ model. This model accurately calculates strained flows and swirling flows making it reliable for wider class of flows than the standard $k-\varepsilon$ model. Results obtained from the use of the RNG $k-\varepsilon$ model indicate better match with the empirical data spread than the standard $k-\varepsilon$ model (Fig. 4.6).

4.2.1.4 The Realizable *k*-*ε* Model

The Realizable $k-\varepsilon$ turbulence model [50] satisfied certain mathematical constraints on the normal stresses, consistent with the physics of turbulent flows. This turbulence model adopts a new eddy-viscosity formula involving variables proposed by Reynolds and a new model equation for dissipation ε based on the dynamic equation of the mean-square vorticity fluctuation. Hence, the k-equation is same as in standard $k-\varepsilon$ and RNG $k-\varepsilon$ model but the ε-equation is quite different than that of the other two. The noteworthy feature is that the production term in the ε-equation does not involve the production of k presenting the spectral energy transfer in a better way.

This model was validated extensively for wide range of flows including free flows including jets and mixing layers, rotating homogeneous shear flows, separated and boundary layer flows and channel flows. Another fact is that this model resolves the round-jet anomaly, i.e., it predicts the spreading rate for axisymmetric jets as well as that for planar jets.

Fig. 4.7 shows the resulting heat transfer distribution caused by the impinging jet. A closer observation reveals that the $y^+ \approx 1$ satisfy the empirical correlation better than results of any other y^+ value plots. At $y^+ \approx$ 4, the numerical data seems to satisfy the empirical range, but not at the stagnation region. Moreover, at lower y^+, viscous sub-layers can be resolved more accurately. Hence, the plot with $y^+ \approx 2$ is chosen as more appropriate result in this turbulence model.

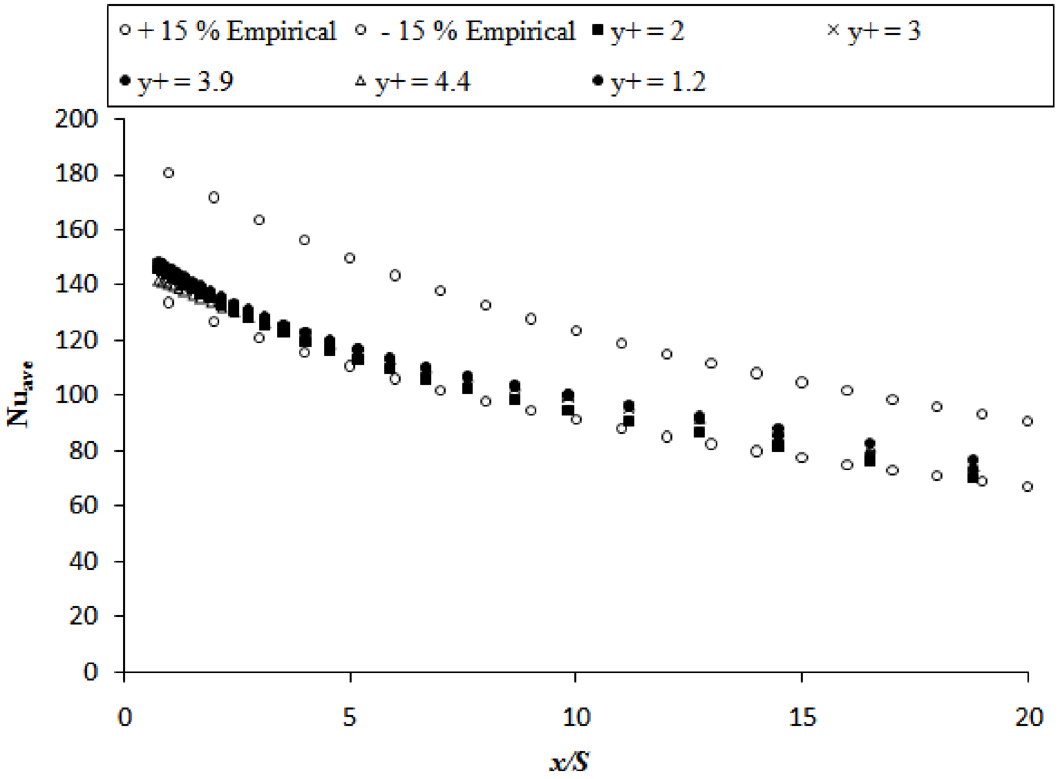

Figure 4.8 Comparison of empirical with numerical Nusselt number distribution at various y^+ using Realizable *k*-*ε* tubulence model

4.2.1.5 The Standard *k*-*ω* Model

The Standard *k*-*ω* model [51] is an empirical model based on model transport equations for the turbulence kinetic energy (k) and the specific dissipation rate (ω). Standard $k-\omega$ model has been improved over the years to effectively predict the free shear flows. Moreover, at the wall boundary condition for the k equation in $k-\omega$ model is treated in a similar way as that for k equation in $k-\varepsilon$ model for enhanced wall treatments wall function approach. This makes $k-\omega$ model calculate identically to $k-\varepsilon$ model except in the specific dissipation rate.

It was observed in the local nusselt number plot that the stagnation region yields an abnormal heat transfer rate when compared to the values obtained from any $k-\varepsilon$ models. Results obtained from the use of Standard $k-\omega$ model show (Fig. 4.8) that the stagnation region yields a normal heat transfer rate when compared to the values obtained from any $k-\varepsilon$ models except for the wall-jet region. The Standard $k-\omega$ plot is almost similar to the $k-\varepsilon$ models in the wall-jet region where the value of k has been calculated in a similar way to that of k in other $k-\varepsilon$ models.

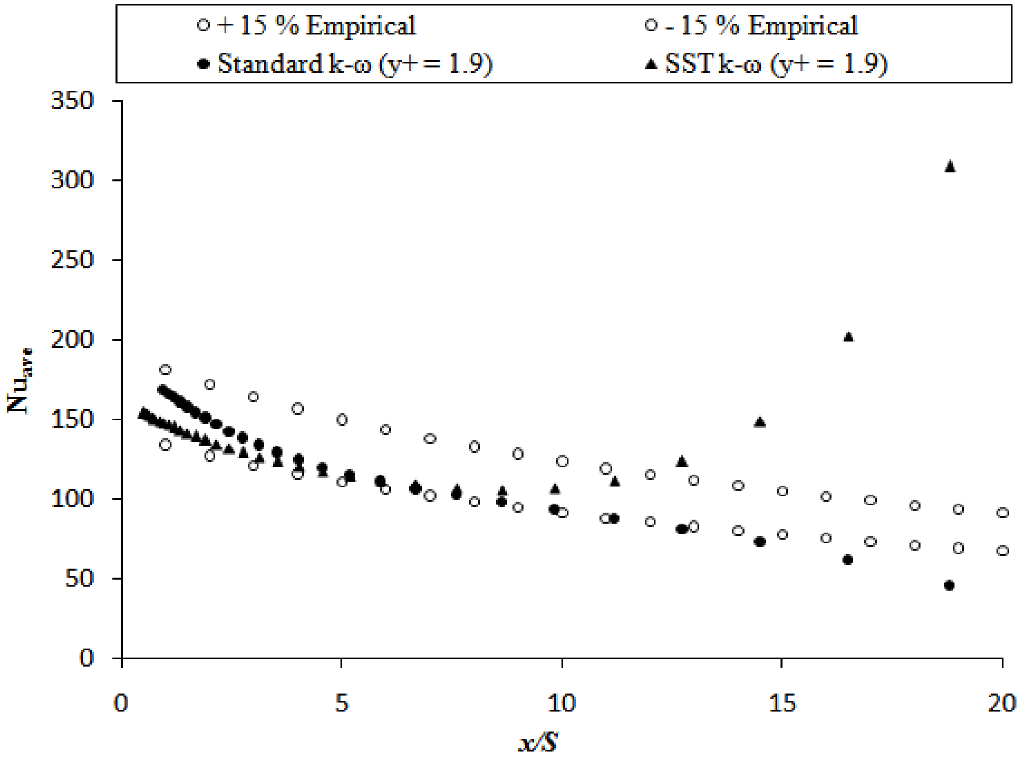

Figure 4.9 Comparison of empirical with numerical Nusselt number distribution at various y^+ using Standard *k-ω* tubulence model

4.2.1.6 The Shear-Stress Transport (SST) *k*-*ω* Model

The SST model [51] differs from the standard $k-\omega$ model in two ways, namely; in the gradual change from the standard $k-\omega$ model to a high-Reynolds-number version of the $k-\varepsilon$ model in the outer part of the boundary layer and, SST model has modified turbulent viscosity formulation to account for the transport effects of the principal turbulent shear stress. This might be the main cause for lower values of heat transfer at the stagnation region (Fig. 4.8) for SST model than for standard $k-\omega$ model because of which unstable results were also seen.

4.3 Validation

A thorough analysis of the results obtained from section 4.2 revealed two turbulence models producing results close to the empirical correlation (Eq. 4.2). The RNG *k*-*ε* and the Realizable *k*-*ε* turbulence model produced good agreement at $y^+ \approx 1$. The effect of y^+ on the surface heat transfer was visible more clearly in realizable *k*-*ε* model than in RNG *k*-*ε* model (see Fig. 4.10). However, a strong reason to select realizable *k*-*ε* model for current parametric study is usage of a new model equation for dissipation (*ε*) based on dynamic equation of mean-square vorticity fluctuation and a new eddy viscosity formula. Moreover, realizable *k*-*ε* model has been widely and extensively validated for problems pertaining to free flow jets and is suitable to predict the spreading rate for axisymmetric jets as well as planar jets.

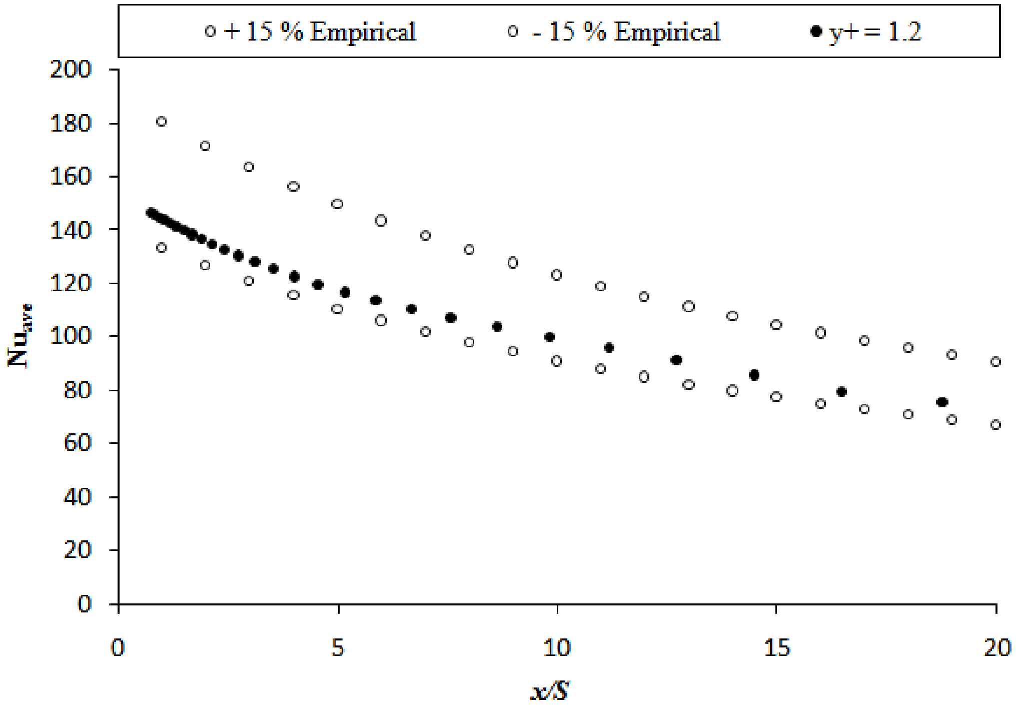

Figure 4.10 Comparison of empirical with numerical Nusselt number distribution at various $y^+ = 1$ using Realizable k-ε tubulence model

Hence, realizable k-ε turbulence model will be used for all the models and parametric cases in this study.

4.4 Models and Cases

As proposed in the objectives, six models are studied in an attempt to increase the heat transfer distribution at the wall-jet region past the stagnation region. Consequently, innovative models were designed with a support from the literature for a detailed parametric investigation. The models were broadly categorized into three types: jet-flow turbulence enhancers, surface liners and surface flow turbulence enhancers. These models are as follows:

(a) Jet-Flow turbulence enhancers

    i) Triangles

    ii) Cylinder

    iii) Wedge

(b) Surface liners

    i) Channel

(c) Wall-flow turbulence enhancers

    i) Vortex generators (VG)

    ii) Cavities

The details of all the above models and their configurations are given in Table. 4.2.

Table 4.1 Detailed configurations of all models

Model	Triangle		Cylinder		Wedge		Channel			Vortex generator		Cavity		
Variables	**Height h_t**	**Inter-obstacle distance d_t**	**Height h_{cyl}**	**Radius r_{cyl}**	**Height h_w**	**Vertical angle θ**	**Distance from jet centerline d_c**	**length l_{ch}**	**Height h_{ch}**	**Height h_{vg}**	**Angle ϕ**	**Width l_c**	**Distance d_c**	**Radius r_c**
Variable values	0.0125	0.004	0.00938	0.00938	0.0125	20	0.1	0.4	0.013	0.0015	26.5	0.04	0.04	0.05
	0.0188	0.005	0.0125	0.0125	0.0188	30	0.15	0.45	0.014	0.001	45	0.05	0.05	0.06
	0.025	0.006	0.01563	0.01563	0.025	40	0.2	0.5	0.015	0.0005	63.4	0.06	0.06	0.07
						50			0.016		84.3			
									0.017		100			
											120			
											140			
No. of cases studied	9		9		12		5			9		9		
Variable combinations used in each case	0.0125	0.004	0.00938	0.00938	0.0125	20	0.1	0.6	0.013	0.0015	26.5	0.06	0.04	0.05
	0.0188	0.004	0.0125	0.00938	0.0188	20	0.1	0.6	0.014	0.0015	45	0.05	0.05	0.05
	0.025	0.004	0.01563	0.00938	0.025	20	0.1	0.6	0.015	0.0015	63.4	0.04	0.06	0.05
	0.0125	0.005	0.00938	0.0125	0.0125	30	0.1	0.6	0.016	0.0015	84.3	0.06	0.04	0.06
	0.0188	0.005	0.0125	0.0125	0.0188	30	0.1	0.6	0.017	0.0015	100	0.05	0.05	0.06
	0.025	0.005	0.01563	0.0125	0.025	30				0.001	120	0.04	0.06	0.06
	0.0125	0.006	0.00938	0.01563	0.0125	40				0.001	140	0.06	0.04	0.07
	0.0188	0.006	0.0125	0.01563	0.0188	40				0.0005	120	0.05	0.05	0.07
	0.025	0.006	0.01563	0.01563	0.025	40				0.0005	140	0.04	0.06	0.07
					0.0125	50								
					0.0188	50								
					0.025	50								

4.4.1 Triangles Model

Saeed et al. [52] attempted to enhance the jet impingement heat transfer using obstructions creating turbulence. They obstructed the jet with a mesh in the stagnation region at a particular height from the impinging surface. They found significant enhancement in turbulence due to the obstructions. Kurima et al. [22] used a perforated plate and succeeded in enhancing the heat transfer by 2.3 times. Lee et al.[15] also used a perforated plate between the jet and the impinging surface. They found that as the perforated-to-impinging plate distance decreased, more active interaction among the jets rapidly increased the rate of the heat transfer. They found about 2 times higher average Nusselt number with perforated plate than for without perforated plate.

In the present study, a series of equivalent triangles are used to enhance the turbulence in the flow. The numerical domain for the triangles model is shown in the Fig. 4.11 (a) while the geometric parameters used for this model are shown in Fig. 4.11 (b).

Table 4.2 Parametric values used for triangles model.

Parameter	Dimension in R	Dimension in m
Δt	$0.5R$	0.00625
d_{t1}	NA	0.004
d_{t2}	NA	0.005
d_{t3}	NA	0.006
h_{t1}	$1\ R$	0.0125
h_{t2}	$1.5\ R$	0.01875
h_{t3}	$2\ R$	0.025

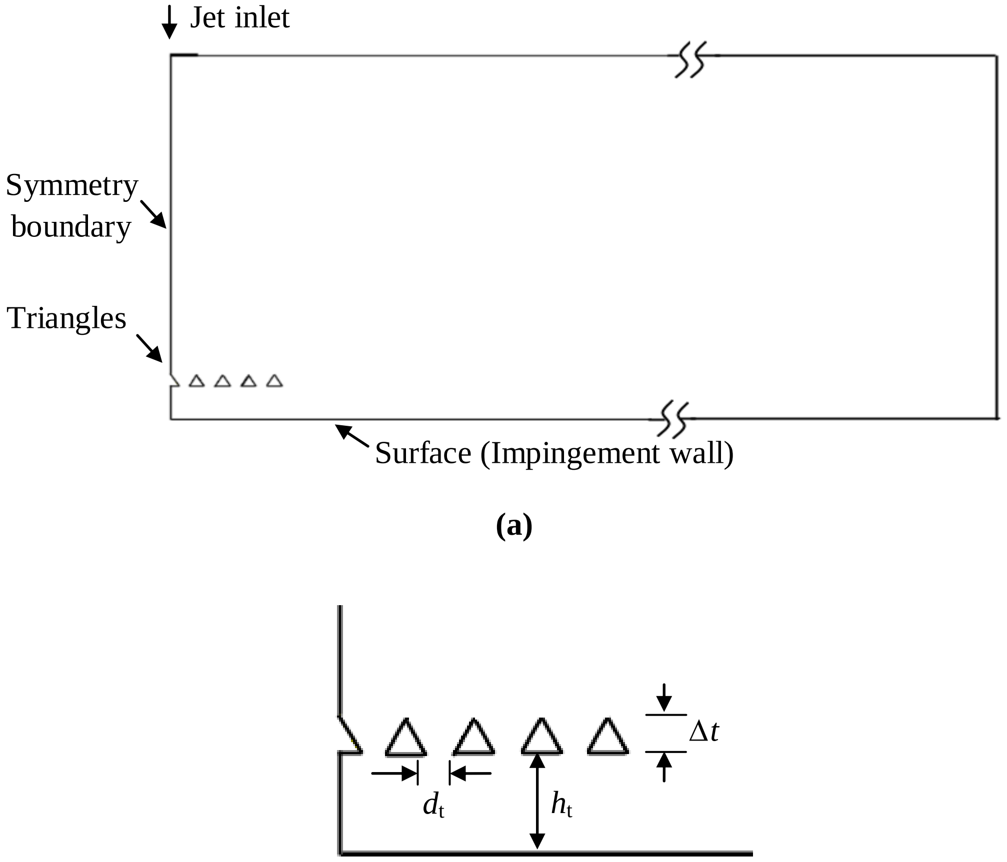

(a)

(b)

Figure 4.11 Schematic view of the triangles model (a) Entire domain (b) Close-up view and parameter definition.

All the combinations of d_{t1}, d_{t2} and d_{t3} with h_{t1}, h_{t2} and h_{t3} were investigated. The results are explained and discussed in chapter 5.

A fully structured grid was constructed for this model. A high resolution grid is needed not only at the impingement wall region but also around the triangular surfaces. A closer view of the computational grid is shown in Fig. 4.12. Different grid adaptation schemes based on y^+, velocity gradient, first cell boundary were used interactively to resolve various flow features.

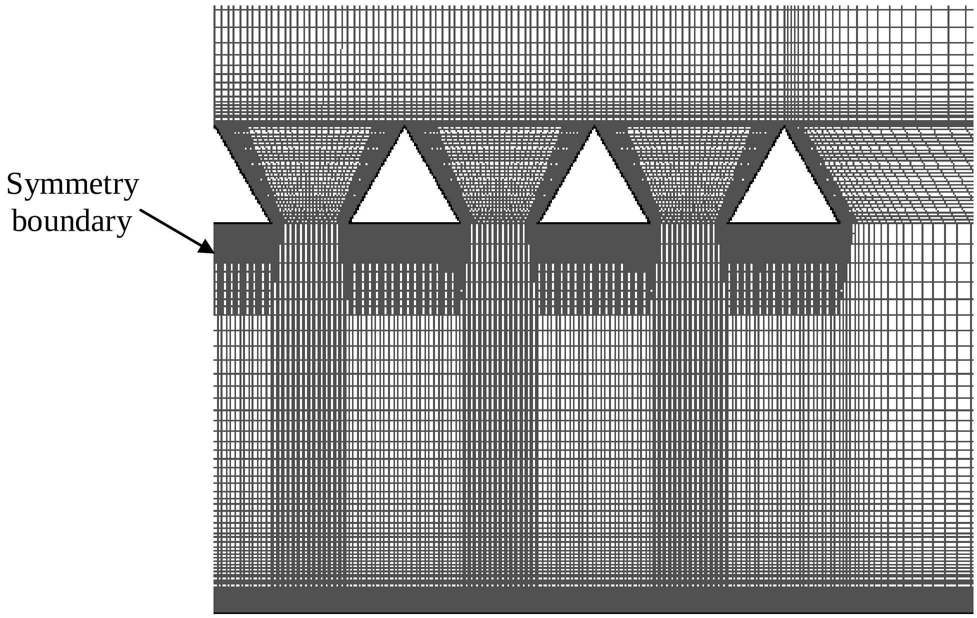

Figure 4.12 Varying grid resolutions above the stagnation region and around the triangles

4.4.2 Cylinder Model

This model focuses on the appropriate diameter and distance of a cylinder from the impinging surface as shown in Fig. 4.13 (a) to maximize the heat transfer distribution. Due to the symmetric nature of domain being studied, the cylinder can be observed as a semi-circle at the symmetry boundary of the domain. Inserting a cylinder in the jet flow is not a new investigation performed to enhance the heat transfer rate. Haneda et al. [16] introduced a rigidly suspended cylinder and augmented heat transfer rate to about 40% at a nozzle-to-target plate distance of 3. However, their investigation also involved oscillatory motion of the cylinder and with less parametric study. Oscillation was also applied by Camci [33] but his investigation was concerned with jet oscillation. He improved heat transfer rate from 20% to 70%.

In the present study, a semi-circle was used to study the flow structure in the given domain and how it enhances the turbulence in the flow. The numerical domain for the cylinder model is shown in the Fig. 4.13 (a) while the geometric parameters used for this model are shown in Fig. 4.13 (b).

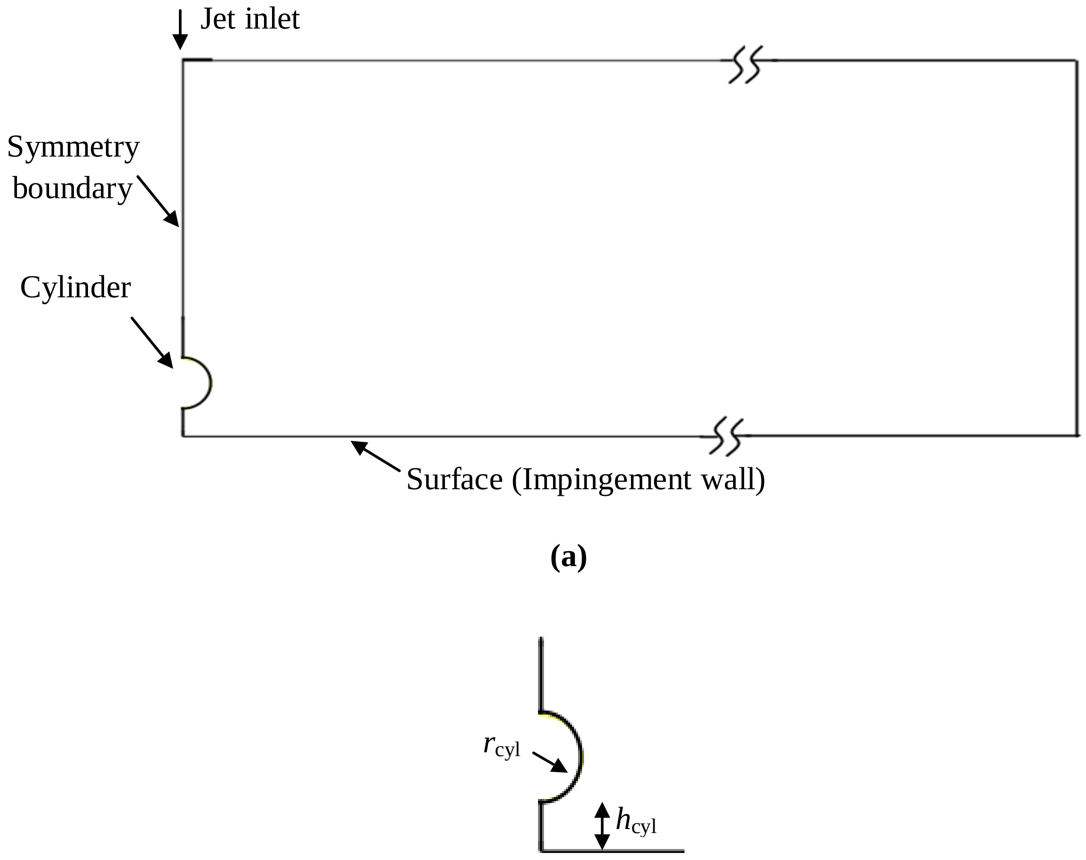

(a)

(b)

Figure 4.13 Schematic view of the cylinder model (a) Entire domain (b) Close-up view and parameter definition.

A half cylinder in the form of a semi- circle was placed at the symmetry end of domain and at a height h_{cyl} above the stagnation region of the impinging jet (Fig. 4.13). The radius of the semi-circle R is expressed in terms of jet slot radius R (Fig. 4.13). Jet slot radius is taken as reference length for all the parameter dimension in this models. Hence, the different values of r_{cyl} and h_{cyl} used in this study are defined in terms of jet radius R and are listed in Table 4.4.

Table 4.3 Parametric values used for the cylinder model

Parameter	Dimension in *R*	Dimension in m
r_{cyl1}	0.75 R	0.009375
r_{cyl2}	1 R	0.0125
r_{cyl3}	1.25 R	0.015625
h_{cyl1}	0.75 R	0.009375
h_{cyl2}	1 R	0.0125
h_{cyl3}	1.25 R	0.015625

Different combinations of r_{cyl1}, r_{cyl2} and r_{cyl3} with h_{cyl1}, h_{cyl2} and h_{cyl3} resulted in nine (9) cases to be investigated. These 9 parameters were valued based on the results obtained from Haneda et al. [16]. They used $H/2R$ = 3 and 5, and the in the present study we used 8 which is a standard value in the anti-icing system. Corresponding to this value, they fixed h_{cyl} = 8 mm varying H, and the same parameter was varied at h_{cyl} = 9, 12 and 15 mm in the present study with a constant H = 0.2 m. The results are explained and discussed in chapter 5.

A hybrid grid was constructed for this model. A high resolution of grid is need at not only the impinging wall region but also near the circular surfaces. A closer view of the computational grid is shown in Fig. 4.14.

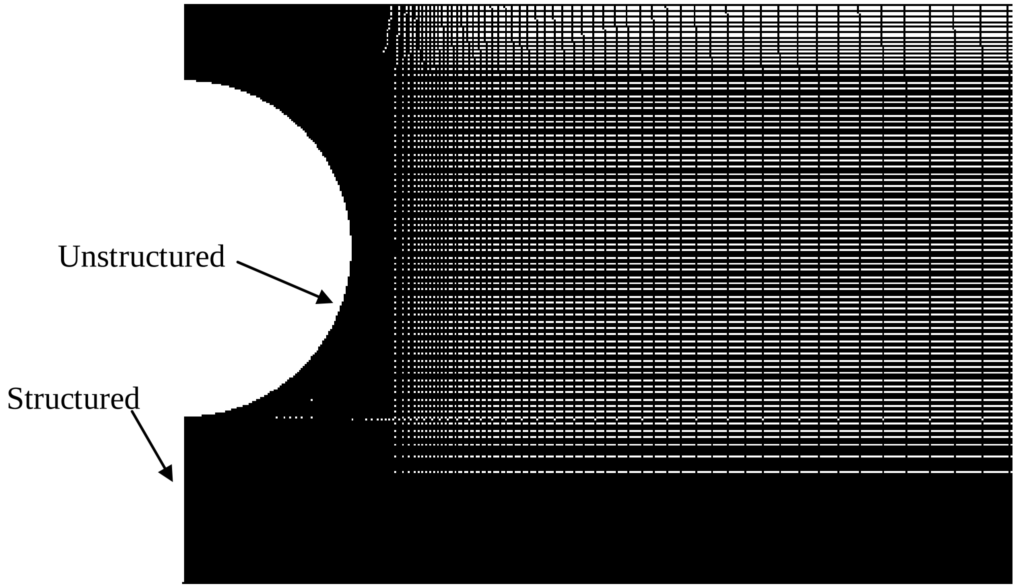

Figure 4.14 Close-up view of hybrid grid used for the cylinder model

4.4.3 Wedge Model

We all know that an obstruction in the jet-flow deflects the jet according to its profile. When a wedge is placed in front of the jet, then the jet is deflected parallel to the wedge surface. Placing a wedge at some height from the stagnation region allows the jet to impinge over a greater area around the stagnation region. One such investigation was done by Saeed et al. [52]. In the present model, a right-angled wedge with a rounded corner which can be viewed as a triangle in a two dimensional space is placed between the jet and the impingement wall as shown in the Fig. 4.15. When the jet is attached to the wedge on its inclined surface, the lower corner of the body plays an important role in producing turbulence in the flow before it impinges on the surface. This phenomenon is very similar in vortex generators where the flow is slowly diverted to an angle and then suddenly the shear stresses within the fluid create vortices. In our case, the rounded corner of the wedge draws the flow towards the region below the wedge. Unlike the case of Saeed et al. [52], the rounded corner of the wedge creates lesser turbulence but allows the flow to affect the stagnation region under the obstacle.

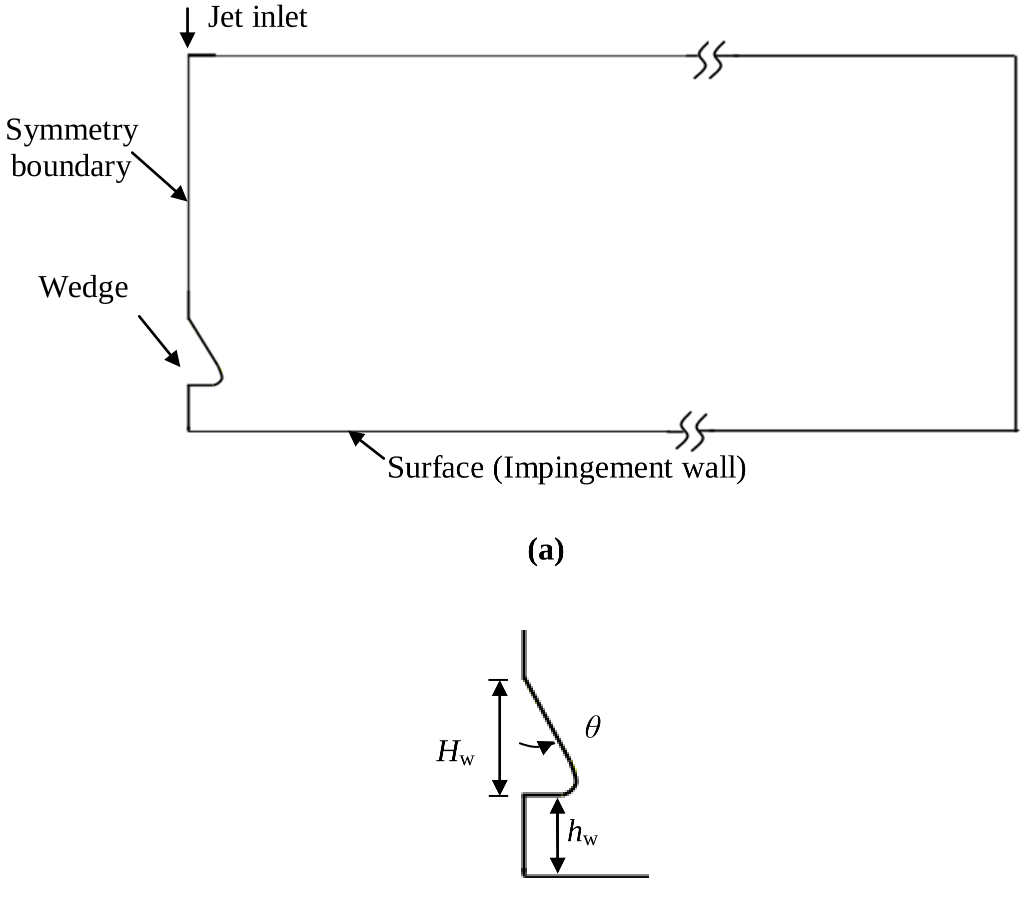

(a)

(b)

Figure 4.15 Schematic view of the wedge model (a) Entire domain (b) Close-up view and parameter definition.

One parameter in Fig. 4.15 was fixed in order to limit the number of cases to be run in the investigation. The height of the wedge H_w was kept constant at $3R$ which is 0.0375 m. Other parameters were varied as shown in Table 4.5.

Table 4.4 Parametric values used for the wedge model

Parameters	**Dimensions in R**	**Dimensions in m/degree**
H_w	3r	0.0375
θ_1	NA	20
θ_2	NA	30
θ_3	NA	40
θ_4	NA	50
h_{w1}	$1R$	0.0125
h_{w2}	$1.5R$	0.01875
h_{w3}	$2R$	0.025

Twelve combinations of the above parameters were investigated and detailed analyses of results are explained in chapter 5.

A structured grid was constructed for the wedge model. A high resolution of grid is needed not only at the impinging wall region but also near the wedge surfaces. A closer view of the computational grid is shown in Fig. 4.16.

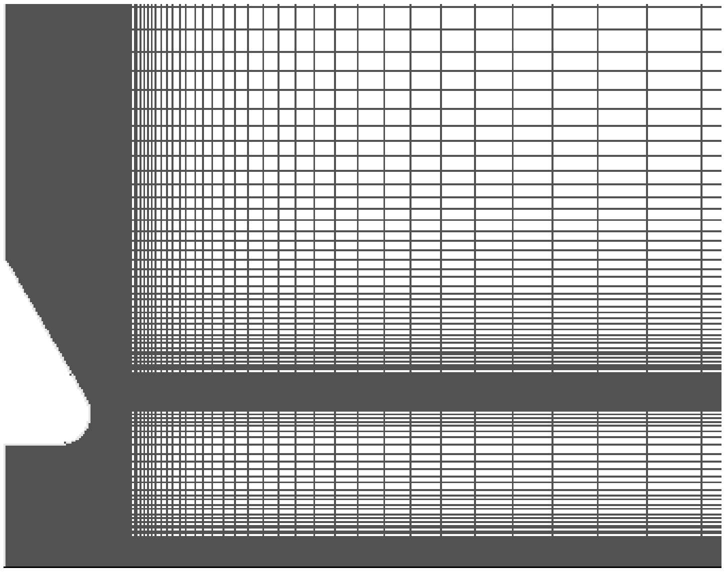

Figure 4.16 Close-up view of structured grid for the wedge model

4.4.4 Channel Model

It is a known fact that confined flow restricts the dissipation within the channel and forces additional heat flux. Saeed et al. [52] investigated this phenomenon and showed increased heat transfer rate due to the confined region past the stagnation point. In the present study, a channel was used to confine the wall-jet flow. Unlike the model used by Saeed et al. [52], the present does not extend all along the impingement wall but is of specific length. In the investigation of Saeed et al. [52], the edge starts near the stagnation region and confines the wall-jet flow till the exit. In the present study, this confinement was released and an optimum channel length was investigated. The only difference in the present investigation and that of Saeed et al. [52] is at they used an exit area equal to the area under the channel, whereas the exit area in the present study is the entire exit boundary as shown in Fig. 4.17.

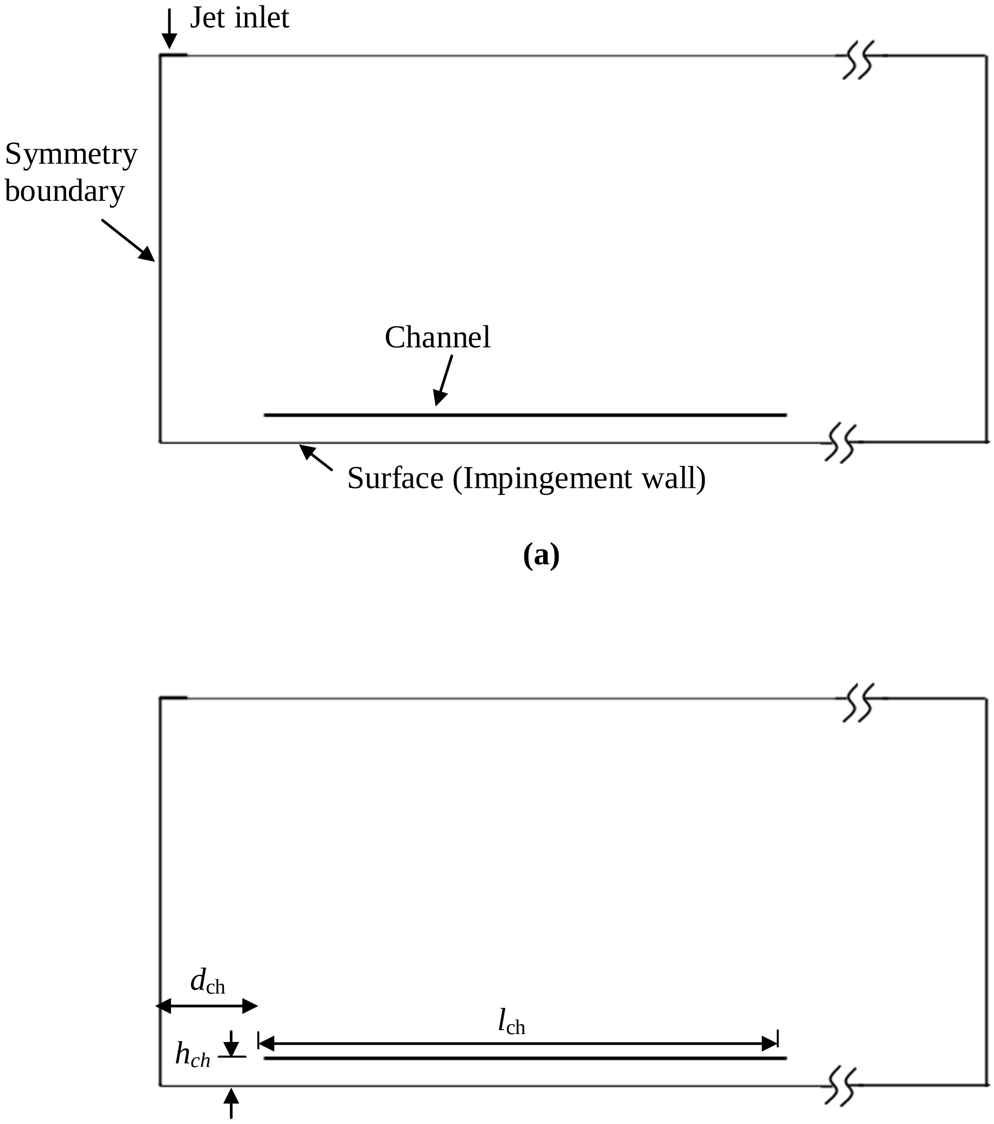

(a)

(b)

Figure 4.17 Schematic view of the channel model (a) Entire domain (b) Close-up view and parameter definition.

The investigation was carried in two parts: In the first part, a suitable length of the channel l_{ch} and the shortest channel-to-jet centerline distance d_{ch} was investigated. In order to achieve this, the velocity contour of the jet without any obstruction was closely observed. After the stagnation region, the flow is free to move towards the domain extremes. It is noteworthy that immediately after the impingement; the surface flow boundary expands first and then dissipates. The point at which the flow starts to expand (as shown in the Fig. 4.18) was considered as the minimum height of the channel. This consideration was taken in order to retain maximum fluid flow under the channel. It should be noted that in this study unlike in the work of Saeed et al. [52], the confinement does not start from jet inlet. Hence, an effort should be made to keep the flow as much as within the channel after the impingement. The channel-to-jet centerline distance d_{ch} was sensitively valued so that the channel does not interfere with the jet itself.

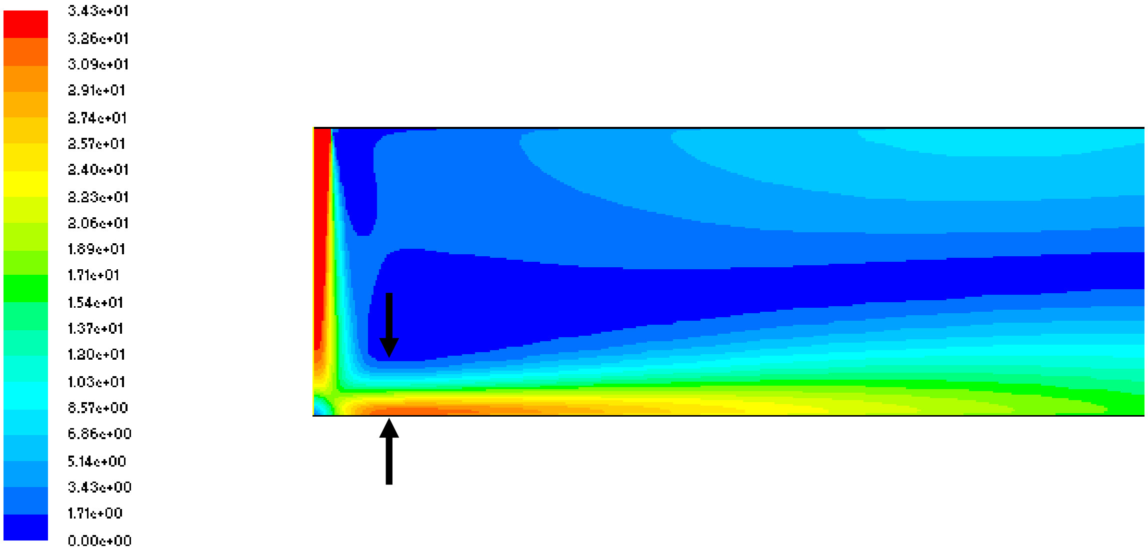

Figure 4.18 Velocity contour for jet impingement without obstruction with arrows pointing the region with the least wall-jet flow thickness.

The velocity contour from the validation section was taken and three values of d_{ch} were chosen as 0.1, 0.15 and 0.2 m. In the present study, maximum channel length was to be obtained; hence lower channel lengths were not encouraged. The length of the channel was gradually increased at l_{ch} = 0.4, 0.45 and 0.5 m. For minor adjustments, the value of

h_{ch} was varied by 0.0125 and 0.015 m to obtain accurate and maximum length of the channel which can hold the flow under it.

In the second part of the investigation, the optimal position of the channel start and end was found to be from d_{ch} = 0.01 m and d_{ch} = 0.6 m respectively. After finding an appropriate location of channel above the horizontal axis, the second part was initiated in which, an investigation on optimum height of the channel was conducted. h_{ch} was varied as h_{ch} = 0.013, 0.014, 0.015, 0.016 and 0.017 m.

A structured grid was constructed using fine resolution at the impinging wall and channel as shown in Fig. 4.19.

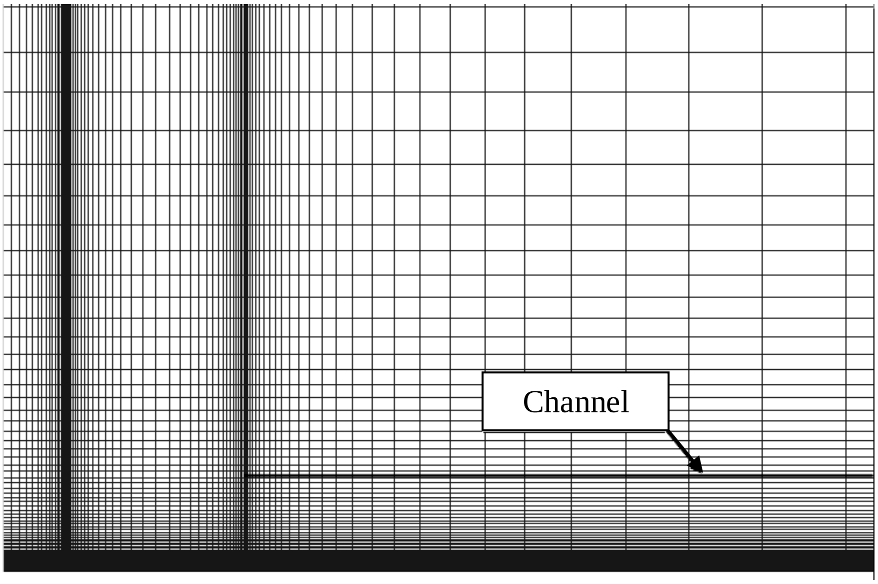

Figure 4.19 Close-up view of structured grid for the channel model

4.4.5 Vortex Generators Model

Recent investigations using vortex generators (VG) were carried out by Mokrani et al. [45] and Chang et al. [46]. Mokrani et al [45] used trapezoidal vortex generators at 30^o

angle to the inner wall of a tube. Their main aim was to enhance mixing of chemicals with the fluid flow inside the tube. They succeeded in enhancing the turbulence intensity up to 17%.

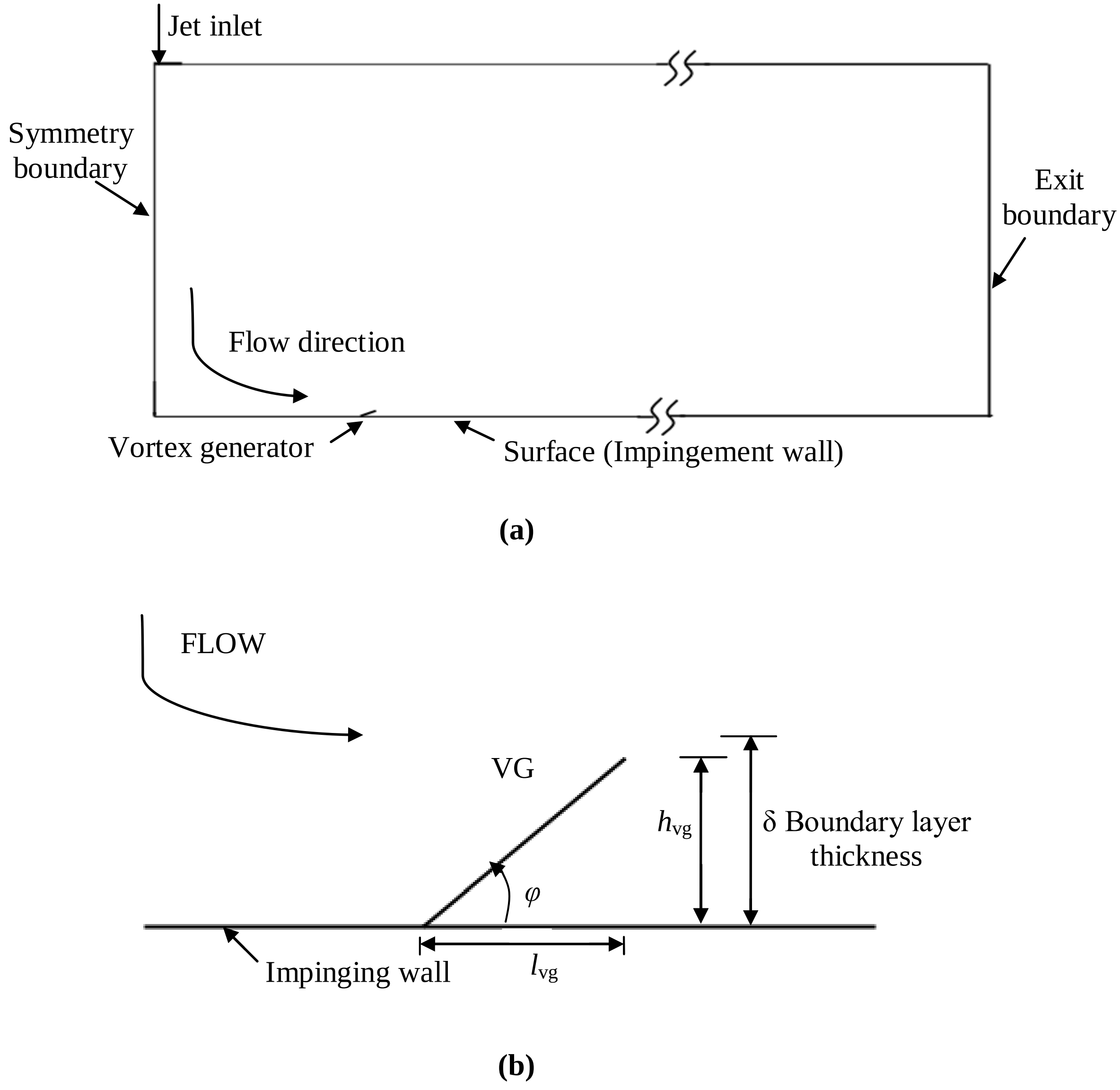

Figure 4.20 Schematic view of the channel model (a) Entire domain (b) Close-up view and parameter definition.

Their results conform to the fact that the turbulence intensity is a main cause to enhance the heat transfer as stated by Herbert et al. [35]. Chang et al. [41] used vortex generators at an angle of 35° to specify secondary flow using cross averaged absolute vorticity flux. Other investigations such as Korichi et al. [44] were also conducted but they used both surface obstructions and vortex generators in a channel flow. Implementation of vortex generators alone has never been used in jet impingement aiming to enhance the heat transfer distribution.

As in the case of channel modeling, the vortex generator model investigation was also divided into two parts.

1. Finding suitable angle for the VG according to the flow
2. Appropriate placement of VG on the impinging wall.

Literature suggests that the height of the vortex generators should be within the boundary layer in order to effectively enhance the heat transfer. Hence, the height of the vortex generators was varied well within the boundary layer thickness. The main parameter investigated in the first phase of the modeling was the angle φ of the VG. It is well supported by the literature that in a conventional VG, the length of VG is double its height [42]. Hence, the design of the VG was proposed as shown in the Fig. 4.20 (b).

The VG is represented by a right-angled triangle on to the impinging wall. Using the relation $h_{vg} = l_{vg}\tan\varphi$, three values of h_{vg} and corresponding l_{vg} were used to obtain appropriate value of φ. h_{vg} was varied at 0.0015, 0.001 and 0.0005 m according to the results obtained in trials to find the optimum channel height. Table 4.6 list the parameters used to investigate the effect of VG angle.

Table 4.5 Parameters used to investigate the effect of VG angle.

VG Name	Height of VG h_{vg}	l_{vg} in terms of h_{vg}	Angle of VG φ in degree
$\varphi_1 y_1$	y_1	$2\ y_1$	26.5
$\varphi_2 y_1$	y_1	y_1	45
$\varphi_3 y_1$	y_1	$0.5\ y_1$	63.4
$\varphi_4 y_1$	y_1	$0.1\ y_1$	84.3
$\varphi_5 y_1$	y_1	$0.18\ y_1$	100
$\varphi_6 y_1$	y_1	$0.57\ y_1$	120
$\varphi_7 y_1$	y_1	$1.2\ y_1$	140
$\varphi_3 y_2$	y_2	$0.5\ y_1$	63.4
$\varphi_6 y_2$	y_2	$0.57\ y_1$	120
$\varphi_7 y_2$	y_2	$1.2\ y_1$	140
$\varphi_6 y_3$	y_3	$0.57\ y_1$	120
$\varphi_7 y_3$	y_3	$1.2\ y_1$	140

In the second part, VGs were placed at fixed intervals along the impingement wall. The location was decided only after the result in part one of modeling were analyzed. The final design of VGs were placed and analyzed one by one at a distance of 0.2, 0.35, 0.5 and 0.65 from the jet centerline. Fig. 4.21 shows the structured grid modeled with gradual grid densities and fine mesh arrangement.

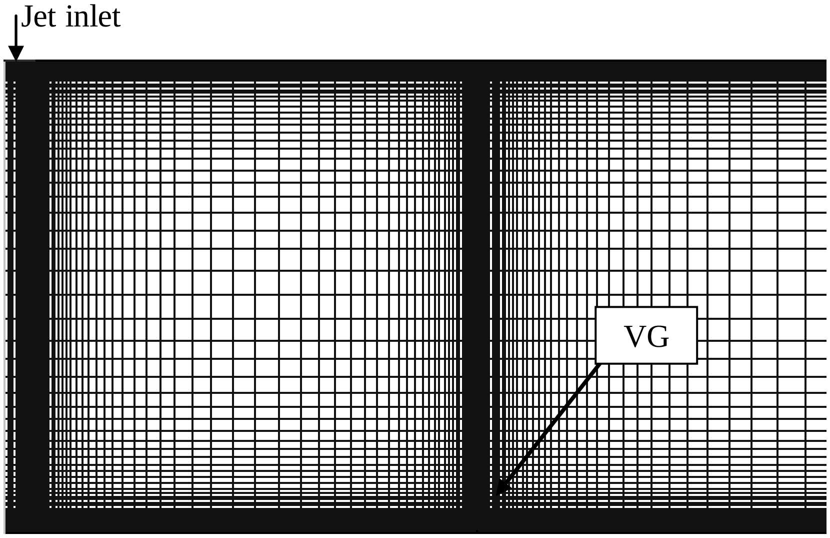

Figure 4.21 Structured grid for the VG model

4.4.6 Cavity Model

A recent development in the surface modification to enhance heat transfer is a dimpled surface. Srinath et al. [34] used jets of 0.006 m diameter jets with Reynolds number varying from 4800 to 14800 and dimple depth of 0.003 m and 0.0015 m. In their study they used one dimple for one jet which implies they only studied one cavity per jet method in pattern form. Park et al. [42] found that vortex pairs in the recirculation region enhanced the thermal performance better in circular dimples than in oval dimples, but their study was for a very low Reynolds number. Kanokjaruvijit et al. [38] studied similar array of jets on dimples with diameter 0.0017 m and jet-to- dimple diameter ratio of 0.59. They found 8 to 68% heat transfer augmentation at *H/D* ratio of 8. However they suggested more parameters like ratio of jet-diameter to dimple-diameter, dimple-depth and pitch need to be investigated. A model extending the work of Kanokjaruvijit [38] could have been made, but due to modeling difficulties, a better and clear model with parameters suggested by Kanokjaruvijit [38] were studied. Thus, optimum cavity-diameter, cavity-spacing and cavity-width are investigated in this study considering the remarks found in the literature.

In the present study, eight cavities in a span of 1 m divided by a parametric length were studied. Three values of distance between the dimple spacing at three values of dimple depth were investigated. A schematic diagram of the model is shown in Fig. 4.22.

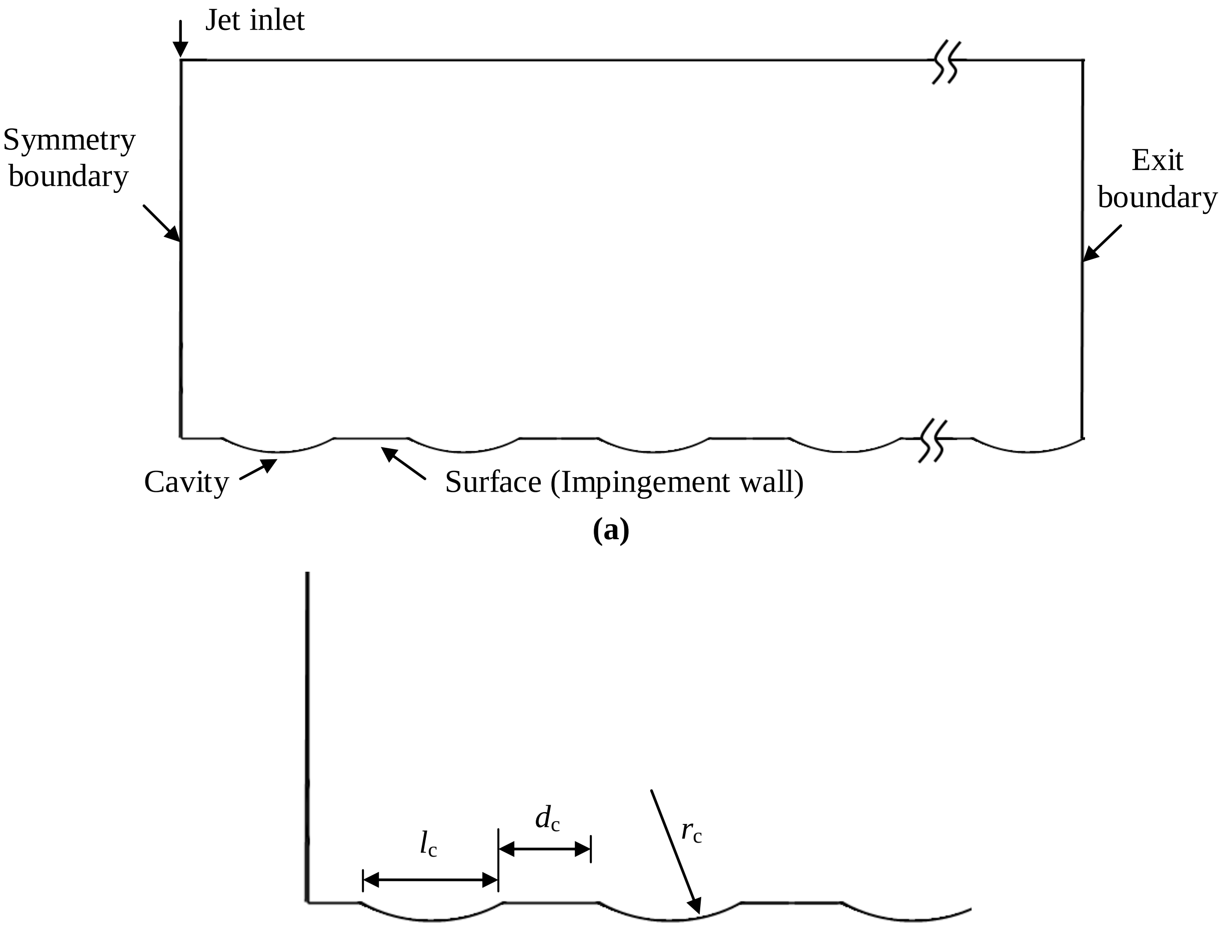

(a)

(b)

Figure 4.22 Schematic view of the cavity model (a) Entire domain (b) Close-up view and parameter definition.

Table 4.6 Parametric used to investigate cavity model

Case	Cavity spacing d_c	Cavity width l_c	Cavity radius r_c
Case 1	0.04	0.06	0.05
Case 2	0.05	0.05	0.06
Case 3	0.06	0.04	0.07

The parametric changes were divided into three cases as shown in the Table 4.7. Each case has its own value of cavity spacing, cavity depth, cavity width and cavity radius. The cavity depth similar to that of Kanokjaruvijit [38] varies with cavity radius in each case. Table 4.8 shows the cavity depth for each radius in each case.

Table 4.7 Parameter combinations and corresponding cavity depth

Case	Radius	Cavity depth
Case 1	r_{c1}	0.01
	r_{c2}	0.008
	r_{c3}	0.00675
Case 2	r_{c1}	0.0067
	r_{c2}	0.00545
	r_{c3}	0.0046
Case 3	r_{c1}	0.00417
	r_{c2}	0.00343
	r_{c3}	0.00292

A structured grid was constructed for this model with grid refinement near the impingement and cavity as shown in the Fig. 4.23.

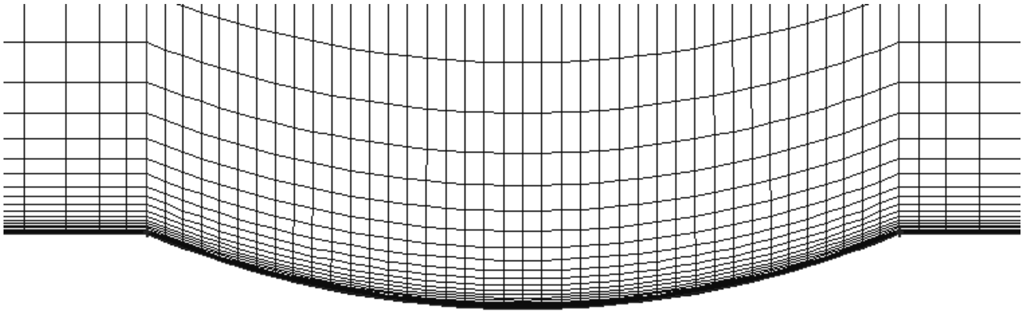

Figure 4.23 Close-up view of structured grid for cavity model

CHAPTER 5

RESULTS AND DISCUSSION

Heat transfer augmentation on a surface using 2D hot-air jet impingement technique was investigated using various models. Numerical results were satisfactorily validated against empirical correlation given by Martin [6]. Various obstructions were modeled and analyzed with a view of enhancing heat transfer distribution over the target surface. Triangles, cylinder, wedge, channel, vortex generators and cavity models were categorized into jet-flow obstructions, surface liners and wall-flow obstructions to simplify and analyze the simulations. Heat transfer was measured using Nusselt number on the target surface. A thorough analysis for parametric values was done in each model to obtain suitable dimensions for enhanced heat transfer distribution. Analysis for each model is explained and important observations are illustrated in the following sections.

5.1 Triangles Model

Numerical simulation of a triangles model as shown in Fig. 4.11 (a) was investigated with parametric variations as listed in Table 4.2. The resulting nine parametric combinations, listed in Table 5.1, were studied using FLUENT. Convergence criteria of 10^{-6} was chosen for the residuals of continuity, energy, k, epsilon, x and y velocities. Each case took an average time of 4 days to converge on a 3 GHz processor personal computer with 2GB RAM running Windows XP operating system.

The reference values used for post processing for all the models and cases are as shown in Table 5.2. The results obtained are presented in the next section.

Table 5.1 Parametric combination investigated in triangles model

Case ID	**Obstacle height (m)**	**Obstacle spacing (m)**	**Associated Results**
A1	0.0125	0.004	Fig. 5.1
A2	0.01875	0.004	Fig. 5.1
A3	0.025	0.004	Fig. 5.1
A4	0.0125	0.005	Fig. 5.2
A5	0.01875	0.005	Fig. 5.2
A6	0.025	0.005	Fig. 5.2
A7	0.0125	0.006	Fig. 5.3
A8	0.01875	0.006	Fig. 5.3
A9	0.025	0.006	Fig. 5.3

Table 5.2 Reference values used for post processing

Property (units)	Value
Area (m^2)	1
Density (kg/m^3)	0.887502
Depth (m)	0.025
Enthalpy (j/kg)	102885.3
Length (m)	0.025
Pressure (pascal)	0
Temperature (K)	400
Velocity (m/s)	33.959 m/s
Viscosity (kg/m-s)	2.225375×10^{-5}
Ration of specific heat	1.4

5.1.1 Effect of Triangle Height at Constant Obstacle Spacing d_{t1}

Fig. 15.1 shows the plot of Nusselt number distributions along the impinging wall for different obstacle-to-target plate height at constant obstacle spacing of 0.004 m.

A general character is observed which shows higher heat transfer at the stagnation region and comparatively lower heat transfer along the wall-jet region which almost gradually meets the flat plate values.

At an obstacle height equal to jet radius, it is observed that the overall heat transfer is much less than the heat transfer without any obstruction. Moreover, on comparing the plot with those of increase obstacle height of 1.5R and 2R, a clear difference along the whole length is observed. This indicates that $h_{t1} = R = 0.0125$m could be the lowest value for this case and can be avoided in future study. Also, there is a gradual decrease in the difference as h_t changes from R to $2R$.

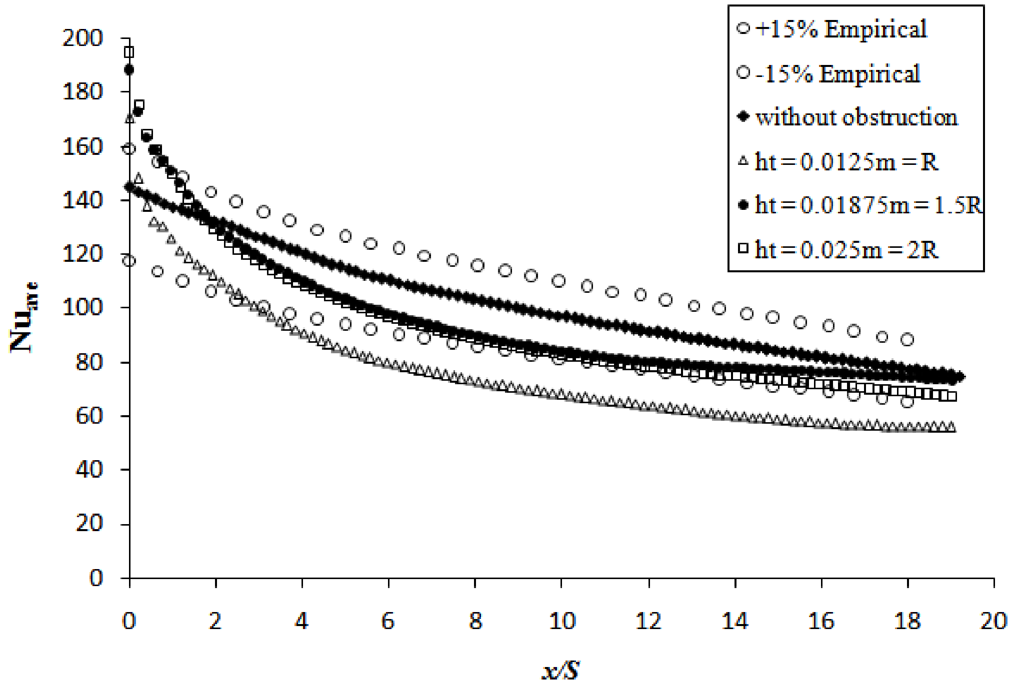

Figure 5.1 Comparison of Nusselt number distribution for various obstacle heights at constant obstacle spacing of 0.004 m.

At $h_{t2} = 1.5R$, a small increase in the average Nusselt number value in far wall-jet region is observed relative to other plots.

5.1.2 Effect of Triangle Height at Constant Obstacle Spacing d_{t2}

Fig. 5.2 shows the plot of Nusselt number distributions along the impinging wall for different obstacle-to-target plate height at constant obstacle spacing of 0.005 m.

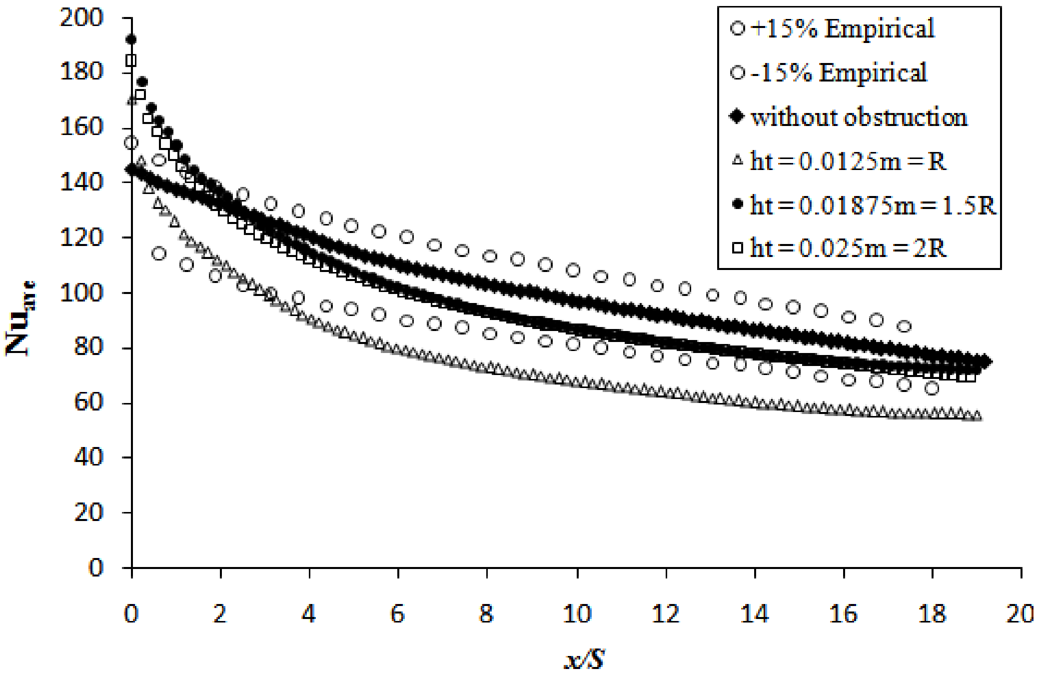

Figure 5.2 Comparison of Nusselt number distribution for various obstacle heights at constant obstacle spacing of 0.005 m.

A character is observed again which shows higher heat transfer at the stagnation region and comparitively lower heat transfer along the wall-jet region which almost gradually meets the flat plate values. Also a clear difference along the whole length is observed between the plot of h_{t1} = 0.0125 m = R (case A4) and other plots indicating the limit for triangles height from the impinging surface.

An increase in obstacle height h_t to 0.01875 m (1.5R) and 0.025 m (2R) results in almost the same Nu distribution except near the stagnation region where h_{t2} = 1.5R gives better enhancement.

5.1.3 Effect of Triangle Height at Constant Obstacle Spacing d_{t3}

Fig. 5.3 shows the plot of Nusselt number distributions along the impinging wall for different obstacle-to-target plate height at constant obstacle spacing of 0.006 m.

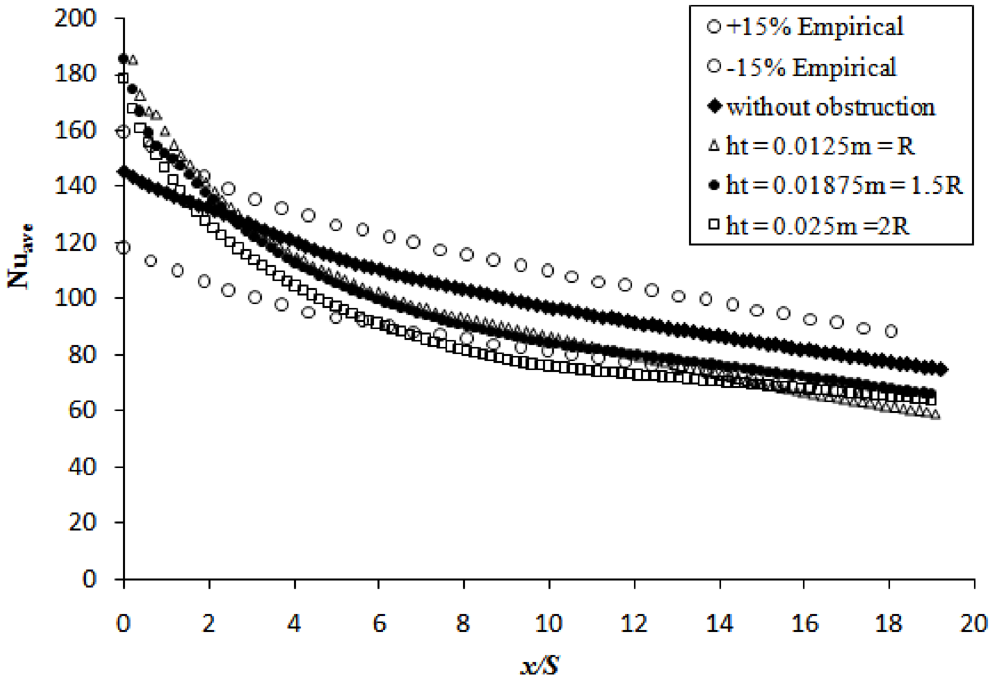

Figure 5.3 Comparison of Nusselt number distribution for various obstacle heights at constant obstacle spacing of 0.006 m.

A general trend shows low heat transfer from the stagnation region till half way on the wall-jet region from where all the profiles are almost parallel to the flat plate ave. Nu number values in the wall-jet region.

A a clear difference along the length is observed for h_{t3} = 0.025 m = 2R (case A9) indicating higher limit for obstacle distance from impinging surface at obstacle spacing of 0.006m.

At lower h_t value, higher Nu distribution exists closer to the stagnation region. At h_t = 0.025 m and d_t = 0.006 m, unlike in other cases takes the lagging position where it seperates its way witha margin of about 10 values amost till the end.

5.1.4 Comparison of Best Heat Transfer Results at Various Obstacle Spacing d_t

The best results obtained from the Figs. 5.1, 5.2 and 5.3 are plotted in Fig. 5.4 for the ease of comparison. Further, Nusselt number distribution for jet without mesh is also compared in order to clearly understand the variations. Fig. 5.4 reveals that $h_{t2} = 1.5R$ = 0.01875 and obstacle spacing of 0.005 m (case A5) gives the best Nusselt number distribution compared with all other parametric combination for the triangles model.

Further observations found in the study of this model are:

The effect of turbulence at the stagnation region due to the presence of mesh significantly increases the heat transfer only in that region for all the parametric combinations.

In cases with d_{t2} = 0.005 m, an increase in heat transfer curve at far wall-jet region is observed in general.

On observing for the best case, plot with h_{t2} = 0.0125 m & d_{t2} = 0.006 m dominates all of them only for half of its length, whereas the plot with h_{t2} = 0.01875 m, d_{t2} = 0.005 m has next higher values and maintains a good way to meet the flat plate values at x/S = 19. This indicates that a lower obstacle height and higher obstacle spacing is suitable for heat transfer enhancements using jet impingement technique.

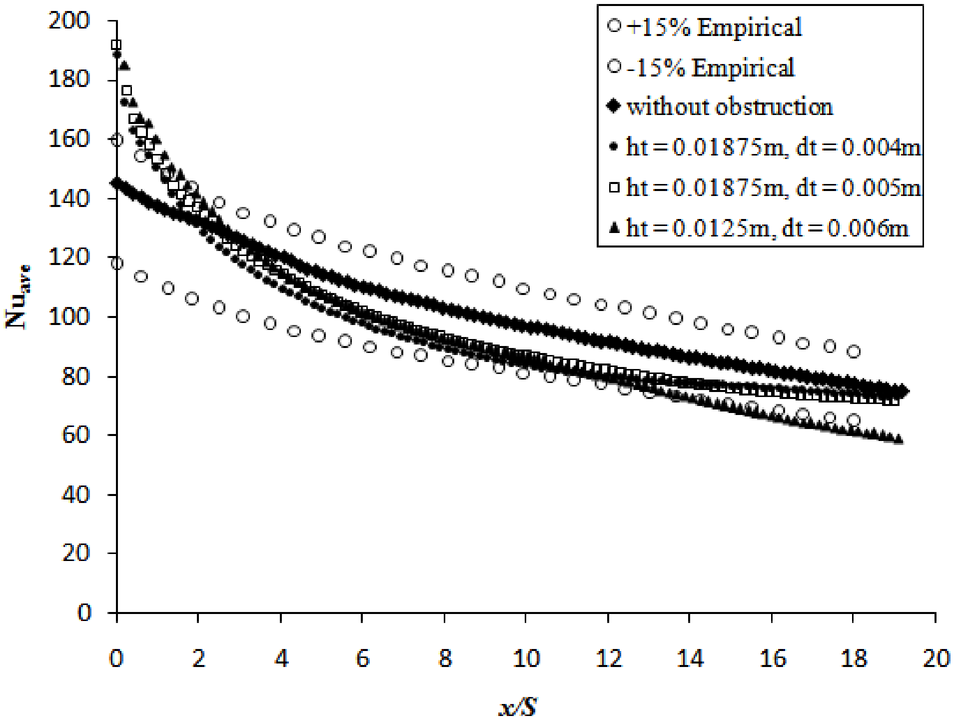

Figure 5.4. Comparison of best Nusselt number distribution plots for various obstacle spacing d_t

Using triangular cross section leads to a higher heat transfer of about 30% but only at the stagnation region ($x/S = 4$).

A lower heat transfer of maximum 15% after $x/S = 4$ is observed in most cases which gradually increases to zero or in other words meet the flat plate values at far wall-jet region.

An interesting fact noticed was, with the increase in the obstacle spacing d_t, the peak Nusselt number value near the stagnation region decreases.

The heat transfer enhancement can be increased by the use of multiple triangles above the stagnation region; but this will affect the heat transfer at wall-jet region.

The use of triangles enhances the turbulence at the stagnation region. This may enhance the heat transfer but soon the jet loses its dissipation potential. The flow induced acceleration in the wall-jet flow reduces and compensates the heat fluxes which in turn cause consistency in heat transfer along the wall-jet region.

A lesson learned from this investigation is, increase in turbulence outside the stagnation region should be focused and this should be done preserving the kinetic dissipation rate of the jet at the stagnation region .i.e., without using heavy obstructions which damp the kinetic energy of the jet.

5.2 Cylinder Model

Numerical simulation of a semi-circle (cylinder) as shown in Fig. 4.13 (a) was investigated with parametric variations as given in Table 4.3.Nine parametric combinations were simulated as given in Table 5.2 using FLUENT at convergence criteria of 10^{-6}. Each case took an average time of 3 days to converge.

Table 5.3 Parametric combination investigated in cylinder model

Case ID	Obstacle height (m)	Obstacle radius (m)	Associated Results
B1	0.009375	0.009375	Fig. 5.5
B2	0.0125	0.009375	Fig. 5.5
B3	0.015625	0.009375	Fig. 5.5
B4	0.009375	0.0125	Fig. 5.6
B5	0.0125	0.0125	Fig. 5.6
B6	0.015625	0.0125	Fig. 5.6
B7	0.009375	0.015625	Fig. 5.7
B8	0.0125	0.015625	Fig. 5.7
B9	0.015625	0.015625	Fig. 5.7

5.2.1 Effect of Cylinder Height at Constant Obstacle Radius r_{cyl1}

In order to analyze the effect of cylinder-to-target plate height h_{cyl} with constant cylinder radius r_{cyl1} on the heat transfer distributions was separately plotted for each value of h_{cyl} at all radii r_{cyl}. Figure 5.5 shows how heat is distributed along the impinging wall at different cylinder heights.

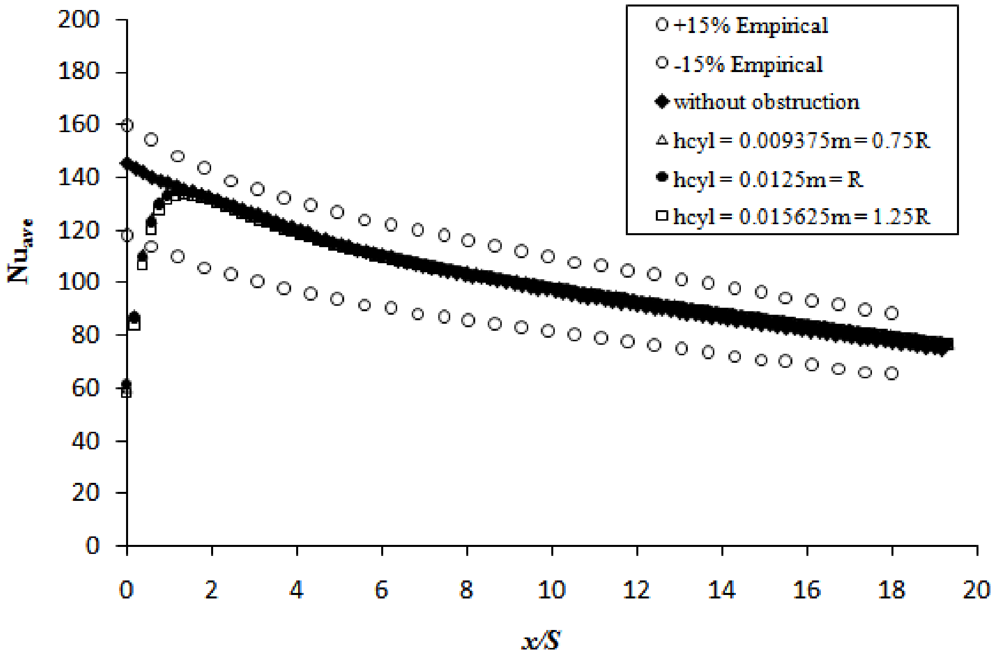

Figure 5.5 Comparison of Nusselt number distribution for various obstacle heights at constant obstacle radius of 0.009375 m

Heat transfer under the cylinder has high gradient of ave. Nu, starting from about 60 at *x*/*S* = 0 to 135 at x/*S* = 1. This is because of the obstruction where it is difficult for the high velocity flow to reach the bottom most point of the spherical shape.

The flow deviated due to the obstruction takes is attached half way through the surface of the cylinder and almost normally impinges the wall surface. The jet also forms a spray like distribution past the cylinder which gives higher heat transfer at the stagnation point newly formed at *x*/*S* = 3 due to placement of an obstruciton.

Almost 7% increase in the heat tranfer was observed from *x*/*S* = 1 to 4. A constant diference of 2-3% increase in ave. Nu was seen till the end of the wall-jet region.

No significant change was observed at cylinder radius $r_{\mathrm{cyl}\,1}$ at any cylinder heights.

5.2.2 Effect of Cylinder Height at Constant Obstacle Radius r_{cyl2}

The results obtained for Nusselt number distribution for various cylinder-to-plate distance h_{cyl} at constant cylinder radii r_{cyl} are given in Fig. 5.6.

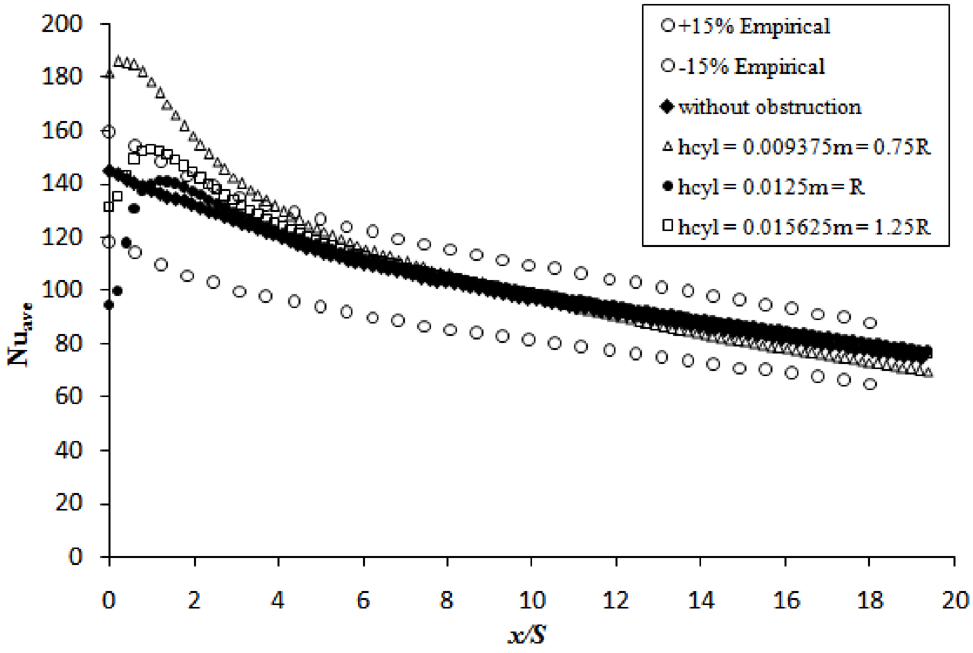

Figure 5.6 Comparison of nusselt Number distribution for various obstacle heights at constant obstacle radius of 0.0125 m

Unlike in the previous cases, the wall under the cylinder is well heated at this cylinder radius ($r_{cyl} = R = 0.0125$ m). At $h_{cyl1} = 0.009375$ m ($0.75R$) and $h_{cyl3} = 0.015625$ m ($1.25R$), ave. Nusselt number under the cylinder is almost equal or greater than that of flat plate validation values; h_{cyl1} being exceptionally higher at the stagnation region.

At cylinder radius $r_{cyl2} = 0.0125$ m $= R$, $h_{cyl1} = 0.009375$ m ($0.75R$) gives an increase in heat trasnfer from as high as 30% at stagnation region to 10% at $x/S = 5$. The curve later superimposes the curve without obstruction from $x/S = 11$ to $x/S = 20$. Results with obstacle height, h_{cyl2} = 0.0125m = R curve is similar to cases of cylinder radius r_{cyl1}, where the only difference is that at x/S = 0 the ave. Nu value is 95 instead of 60. At obstacle height h_{cyl3} = 0.015625m = 1.25R gives about 15% of increase in heat tranfer and gradually decreases to 2-3% at far wall-jet region.

A significant change in heat transfer is seen at the stagnation region and region near by due to changes in cylinder-to-plate distance.

5.2.3 Effect of Cylinder Height at Constant Obstacle Radius r_{cyl3}

The results obtained for Nusselt number distribution for various cylinder-to-plate distance of h_{cyl} at constant cylinder radii r_{cyl} are given in Fig. 5.7.

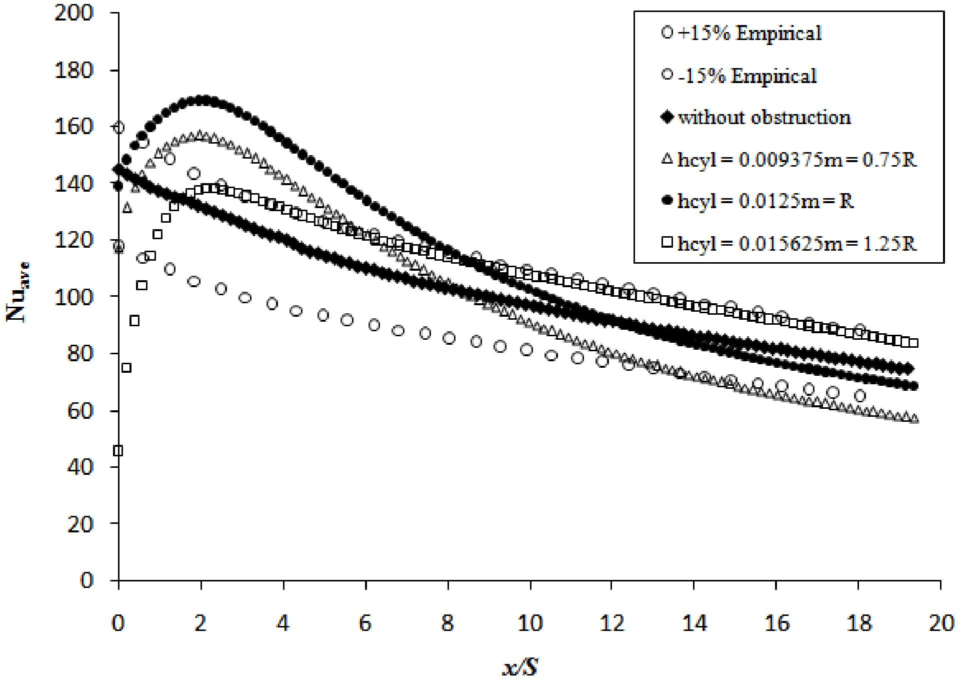

Figure 5.7 Comparison of nusselt number distribution for various obstacle heights at constant obstacle radius of 0.015625 m

A diversified yet interesting results were obtained for different cylinder-to-plate distances for cylinder radius r_{cyl3} = 0.015625m = 0.75R.

In the case with r_{cyl3} = 0.015625m = 1.25R and h_{cyl2} = 0.0125m = R in Fig. 5.7, the heat tranfer from x/S = 0 to 7 is satisfactory but later, a lower than expected heat is transfered till x/S = 20. A similar profile can be seen at higher obstacle height h_{cyl} but with an increased difference of about 15%.

Although the case with h_{cyl} = 0.015625 m curve gives low heat transfer at stagnation region, it maintains an increased value of heat transfer of about 15% almost throughout the wall-jet region.

5.2.4 Comparison of Best Heat Transfer Results at Various Obstacle Radius r_{cyl}

A through observation of the Figs. 5.5, 5.6 and 5.7 reveals best plots as shown in Fig. 5.8. Thus a comparison of these three plots with the results of flat plate is made in Fig. 5.8. The result clearly shows that case with h_c = 0.015625 m and r_c = 0.015625 m is the best parametric combination for the cylinder model.

Further observations found in the study of this model are as follows:

In all the plots a good increase in heat transfer at stagnation region is observed.

As the radius of the cylinder increases, the peak of the maximum heat transfer shifts away from the jet-centerline. This could be due to jet deflection due to cylinder radius higher than the nozzle radius.

In all the parametric combinations, plots associated with r_{cyl3}= 0.015625m = 1.25R give an outstanding augmentation in heat transfer not only at the stagnation region but also the wall-jet region.

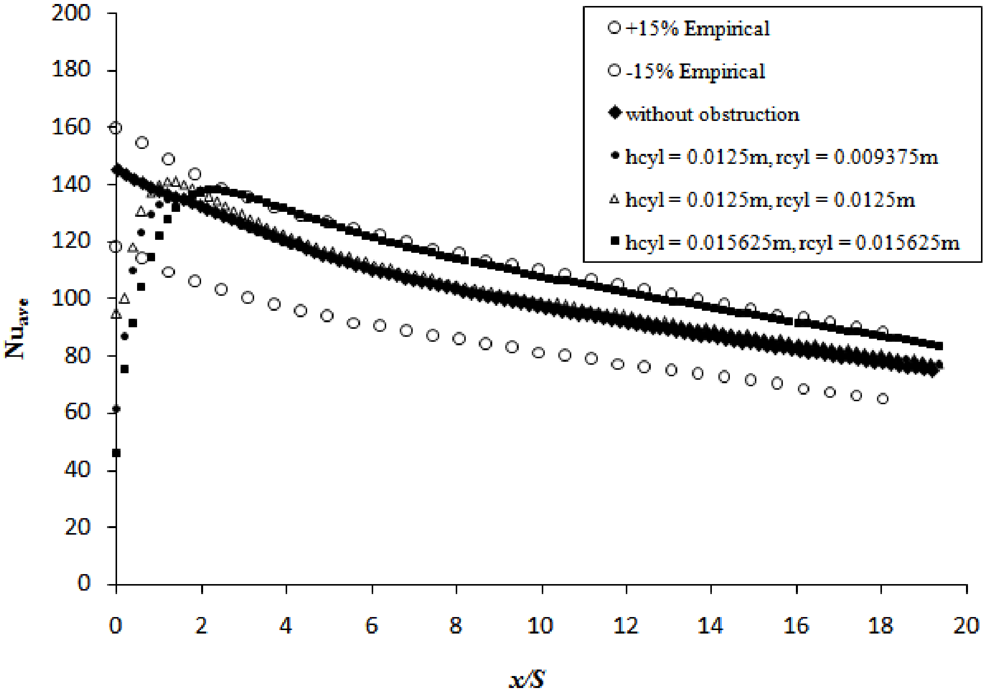

Figure 5.8 Comparison of best Nusselt number distribution for various obstacle radius r_{cyl}

Almost no change is seen in plots of low cylinder radius r_{cyl}, implying negligible effect of cylinder at $r_{cyl} < R$.

On comparing the best plot for different cylinder radii and cylinder-to-plate distance, almost all the curves gives low heat tranfer in the region below the cylinder, a significant increase in the heat transfer is seen till the end with a difference of about +15% for h_{cyl} = 0.015625 m and r_{cyl} = 0.015625 m.

Cylinder radius $r_{cyl1} = 0.75R$ and $r_{cyl2} = R$ allow the jet to impinge on the wall directly under the obstacle, hence the peak of heat heat transfer starts earlier than in the case of $r_{cyl3} = 1.25R$.

All the three curves maintain an increased heat transfer margin to the flat plate values. The first two cases maintain from about 10% near the stagnation to 2-3% along the wall-jet region, where as the third case with $h_{cyl} = 0.015625$ m and $r_{cyl} = 0.015625$ m maintains more than 15% near the stagnation to more than 10% along the wall-jet region.

The best combination of cylinder radius r_{cyl} and cylinder-to-plate distance h_{cyl} stands exceptionally in the Fig. 5.8. The case with r_{cyl3}= 0.015625m = 1.25R, h_{cyl2} = 0.015625m = 1.25R can enhance the heat transfer to about 15% from a conventional jet impingment on a flat plate.

5.3 Wedge Model

Numerical simulation of a wedge model as shown in Fig. 4.15 (a) was investigated with parametric variations as given in Table 4.4 .Twelve combinations of obstacle height and top-angle were simulated as given in Table 5.3 using FLUENT at a convergence criteria of 10^{-6}. Each case took an average time of 4 days to converge.

Table 5.4 Parametric combination investigated in wedge model

Case ID	Obstacle height (m)	Obstacle angle (^{o})	Associated Results
C1	0.0125	20	Fig. 5.9
C2	0.01875	20	Fig. 5.9
C3	0.025	20	Fig. 5.9
C4	0.0125	30	Fig. 5.10
C5	0.01875	30	Fig. 5.10
C6	0.025	30	Fig. 5.10
C7	0.0125	40	Fig. 5.11
C8	0.01875	40	Fig. 5.11
C9	0.025	40	Fig. 5.11
C10	0.0125	50	Fig. 5.12
C11	0.01875	50	Fig. 5.12
C12	0.025	50	Fig. 5.12

5.3.1 Effect of Wedge Height at Constant Wedge Top Angle θ_1

In order to analyze the effect of wedge-to-target plate height h_w at constant wedge angle θ_1, Nusselt number distributions were plotted for each wedge-to-target plate height at all angles θ at the top of the wedge. Fig. 5.9 shows the how the heat is distributed along the impinging wall at different wedge heights at wedge top-angle θ_1 = 20-deg.

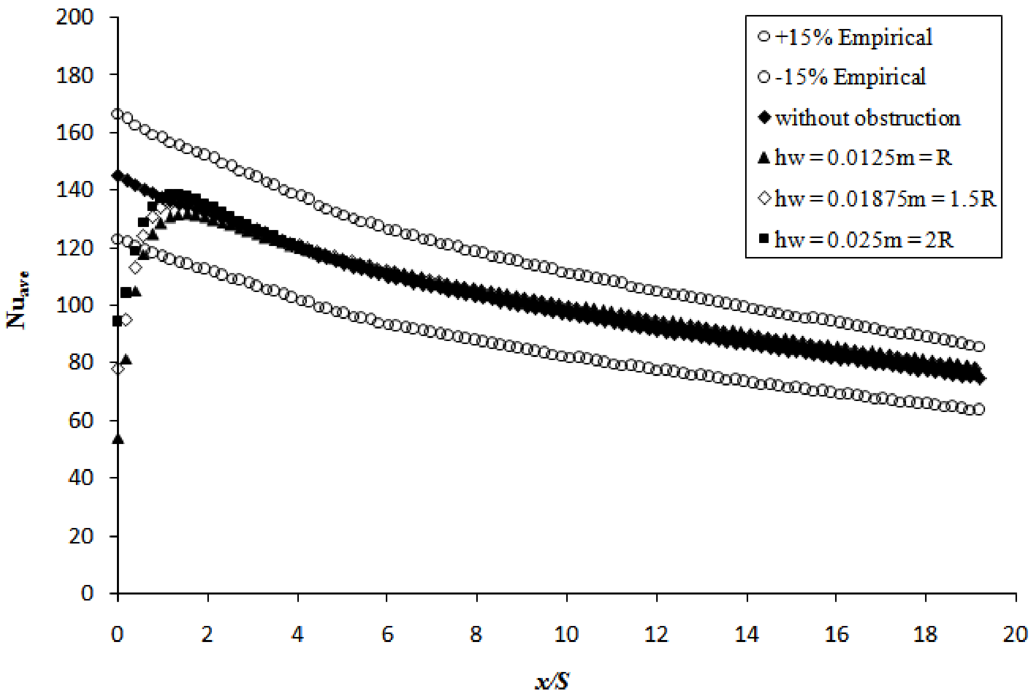

Figure 5.9 Comparison of Nusselt number distribution for various obstacle heights at constant wedge top angle of 20-deg.

Identical heat transfer distribution is observed on placement of a wedge with top half-angle of 20^o at different wedge-to-plate distances.

The heat transfer at stagnation point (x/S = 0) is well below the flat plate values,but they increase as the wedge-to-plate distance increases.

The peak of heat transfer for all wedge-to-plate distances at θ_1 = 20 shifts at about x/S = 1.5.A 7% increase is commonly seen in all cases at the newly formed eccentric stagnation point x/S = 2.

A 2-3% increase in the heat transefer is observed at a wall-jet distance of x/S = 6 in case of h_w = 0.0125m = 1R. The best curve suggested among these cases that with θ_1 = 20^o, h_w = 0.0125m = 1R.

5.3.2 Effect of Wedge at Constant Wedge Top Angle θ_2

Unlike in Fig. 5.9, Fig. 5.10 shows an explicit difference in the heat transfer distribution plots at different wedge-to-plate distances.

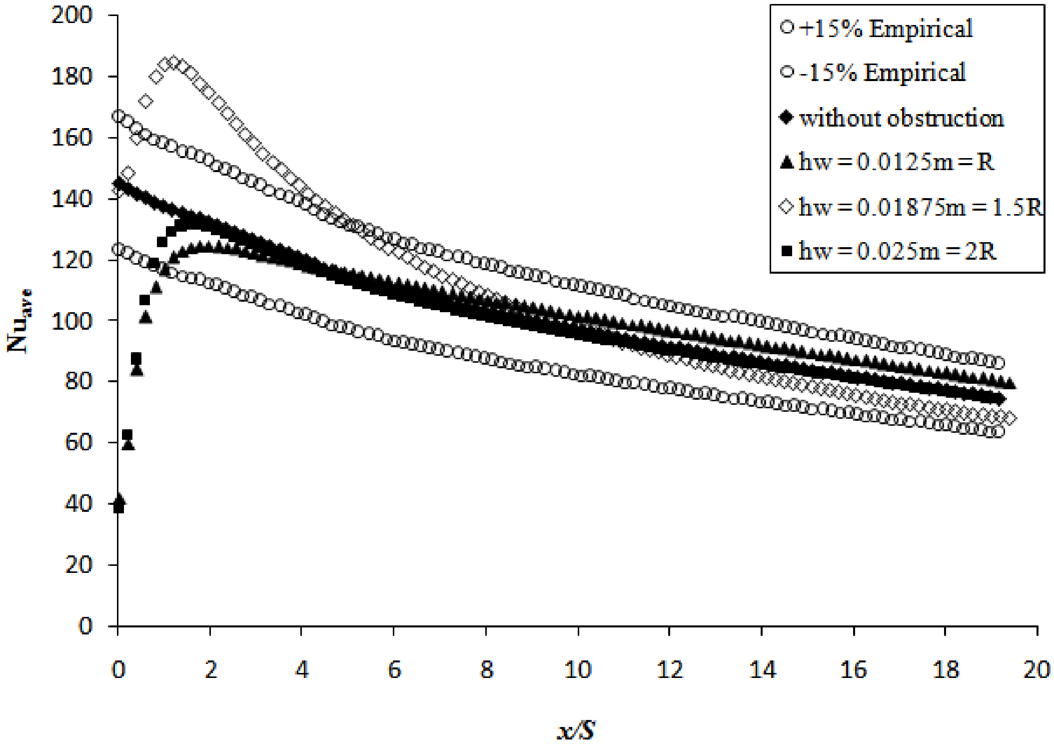

Figure 5.10 Comparison of Nusselt number distribution for various obstacle heights at constant wedge top angle of 30-deg.

At obstacle height h_w = R = 0.0125m, the plot raises from 40 at x/S = 0 to cross the intercept of flat plate values at x/S = 2 maintaining about +5% of difference thereafter. At obstacle height h_w= 0.025m = 2R curve stays ahead of the validation only from x/S = 1 to 5, after which maintains the same heat distribution as in the flat plate case.

The obstacle at h_w = 0.01875m = 1.5R has an exceptionally enhanced heat transfer distribution till half of the domain lenght (x/S = 0 to 10), after which a 5% decrease in heat trasnfer was observed. A uniform enhanced heat transfer distribution is only seen at h_w = 0.0125m = R.

5.3.3 Effect of Wedge at Constant Wedge Top Angle θ_3

Heat transfer distribution on impinging plate due to the wedge at cone angle θ_3 produced stable results but with very less improvement in Nusselt number distribution. However, a better results than those obtained previously from cone angel θ_1 are shown in Fig. 5.11.

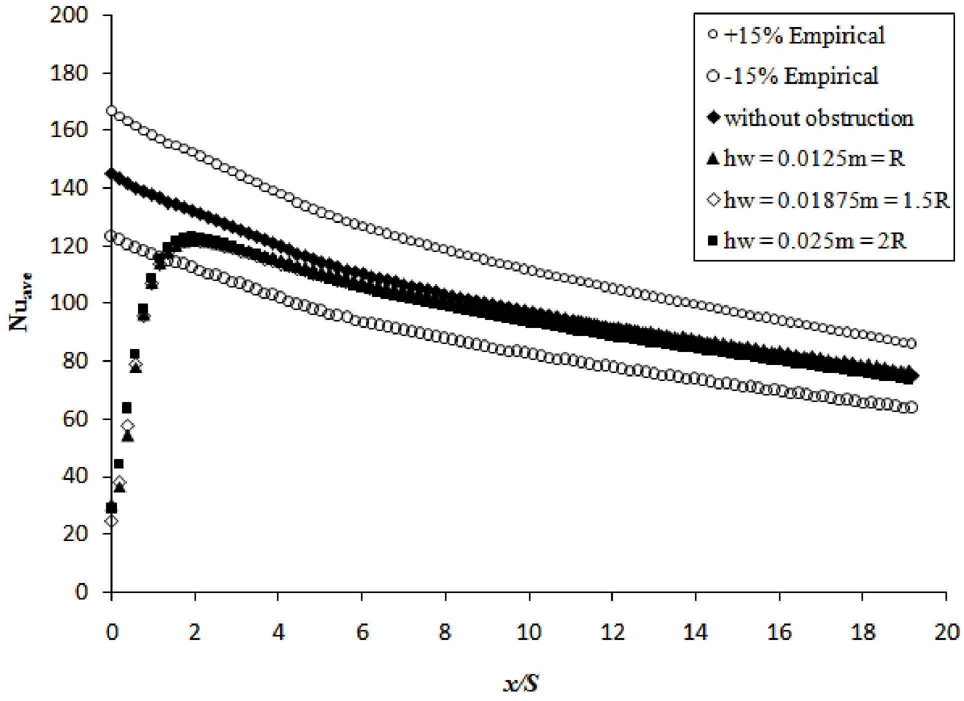

Figure 5.11 Comparison of Nusselt number distribution for various obstacle heights at constant wedge top angle of 40-deg.

The heat transfer distribution for this case is maintained lower to that of validation case. The lower values can be seen from x/S = 0 to x/S = 8 along the wall-jet region.

The stagnation region under the obstruction (*x*/*S* = 0) starts at a Nu value of about 30 for all wedge-to-plate distances but cannot meets the flat plate values untill *x*/*S* = 10.

No significant improvement is seen and hence no combination can be picked as the best in this case.

5.3.4 Effect of Wedge at Constant Wedge Top Angle θ_4

Fig. 5.12 explicitly reveals that any further increase in the wedge top-angle does not affect the heat transfer distribution. The Fig. 5.12 suggests ending further analysis by increasing the value of θ.

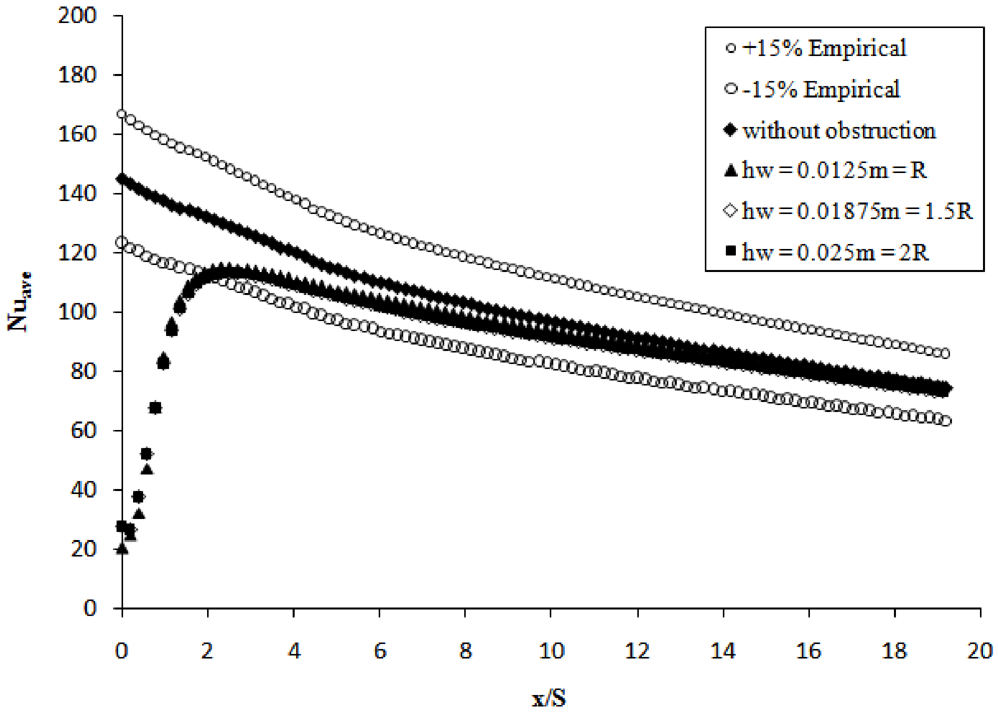

Figure 5.12 Comparison of Nusselt number distribution for various obstacle heights at constant wedge top angle of 50-deg.

From Fig. 5.12, it is observed that this combination of θ_4 and h_w does not give satisfactory results. Although an anticipitated heat transfer distribution profile was observed, the ave. Nu values clearly lie below the numerical values through out its length. This symbolizes a limitation of using top wedge-angle as an obstruction in jet impingment technique under the present problem conditions .

Previously, the low heat transfer at the stagnation region was compensated by higher values on the wall-jet region, but in this case a 2-5% decrease in heat transfer was observed along the wall-jet region including a huge loss of heat at the stagnation region.

5.2.5 Comparison of Best Heat Transfer Results at Various Wedge Top Angles

In an observation, best plots in Figs. 5.9, 5.10 and 5.11 were selected and plotted to obtain the most effective combination of parameters in this model. The results were plotted in comparison with the result obtained without using a wedge. Fig. 5.13 reveals that case with $\theta_2 = 30^o$, $h_w = 0.0125$ m = R has higher values of nusselt number through out the wall-jet region by compensating the heat at stagnation region which is the objective of this study.

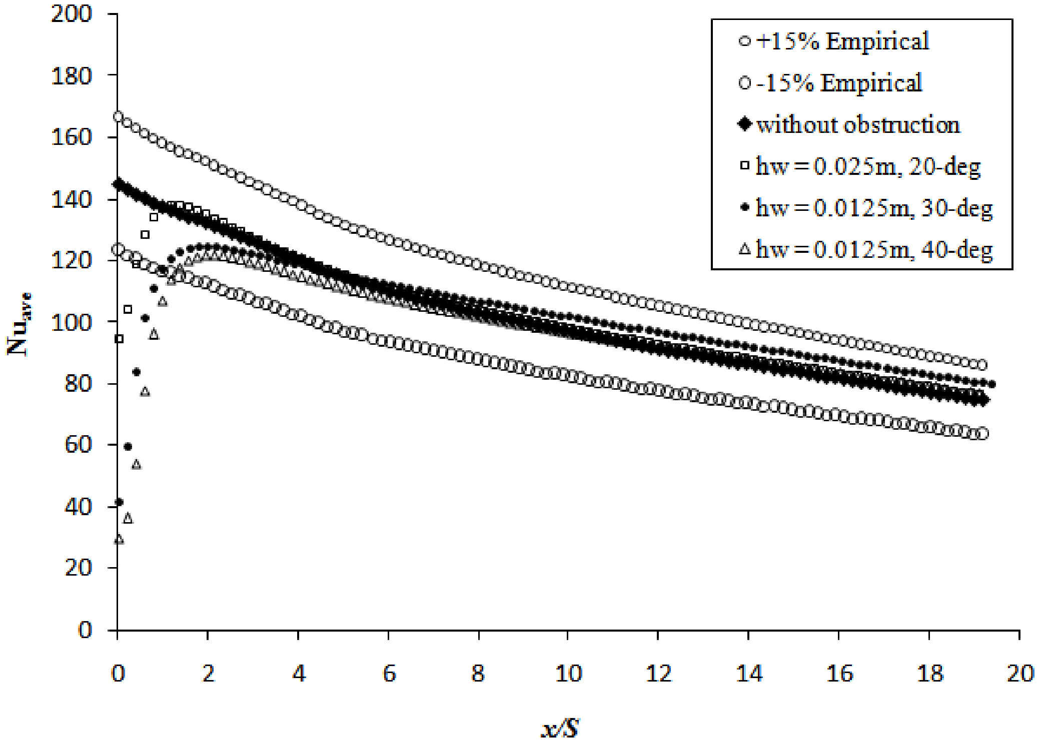

Figure 5.13 Comparison of best Nusselt number distribution for various wedge top angles

Further observations in the study of this model are

The heat transfer curves were selected only from case with$\theta_1 = 20^\circ$, $h_w = 0.0125$ m $= R$ to case with $\theta_3 = 40^\circ$, $h_w = 2R$ combinations as the results of poor results obtained from θ_4 wedge half-angle.

A closer observation reveals that although at $\theta_1 = 20^\circ$, $h_w = 0.025$ m $= 2R$ gives good heat transfer near the stagnation region, it doesn't satisfactorily continues along the wall-jet region.

At $\theta_2 = 30^\circ$, $h_w = 1.5R$ and $\theta_3 = 40^\circ$, $h_w = R$, it seems to have a stable heat transfer distribution along the length of empirical curve but at $\theta_2 = 30^\circ$, $h_w = 0.0125$ m $= R$ a 4-5%

higher heat transfer than the flat plate results along the wall-jet region was observed. The case with $\theta_2 = 30^{\circ}$, $h_w = 0.0125$ m = R gives a satisfactory enhancement in heat transfer distribution along the wall-jet region.

5.4 Channel

Numerical simulation of a channel model as shown in Fig. 4.17 (a) was investigated with parametric variations as given in chapter 4 .Six parametric combinations were simulated to get an optimal length and shortest distance of channel-to-jet centerline distance using Fluent ® version 6.2. The convergence criteria used for this model was of 10^{-6}. Each case required an average time of 2 days to converge.

5.4.1 Effect of Channel Height on Heat Transfer Distribution

The optimal channel length (d_{ch} = 0.5 m) as mentioned in section 4.4.4 was used at different channel-to-plate distance h_{ch} as listed in Table 5.4. The heat transfer distribution for each value of h_{ch} is shown in Fig. 5.14.

Table 5.5 Parametric range of channel-to-plate height h_{ch}

Case ID	**h_{ch} (m)**	**Associated Results**
D1	0.013	Fig. 5.14 (a)
D2	0.014	Fig. 5.14 (a)
D3	0.015	Fig. 5.14 (a)
D4	0.016	Fig. 5.14 (b)
D5	0.017	Fig. 5.14 (b)

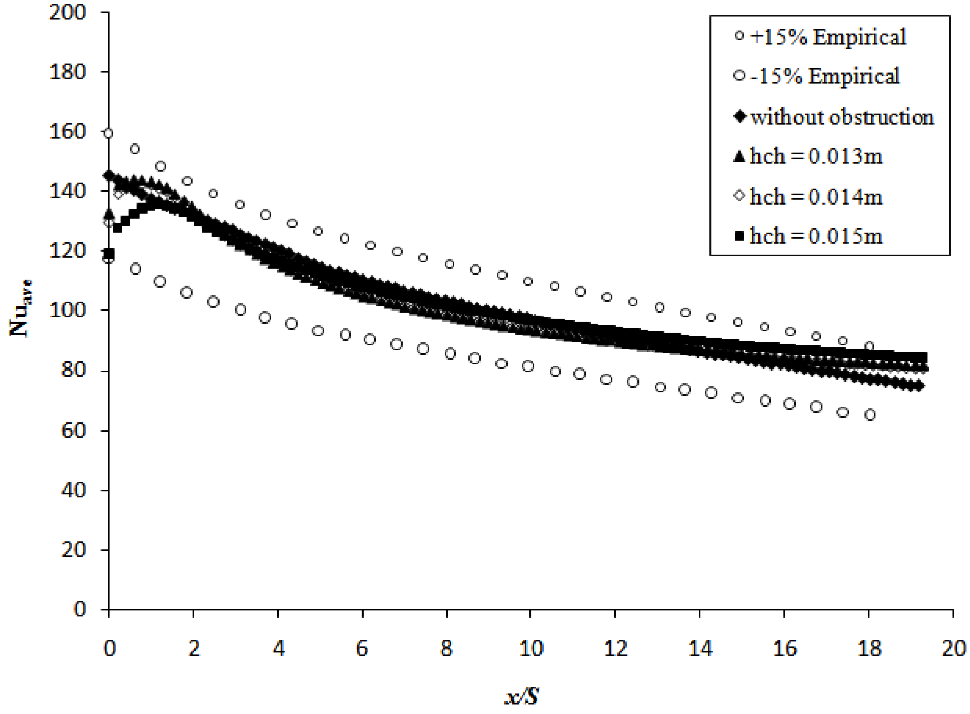

(a)

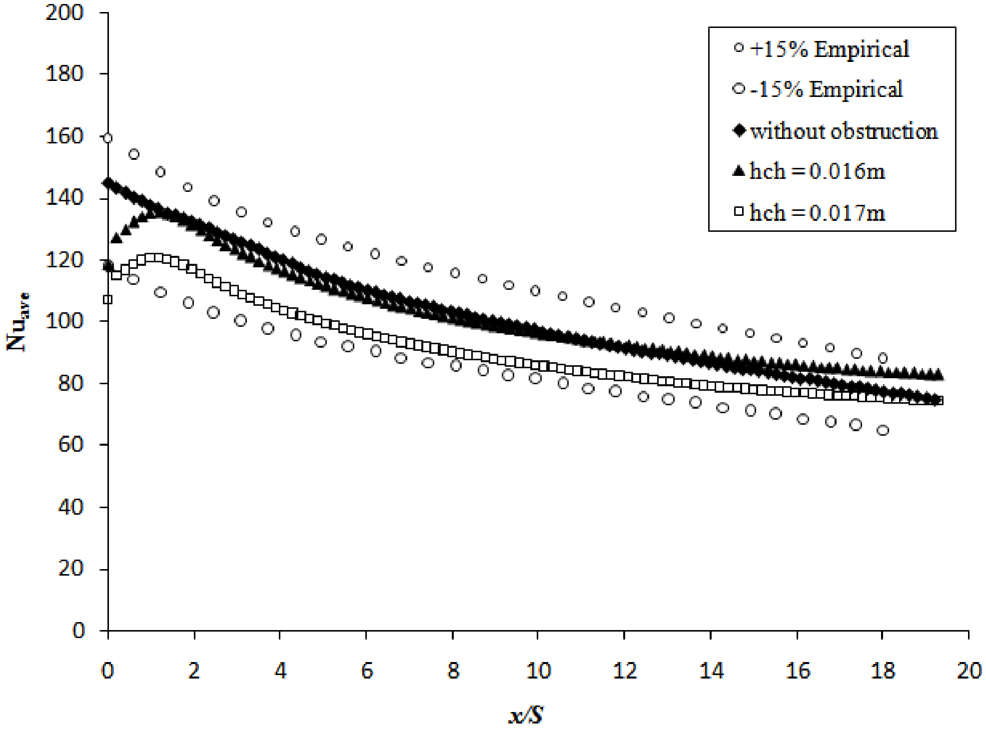

Figure 5.14 Comparison of Nusselt number distribution of channel for various channel-to-plate height h_{ch}

Heat transfer at the stagnation region decreases as the height of the channel increases to a certain level due to fewer obstruction created by the channel start.

In Fig. 5.14 (a), the sag in the heat transfer distribution profile superimposes the values of flat plate from about $x/S = 5$ to 12 which implies no heat transfer enhancement in this region. Heat transfer after $x/S = 14$ increases gradually to about 5%.

In Fig. 5.14 (b), the heat transfer distribution profile remains almost similar in all the cases except that it lowers as the height of the channel increases from 0.016 to 0.017m which explains a higher limit for channel height.

Increasing the height of the channel above $h_{ch}/R = 1.2$ ($h_{ch} = 0.015$ m) gradually decreases the overall heat transfer distribution.

5.4.2 Best Heat Transfer Results for Channel Height

From Fig. 5.14 (a), heat transfer improved at $h_{ch3} = 0.015$ when compared to other cases. A comparison between heat transfer with and without a channel (see Fig. 5.15) reveal a significant raise in the heat transfer at far wall-jet region.

A few other observations can be concluded from the study conducted on this model.

Since the channel was an open ended channel with a limited evaluated length, it did not provide the necessary pressure on the boundary layer to augment the heat flux.

As the height of the channel increased, the heat transfer distribution increased to a maximum level and then dropped to a lower level. The maximum level being at the channel height of 0.015 m or $h_{ch}/R = 1.2$. Hence, the best height for an open ended channel near an impinging jet to enhance heat transfer is 0.015 m or $h_{ch}/R = 1.2$.

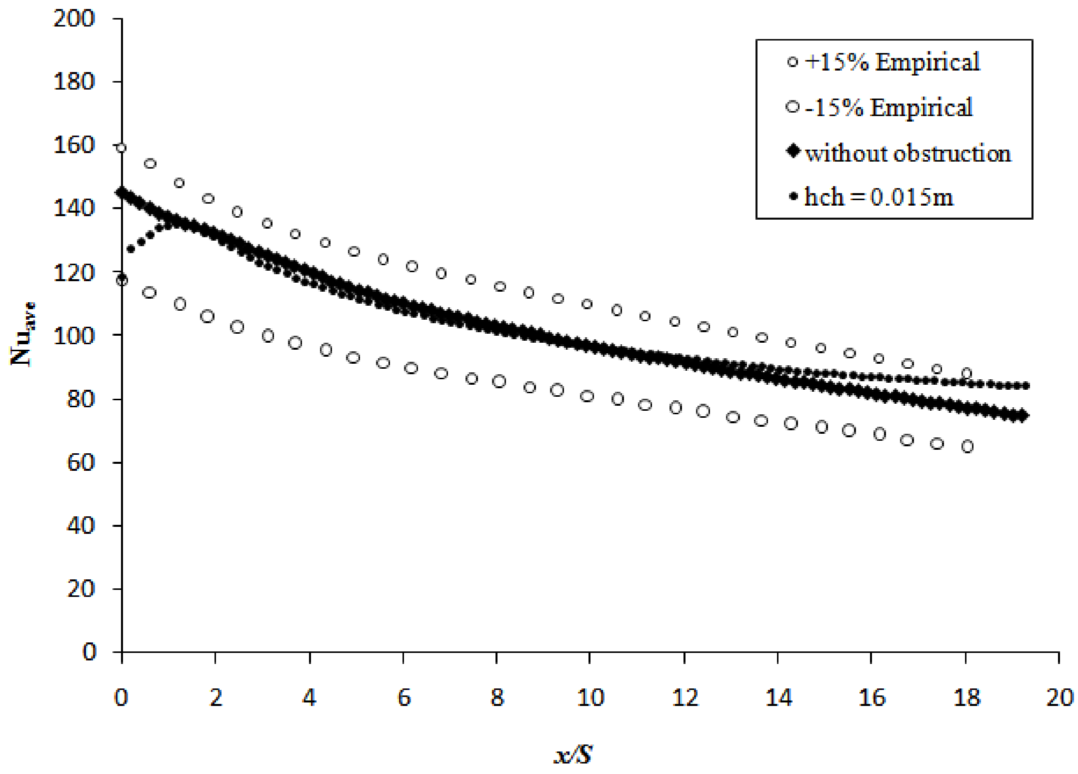

Figure 5.15 Comparison of best Nusselt number distributions for channel model at channel-to-plate height h_{ch3} = 0.015

A common trend was followed in the heat transfer distribution of all the plots at the channel exit. This effect may be due to shear induced turbulence created in the flow at the exit of the channel.

After the stagnation point, a little drop in the heat distribution values was seen for all the plots at the point where the channel starts. Due to presence of confinements with open wall boundaries, the flow acceleration within the channel was observed. With this acceleration and abrupt ending of the channel wall, a turbulence affecting the heat transfer after the channel exit was created.

A learned phenomenon from this model is that an open ended channel used for jet impingement can enhance the heat transfer only at the exit of the channel due to high velocity and low pressure within the channel. This makes the technique applicable for user defined distances to enhanced turbulence and heat transfer along the wall-jet region.

5.5 Vortex Generator

Numerical simulation of a channel model as shown in Fig. 4.20 was investigated with parametric variations as given in Table 4.4 .Seven VG angles were simulated to get an optimal angle and VG height. The convergence criterion was set at of 10^{-6}. Each case required an average time of 3 days to converge.

5.5.1 Effect of VG Height at Various VG Angles

Simulations for VGs in Table 4.4 were conducted for a single VG placed on the impinging wall at a distance of 0.2 m from the jet-centerline. This distance of VG from the jet-centerline was chosen considering the following criteria

- The wall-jet flow should be at an average Reynolds number at this region.
- The VG placement on the impingement wall is where the slope of plot in Fig. 4.9 increases starting from the stagnation region.

Fig. 5.16 (a) and (b) show the heat transfer is effect due to the presence of VG at different angles. The values of VG angle φ, VG length l_{vg} and VG height h_{vg} are listed in Table 5.5.

Table 5.6 Parametric combinations investigated in VG model

Case ID	**Obstacle height h_{vg} (m)**	**Obstacle angle φ_{vg} (^{o})**	**Corresponding obstacle length l_{vg} (h_{vg})**	**Associated Results**
E1	0.0015	26.5	2 h_{vg1}	Fig. 5.16
E2	0.0015	45	h_{vg1}	Fig. 5.16
E3	0.0015	63.4	0.5 h_{vg1}	Fig. 5.16
E4	0.0015	84.3	0.1 h_{vg1}	Fig. 5.16
E5	0.0015	100	0.18 h_{vg1}	Fig. 5.16
E6	0.001	120	0.57 h_{vg1}	Fig. 5.17
E7	0.001	140	1.2 h_{vg1}	Fig. 5.17
E8	0.0005	120	0.57 h_{vg1}	Fig. 5.17
E9	0.0005	140	1.2 h_{vg1}	Fig. 5.17

In Fig. 5.16 (a) and (b), a small step can be seen at x/S = 4 where the VG is placed. The step resemble the effect of eddies due to the applied VG angle. This is usually negligible and cannot be distinguished on comparison. Hence, VG height is considered more important than the VG angle as it affects the boundary layer attachment at local Reynolds number.

VG angles φ_{vg6} and φ_{vg7} were tested for different heights and significant increase in heat transfer was observed. φ_{vg6} and φ_{vg7} were correspondingly tested for VG heights h_{vg2} = 0.001 m and h_{vg3} = 0.0005 m are shown in Fig. 5.17 (a) and (b).

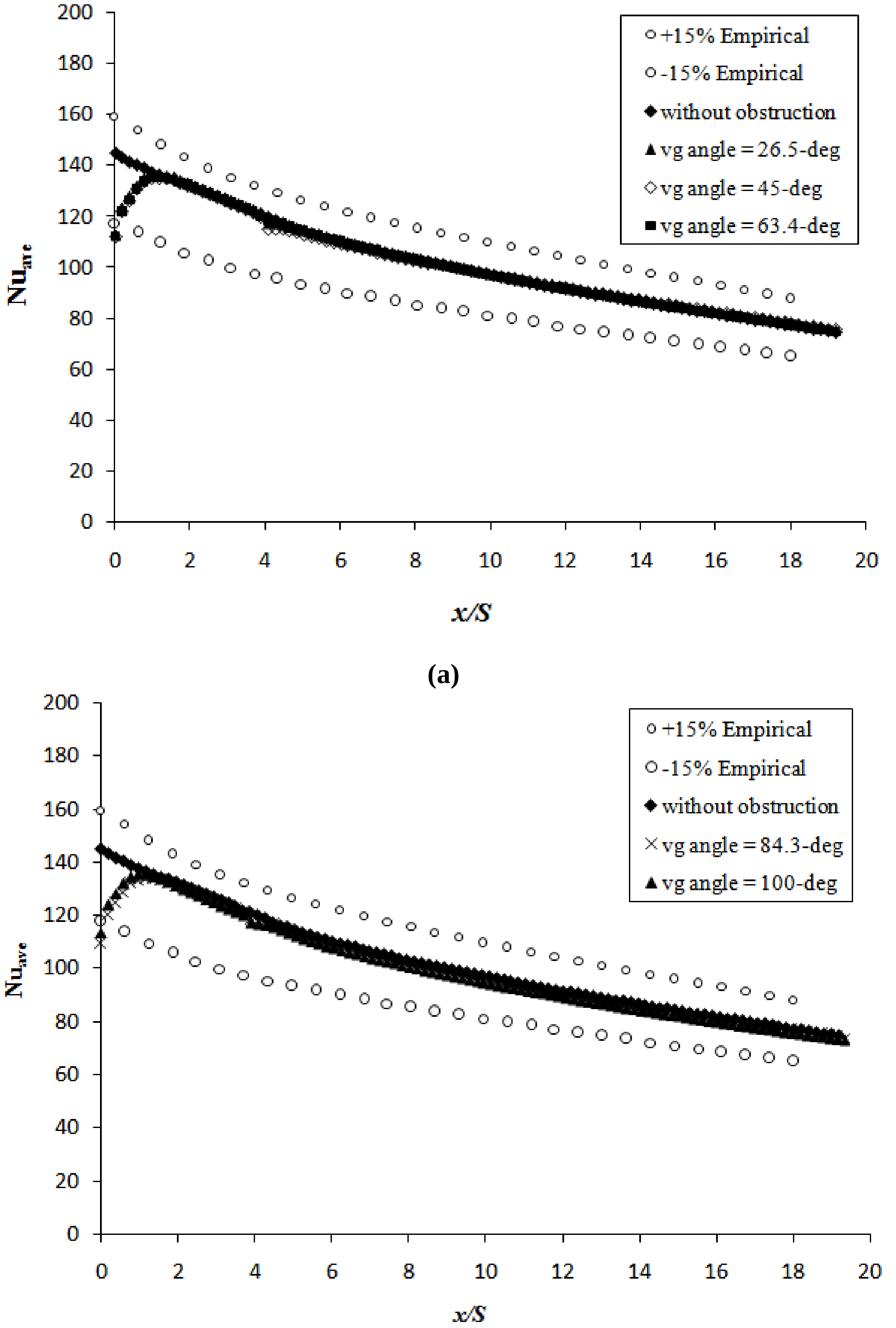

(a)

(b)

Figure 5.16 Comparison of Nusselt number distribution at various VG angles for constant VG height of 0.0015 m

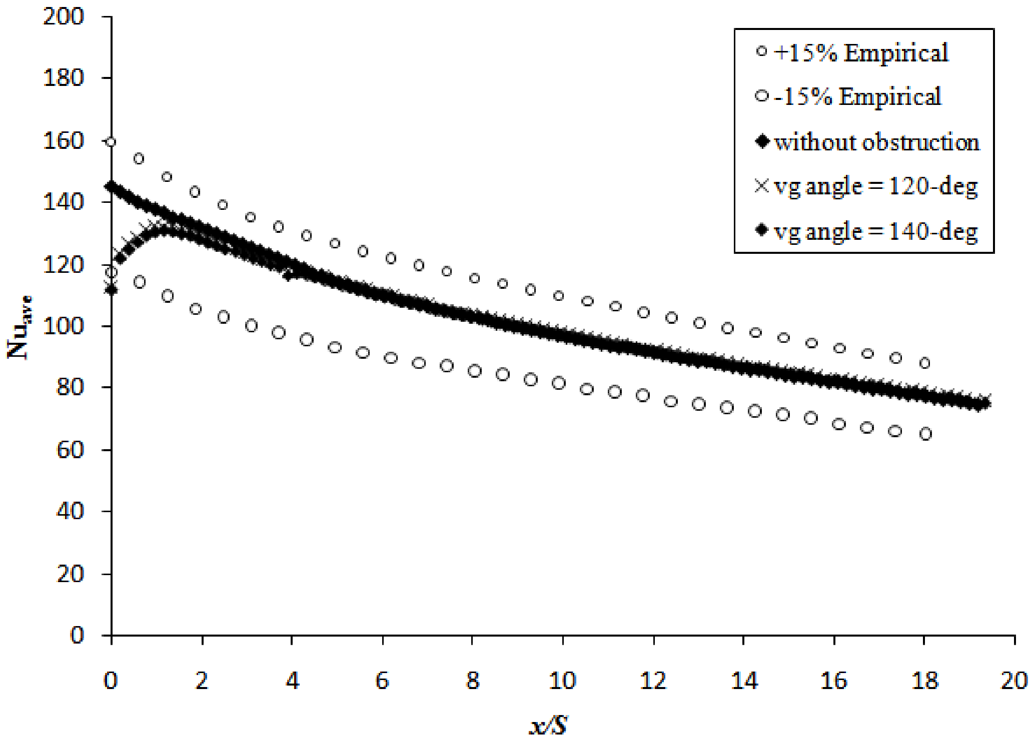

(a)

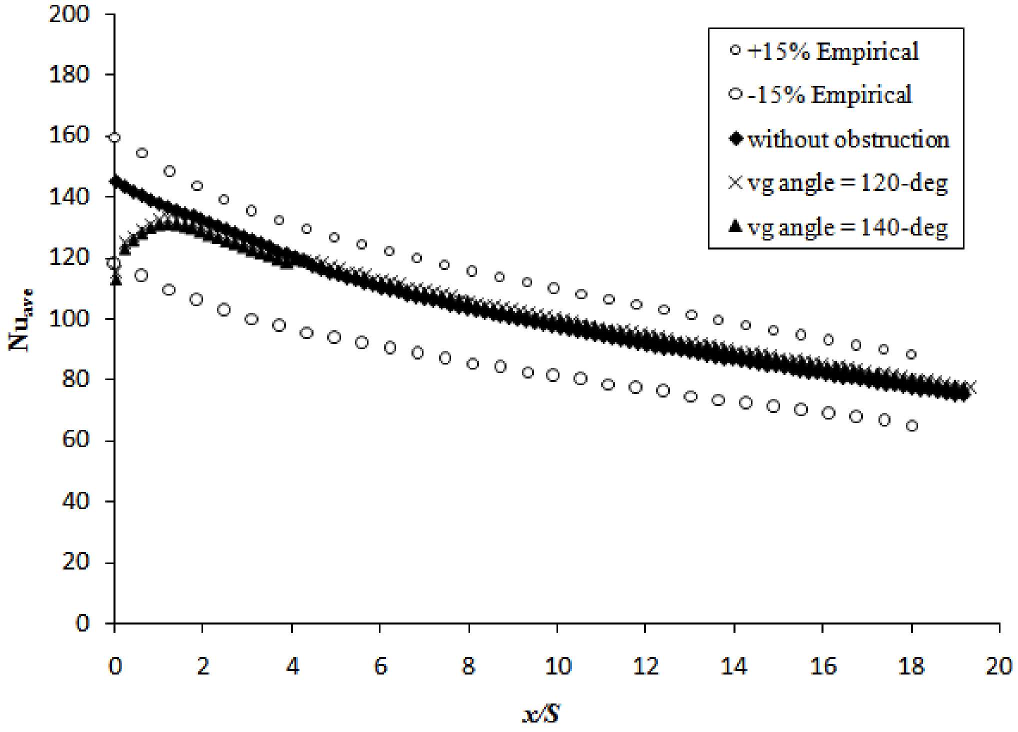

(b)

Figure 5.17 Comparison of Nusselt number distribution at various VG angles for VG heights 0.001 and 0.0005 m

Both the plots in Fig. 5.17 are identical except that the distance from the flat plate values is more in 5.17 (a) than in 5.17 (b) i.e., h_{vg3} = 0.0005 m gives better heat transfer than h_{vg2} = 0.001 m.

5.5.2 Periodic placement of VG

Analyzing Fig. 5.16 and Fig. 5.17, $\varphi_{vg6} = 120^o$, h_{vg} = 0.0005 m plot gave the best heat transfer in its category. Precise placement of multiple VGs on the wall is a vital step before finalizing the overall heat transfer enhancement. Observing the heat transfer distribution from Fig. 5.17, the fluctuation in the curve due to VG at point $x/S = 4$ suggests to place the next VG on the wall where the corresponding curve increases in its slope resulting in Fig. 5.18. After careful observation of the effect of VG on the heat transfer curve, each VG was then place at x/S = 4, 7 and 10 on the impinging wall. The result was then compared with the empirical data as shown in Fig. 5.18.

Other important findings were also observed in this study

Vortex genertors are effective means of heat transfer enhancement, but only in their proximity.

Usually, VGs are to be placed such as their inclination is with the flow, but in the case of jet impingement, the angle should be against the flow. This is proved from the Fig. 5.16 and Fig. 5.17. As the vortex angle increase the peak value of heat transfer associated with it also raises.

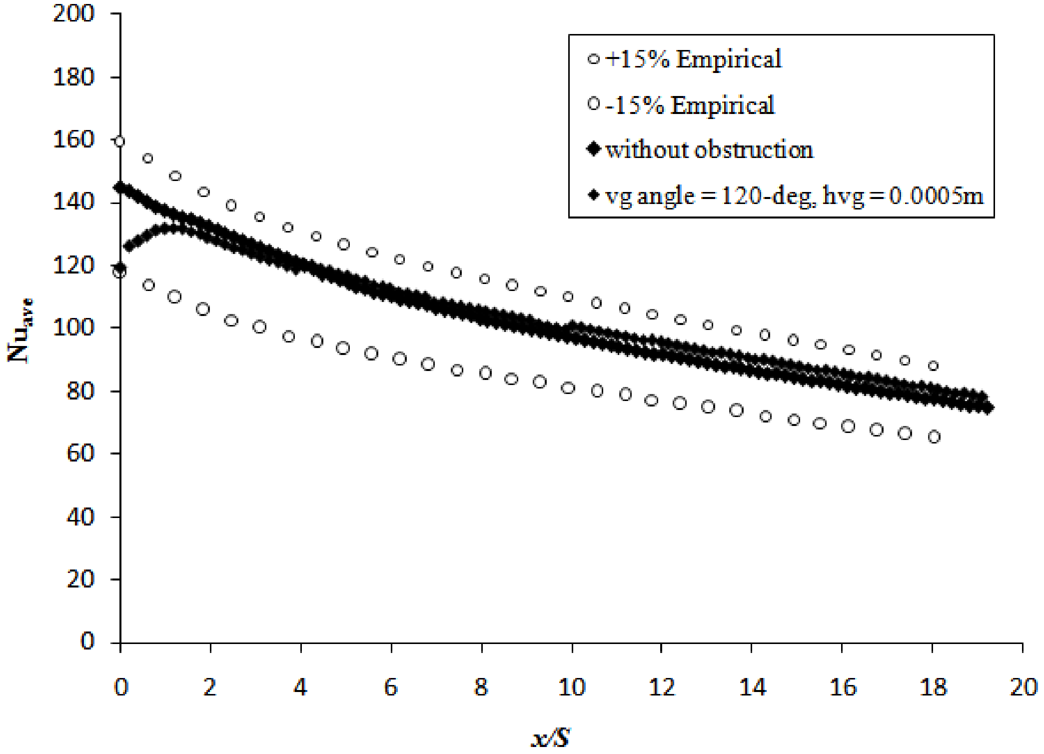

Figure 5.18 Comparison of Nusselt number distribution of flat-plate with multiple VGs and empirical data range.

Vortex generators cause a sudden step covering a distance to settle in the heat transfer distribution. This is simply the region before and after the VG where the flow is effected.

In a 2-dimensional study, the effect of vortex angle in xz plane cannot be considered where most of the studies used either an experimental analysis or a 3-dimensional domain including an angle in z-axis.

An interesting discovery in this model is, the angle of VG cannot be increased above 90^o unless its height is well below the boundary layer thickness.

5.6 Cavity

Numerical simulation of a channel model as shown in Fig. 4.22 was investigated with parametric variations as given in Table 4.5 and 4.6. A more simplified and easy to understand representation is listed in Table 5.4.

Table 5.7 Parametric models investigated in cavity model

Case ID	Obstacle length l_c (m)	Inter-obstacle distance d_c (m)	Obstacle radius r_c (m)	Corresponding cavity depth (m)	Associated Results
F1	0.06	0.04	0.05	0.01	Fig. 5.19
F2	0.05	0.05	0.05	0.0067	Fig. 5.19
F3	0.04	0.06	0.05	0.00417	Fig. 5.19
F4	0.06	0.04	0.06	0.008	Fig. 5.20
F5	0.05	0.05	0.06	0.00545	Fig. 5.20
F6	0.04	0.06	0.06	0.00343	Fig. 5.20
F7	0.06	0.04	0.07	0.00675	Fig. 5.21
F8	0.05	0.05	0.07	0.0046	Fig. 5.21
F9	0.04	0.06	0.07	0.00292	Fig. 5.21

Nine cases categorized into three major cases according to cavity length l_c were simulated with a convergence criterion of 10^{-6}. Each case required an average time of 4 days to converge.

5.6.1 Effect of Cavity Width at Constant Cavity Radius r_{c1}

Figure 5.19 shows how the increase in inter-cavity distance and decrease in cavity length stabilizes the heat transfer distribution along the wall-jet region of an impinging surface. A noteworthy fact is that the depth of cavity changes corresponding to parametric changes which plays an important role in stable wall-jet flow.

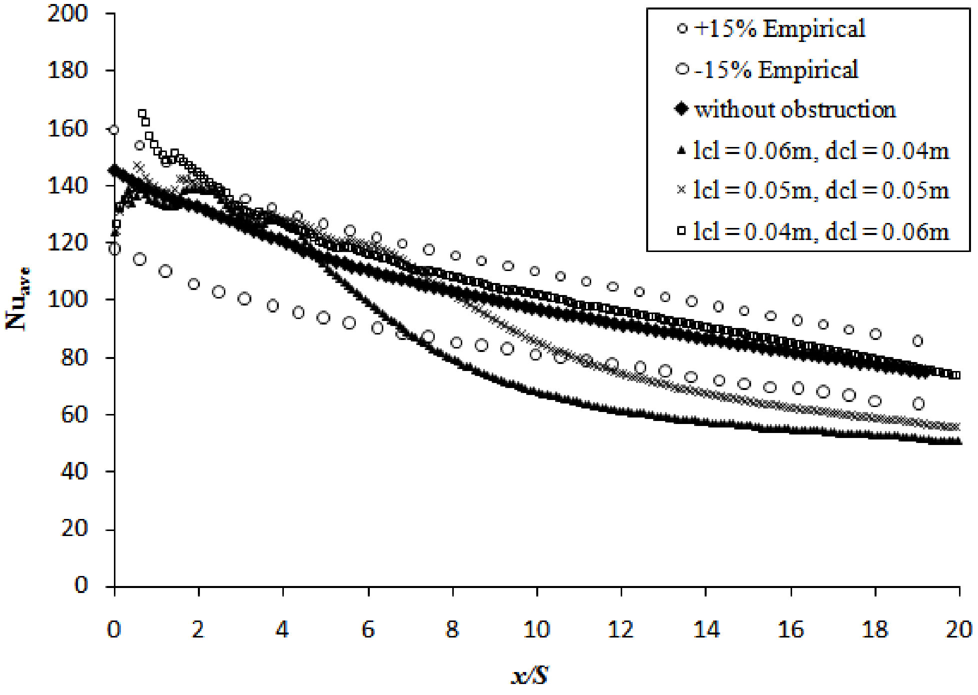

Figure 5.19 Comparison of Nusselt number distribution for various cavity widths and distance at constant cavity radius of 0.05 m

In Fig. 5.19, as the cavity depth decrease from 0.01 to 0.004 m, the width of each cavity l_c decreases from 0.06 m to 0.04m. It was observed that the flow is detached in the first two cases due to higher cavity depth, but this disappears at lower cavity depth.

In case with l_{c1} = 0.004, d_{c1} = 0.006, the distance between the cavities d_c is large and width of the cavity l_c is small stabilizing the flow along the wall-jet region.

In the same curve, the average Nu from $x/S = 0$ to 15 gives 2-15% heat transfer enhancement implying high wall pressure gradient.

5.6.2 Effect of cavity width on heat transfer at constant cavity radius r_{c2}

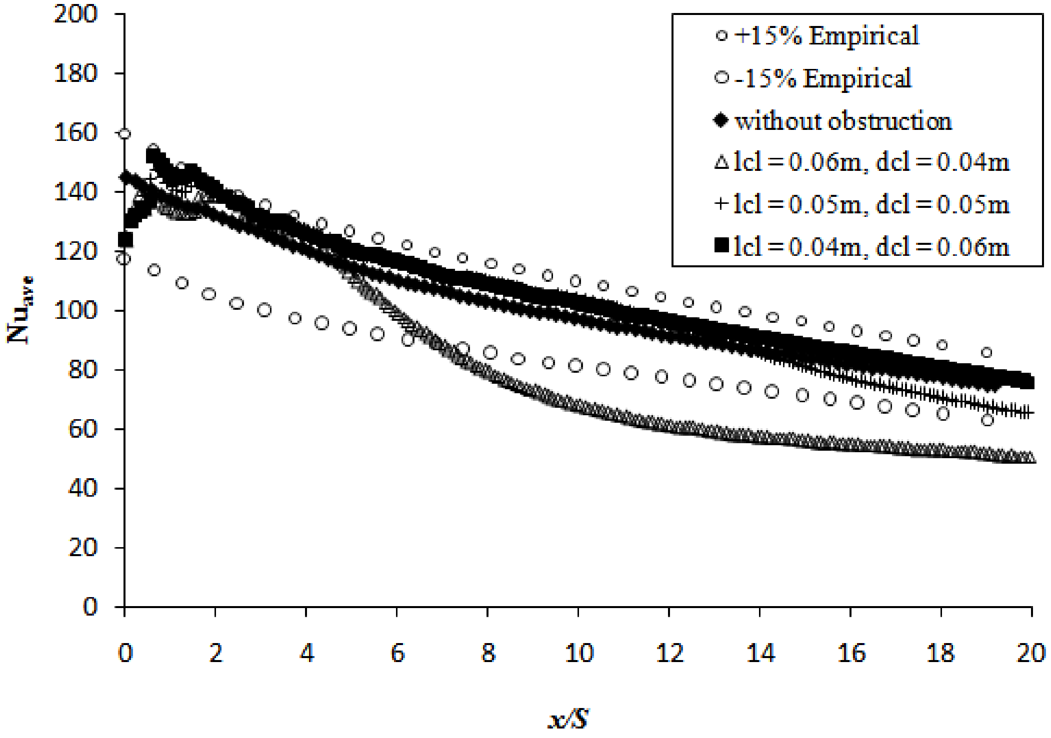

Figure 5.20 Comparison of Nusselt number distribution for various cavity width and distance at constant cavity radius of 0.06 m

In Fig. 5.20, a similar trend as found in Fig. 5.19 was observed but with a better stability. It should be noted that a higher cavity radius is used which gives a lower corresponding cavity depth.

As discussed earlier, higher cavity-to-cavity distance and lower cavity depth helps in stabilizing the flow and avoiding separation in the wall-jet region, as in case F5 (l_{c1} =

0.00, d_{c1} = 0.00) with cavity depth 0.005m which satisfies this phenomenon due to increase in r_c.

5.6.3 Effect of Cavity Width at Constant Cavity Radius r_{c3}

Figure 5.21 shows the effect of cavity width l_{c1}, l_{c2} and l_{c3} at cavity radius r_{c3}. A general observation from all the plots is that a combination of l_{c1} = 0.004, d_{c1} = 0.006, and r_{c1} = 0.005 (case F3) yielded better results than the other cases in Table 4.6.

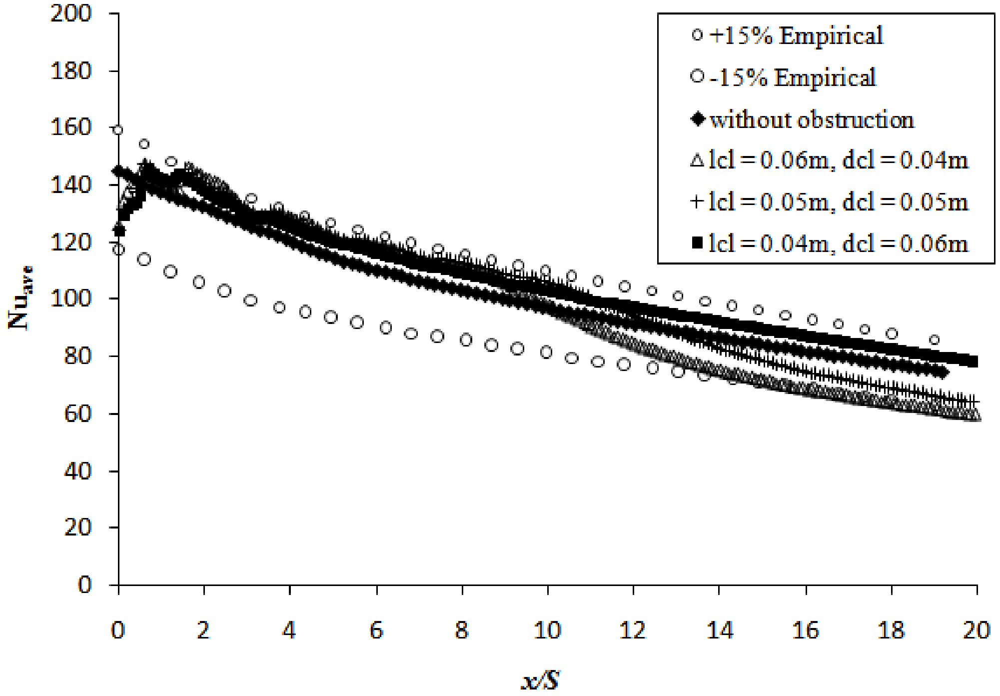

Figure 5.21 Comparison of Nusselt number distribution for various cavity width and distance at constant cavity radius of 0.07 m

All the curves take an anticipated profile at least till x/S = 10. The cavity radius is maximum and the cavity depth is minimum; hence the case with l_{c3} = 0.004, d_{c3} = 0.006, r_{c3} = 0.007, cavity depth = 0.003 satisfactorily heats the impinging wall. However, any further increase in the cavity depth (eg. case F8 with l_{c2} = 0.004, d_{c2} = 0.006, r_{c3} = 0.007, cavity depth = 0.0046) combination yields results but due to the effect of higher cavity width, they gradually looses stability.

7-8% heat transfer enhancement is observed in case with l_c = 0.04 m and d_c = 0.06 m at cavity depth 0.003m.

5.6.4 Comparison of Nusselt number Distribution With and Without Cavities

The best curve in the Fig. 5.20 was revealed as that of case with cavity length, l_{c3} = 0.004, inter-cavity distance, d_{c3} = 0.006, cavity radius, r_{c3} = 0.007 and cavity depth = 0.003 m. A comparison was made between the Nusselt number distributions of best parametric combination found for cavity surface and a plane impingement surface as shown in Fig. 5.21.

Further important findings from this investigation were found as

Inter-cavity distance on the impingement surface should not be less than 5 times the jet radius R for a stable wall-jet flow.

As the radius of the cavity increases with constant cavity width, the overall heat transfer distribution value also increases.

Larger cavity widths l_c and smaller inter-cavity distance d_c can be used for lower jet-to-jet spacing in the system. From Fig. 5.19 and Fig. 5.20 a jet-to-jet spacing of less than 0.4 m is suitable for cavity width greater than $4R$.

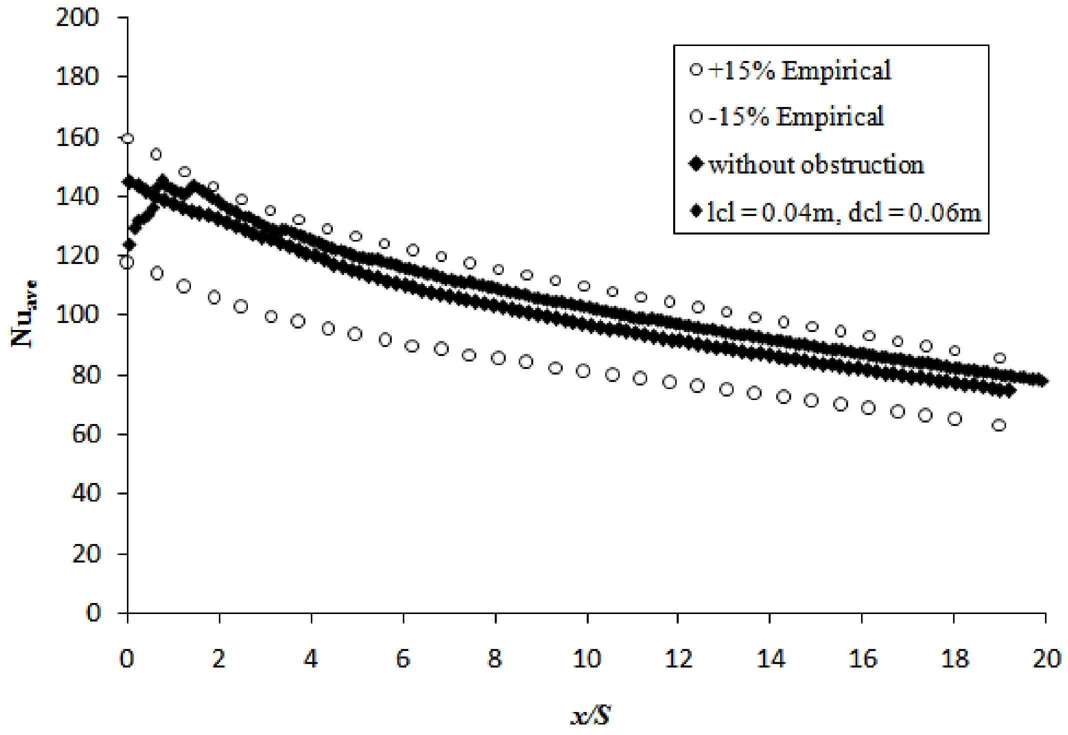

Figure 5.22 Comparison of Nusselt number distribution with and without cavity surface

Inter-cavity distances d_{c1} = 0.004 and d_{c2} = 0.005 yield higher values of heat transfer than d_{c3} = 0.006, but the flow with d_{c1} and d_{c2} soon decelerates and loses its energy giving a below normal heat distribution. However, as stated earlier they are suitable for small jet spacing to give higher heat transfers than the best one in the present study.

Vortices at the cavity boundary create turbulence insisting heat transfer enhancement. In the direction of the flow, vortices are formed on the curved surface when the flow enters the cavity and on the flat surface when the flow leaves the cavity. These are the boundaries where significantly high amount of heat transfer is observed (see Fig. 5.21). The base of the cavity remains cooler than the average heat transfer coefficient.

Half of each cavity facing the flow experiences a higher heat transfer than the other half as the flow entering the cavity falls over the opposite side of the cavity.

CHAPTER 6

CONCLUSIONS

A numerical investigation for various obstructions to enhance heat transfer on a surface using 2D hot-air jet was conducted. Six obstructions were modeled and simulated to study and compare the heat transfer distribution against the validated model. Significant observations were made for all the results obtained.

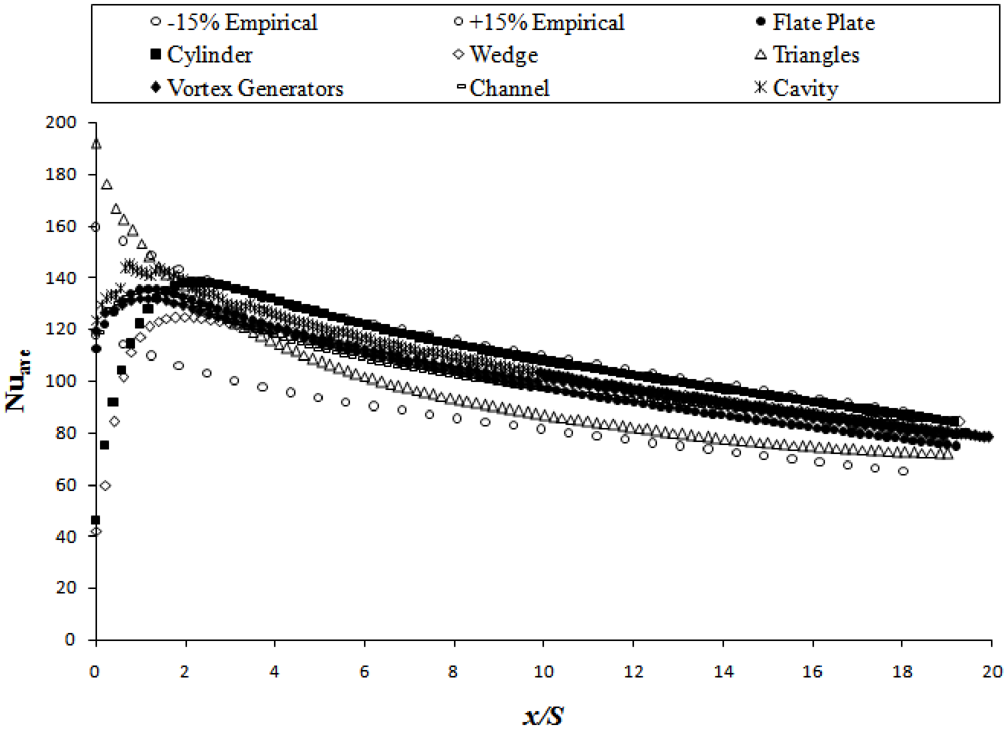

Figure 6.1 Best results obtained for each model

All the models investigated produced an increment in the heat transfer when compared to the result obtained from jet impingement without using any obstruction. Each obstruction has its own effect on Nusselt number distribution along the impinging wall. The best results obtained for each model is shown in Fig. 6.1.

6.1 Influence of Obstructions on Jet Impingement Heat Transfer

Jet obstructions are the easiest to model, investigate and manufacture. They follow an explicit trend in the parametric study. Conical wedge and cylinder were the most efficient obstructions enhancing the uniformity of heat transfer along the length of impinging wall. Unlike the triangles model, these models not only increased the heat transfer at stagnation region but also on the wall past the stagnation region. Except in the case of cylinder model, all other obstructions were giving almost the same values at the far wall-jet region.

Cylinder model resulted in better heat transfer distribution throughout the wall-jet region. Hence, the most suitable obstruction for heat transfer enhancement using jet impingement is cylinder.

6.2 Influence of Surface Liner on Jet Impingement Heat Transfer

A free ended channel was numerically investigated as surface liner to enhance the heat transfer caused by jet impingement. A strategic approach to decide the location and length of the channel was made. A trend followed by all the channels is a low heat transfer within the channel and a gradual increase in heat transfer distribution at the exit of the channel. This phenomenon compensated overall heat transfer to a satisfactory level suggesting further modifications in using a channel to enhance jet impingement heat transfer.

6.3 Influence of Surface Obstructions on Jet Impingement Heat Transfer

Two models were numerically investigated under surface obstruction technique. Vortex generators attached to wall surface and cavity surface as cavity were modeled to enhance the heat transfer distribution. The significant effect of vortex generators was observed on heat transfer in its proximity; whereas cavity surface produced much better results encouraging future work.

6.4 Recommendations

The present investigation was limited to fewer parameters and parametric changes. Although significant findings were made, a large part of undiscovered phenomena exists. Few recommendations for future work are as follows:

- Unsteady transient cases can be modeled elevating the limit of low turbulent and simple designs.
- A combination of surface liner and surface obstructions need to be investigated.
- A 3D modeling in which vortex generators are appropriately placed to form a flow pattern in heat transfer is encouraged.

References

[1] Federal Aviation Administration, *Proceeding of the FAA International Conference on Aircraft In-Flight Icing*, Vol. I and II, Springfield, Virginia, May 6—8, 1996. Final Report.

[2] United States Department of Transportation, Federal Aviation Administration. FAA In-Flight Icing Plan, Apr. 1997.

[3] Thomas, S. K., Cassoni, R. P., and MacArthur, C. D., "Aircraft Anti-Icing and Deicing Techniques and Modeling," *AIAA Journal of Aircraft*, Vol. 33, No. 5, Sept.-Oct. 1996, pp. 841—854.

[4] Cornaro, C., Fleischer, A. S., and Goldstein, R. J., "Flow Visualization of a Round Jet Impinging on Cylindrical Surfaces," *Experimental Thermal and Fluid Science*, Vol. 20, 1999, pp. 66—78.

[5] Metzger, D. E., Yamashita, T., and Jenkins, C. W., "Impingement Cooling of Concave Surfaces with High Velocity Impinging Air Jets," *Journal of Engineering for Power-Transactions of the ASME*, Vol. 91, 1969, pp. 149—158.

[6] Dyban, E. P., and Mazur, A. I., "Heat Transfer for a Planar Jet Striking a Concave Surface," translated from *Inzhenerno-Fizicheskii Zhurnal*, Vol. 17, No. 5, Nov. 1969, pp. 785—790.

[7] Al-Khalil, K. M., *Numerical Simulation of an Aircraft Anti-Icing System Incorporating a Rivulet Model for the Runback Water*, Ph.D. thesis, University of Toledo, Ohio, USA, June1991.

[8] Al-Khalil, K. M., and Potapczuk, M. G., "Numerical Modeling of Anti-Icing Systems and Numerical Comparison to Test Results on a NACA 0012 Airfoil," 31st Aerospace Sciences Meeting & Exhibit, AIAA Paper 93-0170, Reno, NV, Jan.1993.

[9] Martin, H., "Heat and Mass Transfer between Impinging Gas Jets and Solid Surfaces," *Advances in Heat Transfer*, Vol. 13, Academic Press, 1977, pp. 1—60.

[10] Jambunathan, K., Lai, E., Moss, M. A., and Button, B. L., “A Review of Heat Transfer Data for Singular Jet Impingement,” *International Journal of Heat and Fluid Flow*, Vol. 13, 1992, pp. 106—115.

[11] Zhou, D., Lee, S. J., Ma, C. F. & Bergles, A. E., “Optimization of Mesh Screen for Enhancing Jet Impingement Heat Transfer,” *Heat Mass Transfer*, Vol. 42, 2006, pp. 501—510.

[12] Michael Papadakis, “Parametric Investigation of Bleed Air Protection System,” *44th AIAA Aerospace Sciences Meetings and Exhibit*, 2006, pp. 9 – 12.

[13] Farooq Saeed and Ahmad Z. Al-Garni, “Numerical Simulation of Surface Heat Transfer from an Array of Hot-air Jets,” *25th AIAA Applied Aerodynamic Conference*, 2007, pp. 25—28.

[14] D.W. Zhou and Sang-Joon Lee, “Forced Convective Heat Transfer with Impinging Rectangular Jets” *International Journal of Heat and Mass Transfer*, 2007, pp. 1917—1926.

[15] Lee, D.H., Lee, Y.M., Kim, Y.T., Won, S.Y. and Chung, Y.S., “Heat Transfer Enhancement by the Perforated Plate Installed between an Impinging Jet and the Target Plate,” *International Journal of Heat and Mass Transfer*, Vol. 45, 2002, pp. 213—217.

[16] Haneda, Y., Tsuchiya, Y., Nakabe, K. and Suzuki, K., “Enhancement of Impinging Jet Heat Transfer by making use of Mechano-Fluid Interactive Flow Oscillation,” *International Journal of Heat and Fluid Flow*, Vol. 19, 1998, pp. 115—124.

[17] Bergles. E, “ Heat Transfer Enhancement - The Maturing of Second-Generation Heat Transfer Technology,” *Heat Transfer Engineering*, Vol 1, Issue 1, 1997, pp. 47—55.

[18] Gardon, R., Akfirat, J. C., “The Role of Turbulence in Determining the Heat Transfer Characteristics of Impinging Jets,” *International Journal of Heat Mass Transfer*, Vol. 8, 1965, pp. 1261—1272.

[19] Obot, N. T., Majumdar, A. S., Douglas, W. J. M., “The Effect of Nozzle Geometry on Impingement Heat Transfer under a Round Turbulent jet,” *ASME Paper No.79-WA/HT-53*, 1979.

[20] Popiel, C. O., Boguslawski, L., “Effect of Flow Structure on the Heat or Mass Transfer on a Flat Plate in Impinging Round Jet”, in: Proc. *2nd UK National Conference on Heat Transfer*, University of Strathclyde, Vol. 1, 1988, pp. 663—685.

[21] Oyakawa, K., Azama, T., Senaha, I., Hiwada, M., “Effects of Nozzle Configuration on Impingement Heat Transfer”, in: Proc. *ASME/JSME Thermal Engineering Conference*, Maui, USA, Vol. 1, 1995, pp. 377—384.

[22] Kurima, J., Miyamoto, M., Harada, T., “Heat Transfer Augmentation of an Axisymmetric Impingement Jet using a Perforated plate set in Front of Target Plate,” *Heat Transfer- Jpn.*, 1989, pp. 1—20.

[23] Zumbrunnen, D. A., Aziz, M., “Convective Heat Transfer Enhancement Due to Intermittency in an Impinging Jet,” *Journal of Heat Transfer*, Vol. 115, Feb. 1993, pp. 91—98.

[24] Huber, A. M., Viskanta, R., “Convective Heat Transfer to a Confined Impinging Array of air Jets wit Spent air Exits,” *Journal of Heat Transfer*, Vol. 16, 1994, pp. 570—576.

[25] Morency, F., Tezok, F., and Paraschivoiu, I., “Anti-Icing System Simulation Using CANICE,” *AIAA Journal of Aircraft*, Vol. 36, No. 6, Nov.-Dec. 1999, pp. 999—1006.

[26] Behnia, M., Parneix, S., Shabany, Y. and Durbin, P. A., “Numerical Study of Turbulent Heat Transfer in Confined and Unconfined Impinging Jets,” *International Journal of Heat and Fluid Flow*, Vol. 20, 1999, pp.1—9.

[27] Saeed, F., Morency, F., and Paraschivoiu, I., “Numerical Simulation of a Hot-Air Anti-Icing Simulation,” 38th Aerospace Sciences Meeting & Exhibit, AIAA Paper 2000-0630, Reno, NV, Jan. 2000.

[28] Saeed, F., and Paraschivoiu, I., “Numerical Correlation for Local Nusselt Number Distribution for Hot-Air Jet Impingement on Concave Surfaces,” Proceedings of the 8th Annual Conference of the CFD Society of Canada, CFD2K, Montréal, Québec, Canada, June 11—13, 2000, Vol. 2, pp. 897—904.

[29] Fregeau, M., Saeed, F., and Paraschivoiu, I., "Numerical Heat Transfer Correlation for Array of Hot-Air Jets Impinging on 3-Dimensional Concave Surface," AIAA *Journal of Aircraft*, Vol. 42, No. 3, 2005, pp. 665—670.

[30] Brown, J. M., Raghunathan, S., Watterson, J. K., Linton, A. J., and Riordon, D., "Heat Transfer Correlation for Anti-Icing Systems," *AIAA Journal of Aircraft*, Vol. 39, No. 1, Jan.—Feb. 2002, pp. 65—70.

[31] Lee, J., and Lee, S., "The Effect of Nozzle Configuration on Stagnation Region Heat Transfer Enhancement of Axisymmetric Jet Impingement," *International Journal of Heat and Mass Transfer*, Vol. 43, 2000, pp. 3497—3509.

[32] El-Sheikh, H.A. and Garimella, S.V., "Enhancement of Air Jet Impingent Heat Transfer Using Pin-Fin Heat Sinks," *IEEE Transactions on Components and Packaging Technology*, Vol. 23, No. 2, June 2000, pp. 300—308.

[33] Camci, C., "Forced Convection Heat Transfer Enhancement Using a Self-Oscillating Impinging Planar Jet," *Transactions of the ASME*, Vol. 124, 2002, pp. 770—782.

[34] Srinath V. Ekkad and David Kontrovitz, "Jet Impingement Heat Transfer on Dimpled Target Surface", *International Journal of Heat and Fluid Flow*, Vol 23, 2002, pp. 22—28.

[35] Herbert Hofmann, Holger Martin and Matthias Kind, "Numerical Simulation of Heat Transfer from an Impinging Jet to a Flat Plate," *Chemic Ingenieur Technik*, Vol 27, No. 1, 2004, pp. 27—30.

[36] Schlunder E. U and Gnielinski V., *Chem. Ing. Tech.*, Vol 39, No. 9-10, 1967, pp. 578.

[37] Sarghini, F., Ruocco, G., "Enhancement and Reversal Heat Transfer by Competing Modes in Jet Impingement," *International Journal of Heat and Mass Transfer*, Vol. 47, 2004, pp. 1711—1718.

[38] P. S. Shadlesky, "Stagnation Point Heat Transfer for Jet Impingement to a Plane Surface," *AIAA*, Vol. 21, No. 8, 1982, pp. 1214—1215.

[39] K Kanokjaruvijit and R F Martinez-Botas, "An Experimental investigation of the Heat Transfer due to Multiple Jets Impinging normally on a Dimpled Surface"

Proceedings of the Institution of Mechanical Engineers, Vol 218, No 11, 2004, pp. 1337—1347.

[40] M. Fregeau, F. Saeed and I. Paraschivoiu, "Numerical Heat Transfer Correlation for Array of Hot-Air Jets Impinging on 3-Dimensional Concave Surface," *AIAA Journal of Aircraft*, Vol. 42, No. 3, 2005, pp. 665—670.

[41] Shyy Woei Chang, Shyr Fuu Chiou and Chuen Fei Chang, "Heat Transfer of Impinging Jet Array over Concave-Dimpled Surface with Application to Cooling of Electronic Chipsets", *Experimental Thermal and Fluid Science,* Vol 31, 2007, pp. 625—640.

[42] Doseo Park, Carlos Silva, Egidio Marotta and Leroy Fletcher, "Study of Laminar Forced Convection Heat Transfer for Dimpled Heat Sinks" *Journal of Thermophysics and Heat Transfer,* Vol 22, No. 2, 2008, pp. 262—270.

[43] P. M. Nakod, S. V. Prabhu and R. P. Vedula, "Heat Transfer Augmentation between Impinging Circular Jet and Flat Plate using Finned Surfaces and Vortex Generators, *Experimental Thermal and Fluid Science*, Vol 32, 2008, pp. 1168—1187.

[44] Abdelkader Korichi, Lounes Oufer and Guillaume Polidori, "Heat Transfer Enhancement in Self-Sustained Oscillatory Flow in a Grooved Channel with Oblique Plates", *International Journal of Heat and Mass Transfer*, Vol 52, 2009, pp. 1138—1148.

[45] A. Mokrani, C. Castelain and H. Peerhossaini, " Experimental Study of the Influence of the Rows of Vortex Generators on Turbulence Structure in a Tube", *Chemical Engineering and Processing: Process Intensification"* Vol 48, 2009, pp. 659—671.

[46] Li-Min Chang, Liang-Bi Wang, Ke-Wei Song, Dong-Liang Sun and Ju-Fang Fan, "Numerical Study of the relationship between Heat Transfer Enhancement and Absolute Vorticity flux along Main Flow Direction in a Channel formed by a Flat Tube Bank Fin with Vortex Generators", *International Journal of Heat and Mass Transfer,* Vol52, 2009, pp. 1794—1801.

[47] Spalart P. and Allmaras S., "A one-equation turbulence model for aerodynamic flows," Technical Report AIAA-92-0439, *American Institute of Aeronautics and Astronautics*, 1992.

[48] Lauder B. E., and Spadling D. B., *Lectures in Mathematical Models of Turbulence*, Academic Press, London, England, 1972.

[49] Yakhot V. and Orszag. S. A., "Renormalization Group Analysis of Turbulence: I. Basic Theory," *Journal of Scientific Computing*, Vol 1, No. 1, 1986, pp. 1—51.

[50] Shih T. H, Liou W. W., Shabbir A., Yang Z., and Zhu J., "A New *k*- ε Eddy-Viscosity Model for High Reynolds Number Turbulent Flows - Model Development and Validation," *Computers Fluids*, Vol 24, No. 3, 1995, pp. 227—238.

[51] Wilcox D. C., Turbulence Modeling for CFD, DCW Industries, Inc., La Canada, California, 1998.

[52] Farooq Saeed, Ahmed Z. Al-garni and Mohammed M. A. Khan, "Numerical Investigations of Mechanisms to aid in Enhancing Surface Heat Transfer from an Impinging 2D Hot-air Jet," *Canadian Aeronautical and Space Institute (CASI) Conference*, Aerodynamic Symposium, 2009.

[53] Meola, C., Carlomagno, G.M., Riegel, E.and Salvato, F., "An Experimental Study of an Anti-Icing Hot-air Spray-Tube System," 19th Congress ICAS, Anaheim, CA, Sept.1994.

[54] Rahman, M. M, Silikonen, T, " A Simplified v2-f Model for Near-Wall Turbulence," *International Journal for Numerical Methods in Fluids*, Vol. 12, Issue 54, 2007, pp. 1387—1406.

Vita

- Mohammed Mumtaz Ahmed Khan
- Contact Address: House # 2-5-591, Subedari, Hanamkonda, Warangal, India
- Contact # 91-870-2571724
- Email Address: mumtaz_be@yahoo.co.in
- Born on 7th November, 1982 in Warangal, India.
- Received Bachelor of Technology (B. Tech) degree in Mechanical Engineering from Kakatiya Universtiy, Warangal, India in August 2004.
- Graduated from Department of Aerospace Engineering at King Fahd University of Petroleum and Minerals (KFUPM), Dhahran, Saudi Arabia in January 2010.